A Toolbox for Observing and Modulating the Gut-Brain Axis

by

Aliesha Danielle Garrett

Department of Biomedical Engineering
Duke University

Date:_____
Approved:

_____
Mike Tadross, Supervisor

_____
Charlie Gersbach

_____
Diego Bohórquez

_____
G. Allan Johnson

_____
David Hsu

Dissertation submitted in partial fulfillment of
the requirements for the degree of Doctor
of Philosophy in the Department of
Biomedical Engineering in the Graduate School
of Duke University

2022

ABSTRACT

A Toolbox for Observing and Modulating the Gut-Brain Axis

by

Aliesha Danielle Garrett

Department of Biomedical Engineering
Duke University

Date:_____
Approved:

_____
Mike Tadross, Supervisor

_____
Charlie Gersbach

_____
Diego Bohórquez

_____
G. Allan Johnson

_____
David Hsu

An abstract of a dissertation submitted in partial
fulfillment of the requirements for the degree
of Doctor of Philosophy in the Department of
Biomedical Engineering in the Graduate School of
Duke University

2022

Abstract

An estimated 10% of people worldwide have an enteric nervous system (ENS) related illness including irritable bowel syndrome (IBS), diabetes, colorectal cancer, fecal incontinence, and chronic constipation or diarrhea. Current drug treatments have severe side effects and often do not adequately address symptoms; a new approach is needed. ENS stimulation is a promising therapy for these patients, but a major limitation to this approach is our lack of knowledge. The human ENS is comprised of 5 million neurons and drives the digestive system, but its normal function and connections to the central nervous system (CNS) remain poorly understood. One of the major canonical signaling pathways between the ENS and the CNS is the vagus nerve, but the neural circuits involved are still under investigation. Better understanding of these circuits would provide a potential method of treatment for ENS related illness, with neurostimulation serving as an alternative to pharmaceutical treatments. Herein I describe a project which addresses these needs via development of new imaging tools to better understand the gut-brain axis, as well as demonstrating its utility as a target for treatment of gastrointestinal (GI) illness, specifically cancer-associated cachexia.

Leaders in enteric neuroscience note that the continued inconsistencies in GI electrotherapies are driven by a fundamental lack of understanding of gut innervation and circuitry. New tools to directly observe colonic innervation and neuronal response, as well as a map of the whole peripheral nervous system, will reveal crucial targets for stimulation and enable more efficient targeting selection for neurostimulation or other local interventions, which will reduce off target effects and improve efficacy. To address these issues, I have developed an intravital window for direct imaging of the colon,

enabling observation of colonic ENS response to stimulation in vivo for the first time. Additionally, I have developed an embryonic window, allowing visualization of embryonic GI development from E9.5 through birth. Finally, I have generated a mouse peripheral nerve map based on Diffusion Tensor Magnetic Resonance Imaging (DT MRI). Using novel scan parameters and post-processing algorithms, I identified nerve fibers throughout the body and generated quantitative tractography which specifically highlights GI innervation via the vagus nerve.

Cachexia is a multi-systemic syndrome which produces weight loss, muscle atrophy, adipose wasting, fatigue, and anorexia. Affecting an estimated 1% of the global population and up to 80% of all cancer patients, cachexia is fatal in roughly 30% of cases and is incurable. Cancer-associated cachexia (CAC) is particularly devastating as in addition to resulting in decreased quality of life, CAC reduces tolerance and efficacy of cancer treatments and higher overall mortality. As many as half of all cancer deaths are attributed to CAC. There are currently no clinically meaningful treatments for CAC, despite attempts to employ dietary support, physical therapy, anti-inflammatory medication, appetite stimulants, and other supportive therapies. Herein I describe potential therapeutic approach for treatment of CAC via vagal perturbation – either by vagotomy or ultra-low frequency vagal block with an implanted stimulator. This intervention significantly attenuates weight loss, skeletal muscle atrophy, anorexia, urea cycle dysregulation, and circulating inflammatory cytokine elevation. Most importantly, it increases survival time in mice injected with tumor cells, suggesting this could be a clinically meaningful approach for treatment of CAC.

Dedication

For Ian Johnson; curiosity is what it looks like when you’re in love with the world. Thank you for reminding me this is a world worth being curious about.

Contents

List of Tables

List of Figures

Acknowledgements

A tremendous amount of support for this dissertation was provided by Xiling Shen, PhD, who served as my PhD advisor for all but the final six months of my degree. I also owe a great deal of thanks to all the collaborators and lab colleagues who contributed to the inspiration, feedback, and technical assistance provided, particularly current and past members of the Center for In Vivo Microscopy (CIVM), the Shen Lab, the Bohórquez lab, the Grill lab, and the Morizio lab at Duke. In these groups I especially thank Nikolai Rakhilin, Brad Barth, Nikki Pelot, Maya Kaelberer, Ashlesha Deshmukh, Shree Bose, and William Wong, without whom this dissertation would surely be a very different document. I also sincerely thank my dissertation committee, whose critiques have resulted in a more meaningful and vigorous body of research.

I also wish to thank my family for their support and inspiration. Mom, I wouldn't be here if you hadn't made sure I could always put my education first. Eric, I miss you every day; your love and humor changed our lives. Alex, thank you for your humor and the reminder that sometimes you have to leave the lab. Pat, your growing family reminds me why we keep trying to make progress. Dad, thanks for the practice communicating my work to a lay audience – it's an essential skill! Ian, you make every day possible, and you continuously inspire me to do my best work. Rob, thank you for making me laugh hysterically while writing this dissertation.

1. Introduction

1.1 Role of the Gut-Brain Axis

The gut-brain axis is a bidirectional electrical and chemical signaling pathway which drives appetite, hunger, digestion, metabolism, immune activation, and other essential functions of the gastrointestinal system (Carabotti et al., 2015, Foster et al., 2017, Han et al., 2018, Kaelberer et al., 2018, Mayer, 2011). The sacral and vagus nerves are the key electrical elements connecting the enteric nervous system (ENS) and central nervous system (CNS). However, the gut-brain axis also involves systemic chemical signaling via the endocrine system as well as immune cells and the gut microbiome (Bercik et al., 2011, Carabotti et al., 2015, Foster et al., 2017, Han et al., 2018, Kaelberer et al., 2018, Lyte, 2014, Mayer, 2011).

Collectively, the gut-brain axis is responsible for maintenance of homeostasis and essential metabolic and digestive functions. Increasingly, however, researchers and clinicians are aware that in addition to metabolic and digestive health, the gut-brain axis contributes heavily to the body's ability to muster robust immune responses against pathogens, the ambient inflammatory state of the body and autoimmune activity, as well as emotional wellbeing and neurological health (Bercik et al., 2011, Carabotti et al., 2015, Foster et al., 2017, Kaelberer et al., 2018, Lyte, 2014, Mayer, 2011, Rao and Gershon, 2016, Sampson et al., 2016).

1.1.1 The Enteric Nervous System

The ENS is an independent nervous system embedded in the walls of the gastrointestinal system from the esophagus to the rectum. Comprised of 5 million neurons, this autonomous "gut brain" drives the digestive system (Furness, 2012,

Furness, 2008). Even when the gastrointestinal tract is removed from an organism, the organs will continue to function for some time; peristalsis and passage of waste distally through the system will continue as long as the tissue is kept warm, wet, and fed (Rao and Gershon, 2016). This is not the typical operation, however, and communication between the ENS and CNS allows for modulation of enteric activity in response to organismal status and adjustments to behaviors or biological processes in other systems in response to the condition of the gut. This feedback circuit also provides redundant controls for GI function and reduces the likelihood pathology will develop as a result of ENS dysfunction or environmental stresses and disruptions (Rao and Gershon, 2016, Brierley et al., 2018, Carabotti et al., 2015, Han et al., 2018).

The ENS has two major anatomical components, the submucosal plexus and the myenteric plexus; these ganglionated plexuses contain the enteric neurons and their supporting glia and coordinate sensation and motor function within the gut. The submucosal plexus is located below the endothelial layer and the circular muscle, while the myenteric plexus is located between the circular muscle and the longitudinal muscle. Synapsing occurs between the plexuses as well as with external neural pathways, providing a sophisticated neural network to collect and interpret sensory information and transmit motor response, endocrine activity, immune activation, or other autonomic responses (Furness, 2012, Furness, 2008).

Despite its size and importance, there are significant unknowns pertaining to the development and function of the ENS as well as pathogenesis; significant aspects of ENS function such as signaling molecules, functional circuits, neuronal subpopulation identities, external innervation sources, and more are yet to be fully elucidated (Barth et al., 2017, Furness, 2012, Furness, 2008, Jakob et al., 2020, Kulkarni et al., 2017, Mayer,

2011, Morarach et al., 2021, Rakhilin et al., 2016, Rakhilin et al., 2019, Schneider et al., 2019). With GI disorders impacting a significant and growing portion of the human population, better understanding the requirements for normal gut function, mechanisms of disease, and therapeutic response in the ENS will be critical in clinical settings.

1.1.2 The Sacral Nerve

The sacral nerve provides innervation to the lower limbs and pelvic region. Emerging from the lower lumbar vertebrae and sacral vertebrae, the sacral nerve is part of the lumbosacral plexus and provides important motor and sensory functions for the lower GI tissues (Garrett et al., 2021, Rakhilin et al., 2019, Spencer et al., 2016b, Furness, 2012). The sacral nerve is clinically acknowledged to be of particular importance to colonic motility and fecal continence; activation of the sacral nerve can improve outcomes for patients struggling with chronic constipation, chronic diarrhea, and fecal incontinence (Carrington et al., 2014, Dudding et al., 2009, Iachetta et al., 2012, Kenefick et al., 2002, Sharma et al., 2013, Wexner et al., 2010). In addition to the colon and rectum, the sacral nerve innervates the bladder and integrity is also crucial for both continence and voiding (Furness, 2012, Spencer et al., 2016b, Wexner et al., 2010). The sacral nerve contains both motor afferents and sensory efferents, carrying motor signals from the CNS to the gut and sensory signals from the gut to the brain (Furness, 2012, Furness, 2008).

1.1.3 The Vagus Nerve

The vagus nerve, also called cranial nerve X, is one of the key electrical mediators of the gut-brain axis, with direct vagal innervation documented to the heart, lungs, digestive tract, brown adipose tissue, kidneys, liver, and pancreas (Garrett et al.,

2021, Altschuler et al., 1993, Bercik et al., 2011, Browning et al., 2017, Chakravarthy et al., 2015, Chang et al., 2015, Herrity et al., 2014, Kupari et al., 2019, Matsuhisa et al., 2000, Pavlov and Tracey, 2012, Williams et al., 2016). The vagus is known to have key regulatory roles in appetite, hunger, digestion, metabolism, immune activation, and other essential functions of the gastrointestinal system (Carabotti et al., 2015, Foster et al., 2017, Han et al., 2018, Kaelberer et al., 2018, Mayer, 2011). In the upper gastrointestinal tract, vagal efferent activity regulates bowel motility via close interaction with the enteric nervous system (ENS), a complex network of neurons and glia in the bowel wall that controls most aspects of bowel function (Lyte, 2014, Schneider et al., 2019). Vagal sensory (afferent) fibers also provide rich information to the brain, where vagal signaling is influenced by intestinal microbiota, intraluminal nutrients, and the immune system (Carabotti et al., 2015, Kaelberer et al., 2018). Additionally, gut-innervating vagal neurons have been shown to sense distension and induce reward in the brain via dopamine release (Han et al., 2018, Williams et al., 2016). Emerging evidence suggests that nutrients, microbiota, and inflammation in the gut trigger varied sensory neurons in the vagal nodose ganglion, which process the signals and relay them to the brain stem inducing reactions ranging from satiety to anxiety.

The nodose ganglion, the anatomical location of all cell bodies for vagal neurons, contains neurons that innervate not only the gut, but also other visceral organs such as the heart, lung, liver, and spleen, and modulate functions including breathing, inflammation, and energy metabolism (Pavlov and Tracey, 2012, Chang et al., 2015, Yahagi, 2017, Matsuhisa et al., 2000). Furthermore, the right vagus nerve is solely responsible for gut-induced reward (Han et al., 2018), suggesting asymmetry between the left and right nodose ganglion. The vagus nerve is a promising target for many

diseases, but its role in colonic innervation as well as innervation of other organs remains debated, and a lack of understanding of vagal neural circuits and their spatial organization results in inadequate targeting.

Still, the vagus nerve may play important roles in the pathophysiology and treatment of a wide range of human disorders including irritable bowel syndrome, gastroparesis, chronic intestinal pseudo-obstruction, inflammatory bowel disease (IBD), Parkinson's disease, anxiety, chronic inflammation, and metabolic syndromes such as diabetes and obesity (Sung et al., 2014, Liu et al., 2017, Sampson et al., 2016, Foster et al., 2017, Bercik et al., 2011, de Lartigue, 2016, Guo et al., 1987, Pavlov and Tracey, 2012, Malbert et al., 2017).

1.2 Burden of Gut-Brain Disease

Diseases of the gut are among the most prevalent in the human population and are on the rise (Bonaz et al., 2017, de Lartigue, 2016, Baracos et al., 2018, Chey et al., 2015, Elmentaite et al., 2020, Foster et al., 2017, Furness, 2012, Jandhyala et al., 2015, Kulkarni et al., 2017, Mayer, 2011, Opazo et al., 2018, Rao and Gershon, 2016, Sampson et al., 2016, Talley et al., 2015, Vermeulen et al., 2014). Disorders of the gut range from inconvenient or embarrassing to deadly. Functional gastrointestinal disorders (FGID) impact 1 in 10 individuals worldwide (Schneider et al., 2019). Global costs for treatment of irritable bowel disorder (IBD) alone exceed 15 billion USD annually, and some studies estimate the indirect costs exceed that (Kaplan, 2015). 42% of Americans are obese, and 10.5% are diabetic (WHO, 2018, Payne et al., 2019, Morsi et al., 2018, Göbel et al., 2017, de Lartigue, 2016). Colorectal cancer has a lifetime incidence of about 4%, and a 5-year survival rate of 64%, making it the fourth deadliest cancer (Dekker et al., 2019, Bray et al., 2018).

In addition to disorders in gut function, it is increasingly acknowledged that gut health has profound impacts on neurological health, mental health, and immune health. Depression, anxiety, Alzheimer's disease, Parkinson's disease, rheumatoid arthritis, autoimmune disorders, and more have now been linked to gut-brain dysfunction, and the gut-brain axis is an appealing therapeutic target, particularly where current treatments are ineffective (Rao and Gershon, 2016, Campos et al., 2017, Foster et al., 2017, Carabotti et al., 2015, Groves and Brown, 2005, Jakob et al., 2020, Opazo et al., 2018, Morsi et al., 2018, Koopman et al., 2016, Rani et al., 2016). Between these conditions and traditional gut disease, the burden of gut-brain disease is high, affecting a significant portion of the global population at some point over their lifetime.

1.2.1 Cancer Associated Cachexia

Cancer associated cachexia (CAC) is a multifactorial syndrome clinically defined by weight loss greater than 5%, weight loss greater than 2% in those with a body mass index (BMI) < 20 kg/m2, or depletion of skeletal muscle mass (Fearon et al., 2011, Kalantar-Zadeh et al., 2013). While cachexia is especially notable as a cancer-related condition, cachexia also has a noted incidence in patients with chronic heart failure, chronic obstructive pulmonary disease, chronic kidney disease, neurological diseases, rheumatoid arthritis, AIDS, eating disorders, and the elderly (von Haehling et al., 2016, Arthur et al., 2014, Kalantar-Zadeh et al., 2013). It is estimated that 0.5 - 1 % of the global population suffers from CAC, with 1.3 million patients in the US alone (Arthur et al., 2014, von Haehling et al., 2016).

CAC has profound impacts on outcomes for cancer patients. The onset of CAC increases chemotherapy toxicity and complications from surgeries, decreases quality of life in patients, and leads to higher mortality rates (da Rocha et al., 2019, Kalantar-

Zadeh et al., 2013). Additionally, cachectic patients are less responsive to therapies which they do tolerate, further reducing the likelihood they will recover (Vaughan et al., 2013). While CAC is most prominent in end-stage cancers, for some tumor types CAC is present even before the tumor is clinically detectable and in fact plays a key role in cancer survival and progression (Porporato, 2016). This suggests that CAC-related metabolic changes are not just an unfortunate symptom of terminal cancer, but may play a significant role in tumor survival and growth even early in disease progression. Prevalence of CAC is as high as 80% in some cancers, and an estimated 30% of cachectic patients will ultimately die from the syndrome; ultimately, half of all cancer deaths are attributed to cancers with the highest incidence of CAC (Dhanapal et al., 2011, von Haehling et al., 2016, Baracos et al., 2018).

Unfortunately, there are no meaningful clinical treatments for CAC. CAC cannot be reversed by standard nutritional intervention, and no correlation has been demonstrated between dietary intake and body composition parameters (Dodson et al., 2011, Gullett et al., 2011, Mohan et al., 2017). Even aggressive treatment, such as tube feeding, is rarely successful. Furthermore, pharmacologic interventions, including corticosteroids, anabolic steroids, and anti-inflammatory drugs, have all failed to produce meaningful improvements in clinical settings (Ohnuma, 2003, Marceca et al., 2020, Prado and Qian, 2018). Current evidence suggests that the individual pharmacologic treatments for CAC have no more than marginal benefit, although synergistic approaches might improve outcomes. Fundamentally, existing treatment paradigms fail to reverse the underlying metabolic pathology which drives CAC and produces downstream wasting, perhaps due to a focus by nutritionists and myologists on the end symptoms rather than the underlying mechanisms of disease.

CAC is a complex multi-systemic syndrome; tumor-derived catabolic factors and pro-inflammatory factors derived from tumor-immune crosstalk drive changes in appetite, glycolysis, proteolysis, lipolysis, and the urea cycle. While there are likely pathways in CAC which have yet to be identified, studies increasingly highlight the role of aberrant systemic signaling and metabolic disruptions. Key factors including TNFα, IL-1, IL-6, IFN-γ, TGFβ, and myostatin are thought to produce anorexic eating behaviors, decreasing appetite and reducing caloric availability (Porporato, 2016, Aoyagi et al., 2015, Baracos et al., 2018, Petruzzelli and Wagner, 2016, Campos et al., 2017). However, anorexia alone does not account for CAC, as increased feeding does not overcome cachectic weight loss; significant alterations in carbohydrate, lipid, and amino acid metabolism also contribute to the excess energy consumption beyond that attributable to the tumor (Durham et al., 2009, Petruzzelli and Wagner, 2016, Fearon et al., 2012, Porporato, 2016, Gullett et al., 2011). Cachectic individuals develop insulin resistance and decreased carbohydrate tolerance; in combination secreted tumor factors and reduced food intake, this induces browning of adipose tissue, futile cycling, and excess lipolysis (Petruzzelli and Wagner, 2016, Porporato, 2016, Baracos et al., 2018). Many of the same catabolic and inflammatory factors which drive anorexic eating also drive proteolysis of skeletal and cardiac muscle and reduce muscle synthesis (Baracos et al., 2018, Aoyagi et al., 2015, Fearon et al., 2012). These changes in turn produce fatigue and muscle deconditioning which further stimulates breakdown of these tissues, as well as reducing the efficacy of exercise and physical therapy as treatments for cachectic muscle atrophy (Dodson et al., 2011). Animo acids from proteolysis and fatty acids from lipolysis are both processed in the liver, which in cachectic patients undergoes steatosis, increased gluconeogenesis, and urea cycle dysregulation, further

exacerbating the metabolic dysfunction present in cachexia (Petruzzelli and Wagner, 2016, Porporato, 2016, O'Connell et al., 2021). While tumor- and immune-derived factors like reasonable mechanistic triggers for aberrant metabolism, circulating cytokine levels are not necessarily correlated with CAC incidence, and reduction of individual cytokines alone via antibody therapy is insufficient to relieve cachectic symptoms (Fearon et al., 2012, Petruzzelli and Wagner, 2016, Prado and Qian, 2018). Ultimately, CAC is the result of a complex web of feedback systems which are likely still not completely understood, making the treatment of any one aspect insufficient once the cascade begins. However, targeting key mediators of multiple aspects may result in a synergistic relief of symptoms (Aoyagi et al., 2015, Dodson et al., 2011, Fearon et al., 2012, Kalantar-Zadeh et al., 2013).

Treatment of CAC continues to be a significant opportunity for cancer care. CAC incidence is high, especially in cancers which have the lowest survival rate, and CAC hinders the ability to treat cancer patients. There are currently no effective clinical treatments for CAC despite significant recent efforts to understand the underlying mechanisms and expand therapeutic options. The complex, multi-systemic nature of CAC makes it challenging to address, but the vagus drives many key functions that are dysregulated in CAC, giving it a distinct advantage over symptom-oriented or single-element therapies which have been previously investigated.

1.3 Therapeutic Peripheral Nerve Stimulation

Electrical stimulation of the peripheral nervous system is a growth area in clinical research with the potential to provide therapies for otherwise intractable conditions, reduce off-target effects from systemically delivered pharmaceutical agents, and mitigate many of the costs associated with hospitalization and chronic drug treatment (Pelot et

al., 2020, Deshmukh et al., 2020, Johnson and Wilson, 2018, Carrington et al., 2014). The therapeutic potential of these treatments has generated great excitement and spurred several initiatives by federal agencies and the biotech and pharmaceutical industries including the NIH SPARC and DARPA ElectRx initiatives. Numerous applications for PNS are under investigation, including for rheumatoid arthritis, chronic pain, chronic heart failure, obesity, diabetes, Parkinson's and many others with promising outcomes across a tremendous number of applications (Johnson and Wilson, 2018, Liu et al., 2017, Koopman et al., 2016, Abraham and Smith, 2013, Chakravarthy et al., 2015, Malbert et al., 2017, Payne et al., 2019, Yao et al., 2018, de Lartigue, 2016).

1.3.1 Sacral Nerve Stimulation

Sacral nerve stimulation (SNS) is an FDA approved therapy for treatment of urinary and fecal incontinence as well as treatment-resistant chronic constipation (Fallahzadeh Abarghuei and Karimi, 2022, Šlauf and Vobořil, 2021, Tilborghs and De Wachter, 2022). It is also under investigation for treatment of chronic diarrhea, irritable bowel syndrome, and chronic pain (Roybal et al., 2021, Bharucha et al., 2017, Fassov et al., 2019). Sacral nerve stimulation remains a possible therapeutic for numerous diseases impacting sensation, control, and functionality of the pelvic organs, particularly the bladder and the lower GI tract.

However, significant concern remains regarding the clinical efficacy of SNS; limited studies on the ideal stimulation parameters and implantation site have resulted in somewhat arbitrary selections. Regardless of the desired downstream impact on GI function (accelerated transit in constipation or delayed transit in diarrhea or incontinence), frequency and magnitude of electrical stimulation are identical (Fallahzadeh Abarghuei and Karimi, 2022, Fassov et al., 2019, Šlauf and Vobořil, 2021).

While implantation is routinely performed at the S2 foramen based off of initial application for urinary incontinence, innervation of the colon and ileum may be more extensive from other sacral dorsal root ganglia (DRGs) or even pelvic nerves emerging at the lower lumbar levels (Šlauf and Vobořil, 2021, Tilborghs and De Wachter, 2022, Barth et al., 2017, Barth and Shen, 2018).

1.3.2 Vagus Nerve Stimulation

Vagus nerve stimulation (VNS) is an FDA approved therapy for treatment-resistant focal epilepsy and treatment-resistant major depressive disorder, episodic cluster headaches, migraine pain, hemicrania continua, and paroxysmal hemicrania (Chakravarthy et al., 2015, Deshmukh et al., 2020, Groves and Brown, 2005, Johnson and Wilson, 2018). VNS is under additional investigation as a clinical tool for treatment of diabetes, anxiety disorders, dementia, alcohol addiction, chronic heart failure, arrhythmia, autoimmune diseases, and chronic pain conditions (Groves and Brown, 2005, Johnson and Wilson, 2018, Chakravarthy et al., 2015, Abraham and Smith, 2013). Multiple studies have reported promising outcomes following vagal nerve manipulation for treatment of obesity-associated metabolic syndromes in clinical trial and preclinical studies (Göbel et al., 2017, Yao et al., 2018, Malbert et al., 2017). Notably, VNS is used clinically to achieve both vagal activation and vagal block depending on the desired effect. VNS for epilepsy and depression, for example, rely on vagal activation, and vagal activation is the predominant form of VNS under investigation (Johnson and Wilson, 2018, Krahl, 2012, Groves and Brown, 2005). Treatments for cluster headaches, migraines, and hemicrania, however, rely on vagal block, as do some proposals for treatment of metabolic disease and pain (Payne et al., 2019, de Lartigue, 2016, Tajti et al., 2019, Mwamburi et al., 2017).

Vagus nerve stimulation (VNS) provides a promising means to “reset” aberrant signaling along the gut-brain axis. The recent introduction of transcutaneous VNS delivery systems for clinical use makes VNS a particularly appealing approach, providing benefits without the need for expensive and risky surgical implants (Mwamburi et al., 2020, Mwamburi et al., 2017, Butt et al., 2020).

2. Intravital Windows for Real-Time Chronic Gut Imaging

Intravital microscopy is a powerful tool for visualizing biological processes in live organisms (Alieva et al., 2014). Intravital imaging has a distinct benefit over many alternative techniques; *in vitro* systems are ideal for microscopy, but often lack the complexity of *in vivo* systems and fail to recapitulate crucial elements of the system of interest, whereas tissues of interest *in vivo* are typically difficult to visualize due to their position within the host organism. Intravital imaging provides direct access to these tissues through optically clear windows, a significant improvement over *ex vivo* imaging or imaging of sections as it enables chronic repeated treatment and imaging of the same tissue (Huang et al., 2021). This both improves scientific rigor and availability of data by allowing data to be taken longitudinally without disrupting the study and eliminating inter-subject variability which might otherwise obscure subtle differences. Additionally, this technique reduces the resources required to perform experiments, making research more affordable and encouraging ethical reduction of animal use without disrupting scientific goals by creating a system where single animals can serve as their own controls and/or be used for data collection at multiple time points.

Techniques to intravitally image brain (Goldey et al., 2014, Holtmaat et al., 2009), spinal cord (Farrar et al., 2012), liver (Ritsma et al., 2012), lung (Entenberg et al., 2018), skin (Lehr et al., 1993, Maeda and DaCosta, 2014), intestine (Ritsma et al., 2014, Rakhilin et al., 2016), kidney (van den Berg et al., 2020), pancreas (Nobis et al., 2017), and others (Huang et al., 2020, Alieva et al., 2014). Figure 1 highlights some of these tools.

Prior to the windows I developed, no such window existed for colon (Rakhilin et al., 2019) or embryo (Huang et al., 2020). These targets are particularly difficult to image

due to their highly changeable nature; the colon experiences significant distension and is highly sensitive to obstruction, and embryos grow and move significantly during their developmental window. In this section I describe these tools and their use in detail.

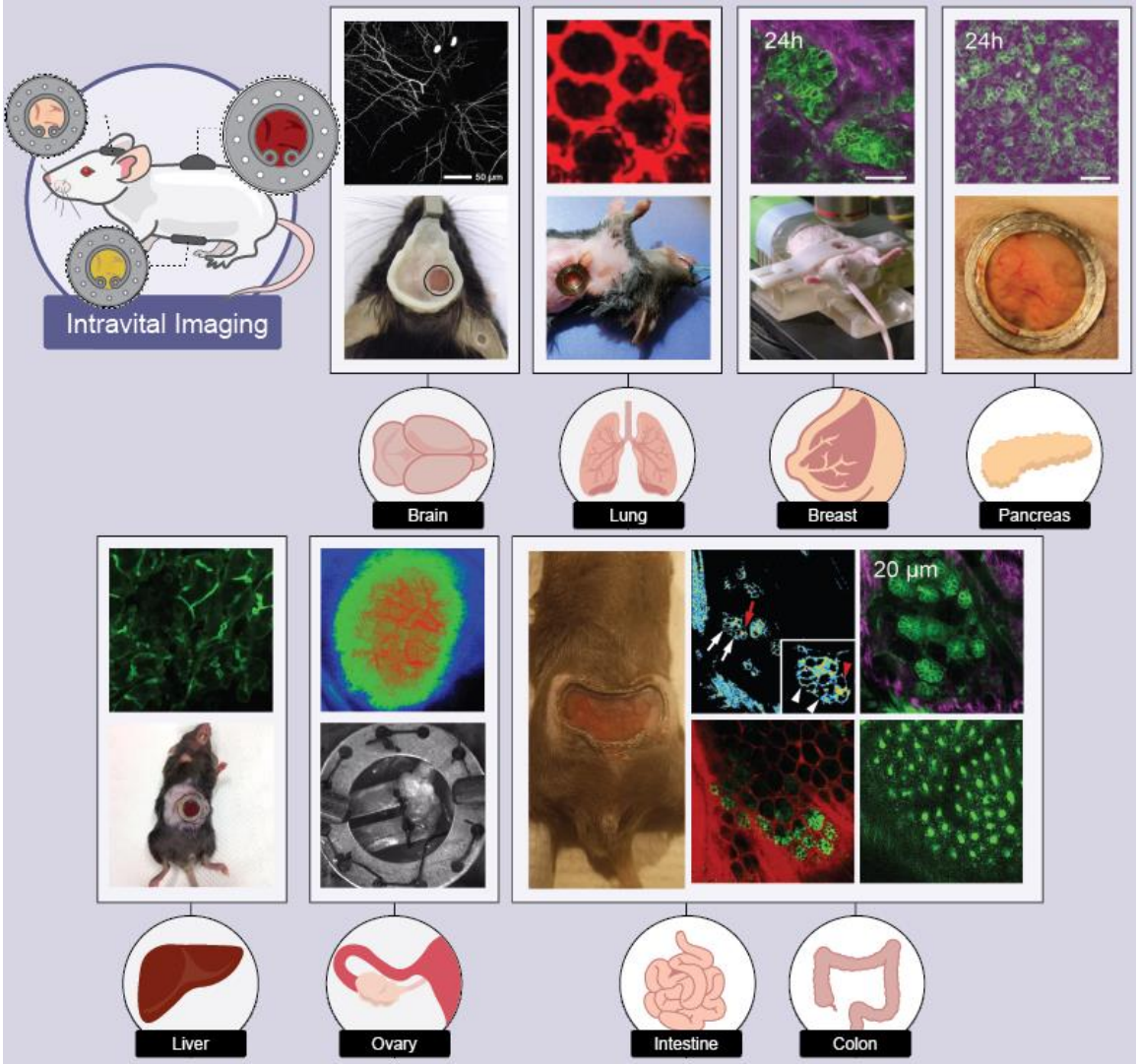

Figure 1: Intravital imaging windows.Representative imaging windows (IWs) and intravital microscopy (IM) images: brain IW and IM (Luckner et al., 2018); lung IW and IM (Lelkes et al., 2014); breast IW (Huang et al., 2021); breast IM (Nobis et al., 2017); pancreas IM (Nobis et al., 2017); pancreas IW (Huang et al., 2021); liver IW (Huang et al., 2021); liver IM (Nobis et al., 2017); ovary IW and IM (Bochner et al., 2015); intestine and colon IW and IM (Huang et al., 2021). Adapted from (Huang et al., 2021).

2.1 Colon Window

An intravital colon window has multiple clear applications; visualizing epithelial stem cell populations, immune response to inflammatory injury, and neural circuitry mediating colonic function are all areas of great interest with direct application to human health and disease. The colon is part of the lower GI, with crucial roles in absorption of salt, water, and nutrients from chyme (Furness, 2012, Furness, 2008). More than half of the body's gut microbiome resides in the colon, supporting digestion of polysaccharides into short-chain fatty acids, producing vitamins, and supporting homeostasis (Hillman et al., 2017, Jandhyala et al., 2015). Complex microbiota-immune reactions take place at the mucosal barrier of the colon, guiding healthy gut response provided fast-cycling LGR5-positive stem cells maintain barrier integrity (Barker et al., 2007). Failure to maintain this barrier can result in infection or inflammation; IBD, ulcerative colitis, and Crohn's disease are all pervasive diseases caused by dysfunction of GI inflammation (Kaplan, 2015).

The colon contains two interconnected ganglionated neuronal plexuses, the submucosal and myenteric, which comprise the colonic ENS. The human ENS consists of over 100 million neurons and regulates motility, vasodilation, and secretion, as well as performing sensory functions and communicating interactions with the immune system (Rao and Gershon, 2016, Furness, 2012, Furness, 2008). However, relatively little is known about how this is achieved in real time, with the mechanisms coordinating such behavior yet to be fully elucidated (Furness, 2012, Furness, 2008, Barth et al., 2017, Rakhilin et al., 2016).

Malfunction of this critical system can lead to a variety of conditions including functional gastrointestinal disorders (FGID), common examples of which include IBS,

fecal incontinence, chronic constipation, chronic diarrhea, and others (Furness, 2012, Rao and Gershon, 2016, Furness, 2008). These conditions are incredibly common, with approximately 20% of the global population experiencing FGID (Barth et al., 2017, Lahner et al., 2013, Rao and Gershon, 2016). However, they are also challenging to treat; pharmaceutical interventions are often unsuccessful, partly due to a lack of fundamental knowledge regarding normal colonic function and response of the ENS to treatments (Paul and Basude, 2016, Talley et al., 2015, Lahner et al., 2013). A promising emerging alternative to pharmaceutical treatments is peripheral nerve stimulation (Iachetta et al., 2012, Kenefick et al., 2002, Payne et al., 2019, Wexner et al., 2010, Bonaz et al., 2017, de Lartigue, 2016, Malbert et al., 2017, Paulon et al., 2017, Yao et al., 2018). Sacral nerve stimulation (SNS) has been shown to be particularly effective for fecal incontinence and constipation, but little is known mechanistically about the impact of SNS on the ENS and colonic motility (Iachetta et al., 2012, Kenefick et al., 2002, Wexner et al., 2010).

Improvements to SNS efficacy are limited by a lack of knowledge regarding SNS-ENS interactions under different stimulation parameters, particularly chronically and at a single cell level (Carrington et al., 2014, Sharma et al., 2013, Dudding et al., 2009). This results in seemingly paradoxical decisions in treatment, such as the use of identical stimulation parameters clinically to induce opposing effects in patients suffering from chronic constipation or chronic diarrhea. In this section I describe an intravital window for use in chronic imaging of the same location in the colon over multiple days, which I originally published on as co-first author (Rakhilin et al., 2019). This technology will enable examination of colonic behavior in a multitude of scenarios, expanding our

understanding of normal colonic physiology, etiology of disease, and response to therapeutic interventions.

2.1.1 Physical Specifications and Mode of Use

The colon window is comprised of four key physical elements; the window frame, the cover glass, the magnetic scaffold, and the imaging jig. The frame and glass form a single unit for implantation into the skin, with the scaffold implanted in the abdominal cavity. These items are autoclavable and able to be reused in multiple animals after thorough cleaning and heat sterilization between subjects. The imaging jig is important for use, but it is not implanted; a single jig may be used on multiple animals during serial imaging sessions as it is an exterior accessory.

2.1.1.1 Window Frame and Glass

I utilized a custom-designed colon window for visualization of spatiotemporal dynamics of the colon (Figure 2). The window was designed in AutoCAD 2016 (AutoDesk) and 3D-printed from smooth titanium (Materialise) to reduce scarring and improve biocompatibility. The window's size and shape allow unimpeded visualization of the colon and unobstructed gastrointestinal transit as well as unencumbered leg movement (Rakhilin et al., 2019). The cover slip was laser-cut with a 30 W CO_2 laser (Epilog, Zing) from borosilicate heat-resistant UV fused-silica glass wafers (Mark Optics, Corning 7980) specifically to fit the custom window design.

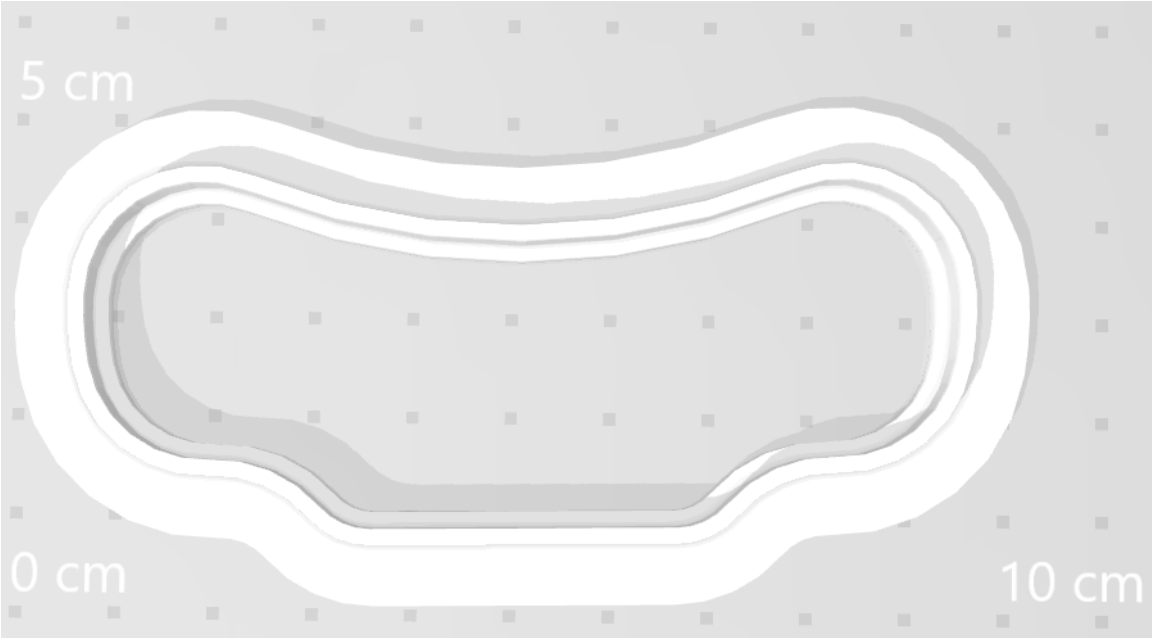

Figure 2: Rendered windowed scaffold.The geometry of the scaffold enables coverage of the full width of the abdominal cavity without impeding leg motion or impinging on the diaphragm.

2.1.1.2 Ferromagnetic Scaffold

Perhaps the greatest challenge when imaging the colon is minimizing motion artifacts. Intrinsic motor patterns driving peristalsis and grand migrating contractions are essential for normal gastrointestinal function, and restricting that motion chronically is invariably fatal; attempts to utilize a static scaffold resulted in bowel obstructions that were invariably fatal within two days. To resolve this challenge, I used an 11.5 x 3.5 x 1.5 mm ferromagnetic scaffold (Figure 3) designed in AutoCAD (Autodesk) and machined it out of 416 ferromagnetic steel (AZO materials, UNS S41600).

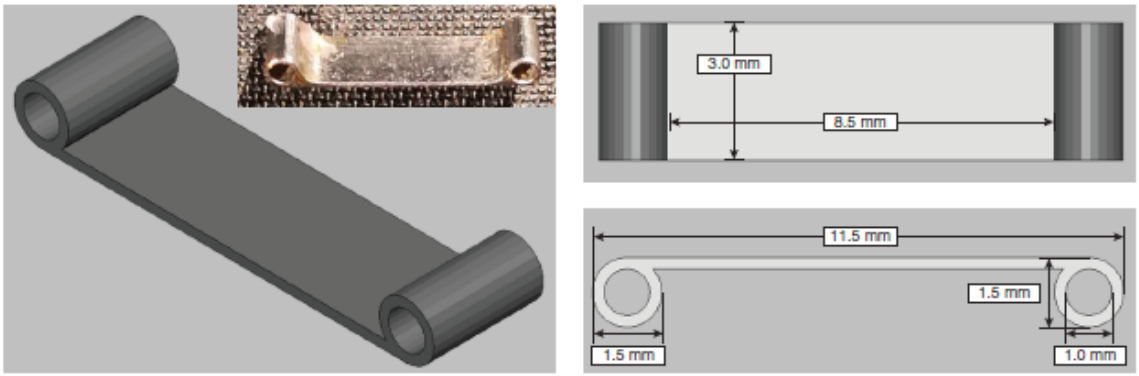

Figure 3: A ferromagnetic scaffold for the colon window.Left is an isometric rendering of the device with inset photograph of a machined scaffold. Right are two drawings of the scaffold with dimensions notated. The body is a simple bar, with suture hooks on either end.

2.1.1.3 Surgical Implantation

Implants and surgical equipment for these procedures were autoclave sterilized prior to use. Animals were anesthetized with isoflurane (4% isoflurane by volume in oxygen for induction and 2% isoflurane by volume in oxygen for maintenance) gas. Optical lubricant was applied to prevent corneal damage. Mice were injected with bupivacaine (0.25% <2 mg/kg) and meloxicam (2 mg/kg) subcutaneously prior to surgery. The surgical site was prepared by shaving the hair and sterilizing the site with three alternating washes of iodine and 70% ethanol.

A 15 mm circle of skin in the lower abdomen, over the colon, was removed. A 10 mm circle of peritoneal muscle centered in this segment was also excised. The ferromagnetic scaffold was inserted below the colon, with sutures passed between the scaffold and the abdominal wall with 4 – 8 mm of slack as illustrated in Figure 4. This slack suture enables scaffold displacement during colonic distension or motion of the animal, preventing obstruction of the bowel by the implant. The colonic surface is marked intraoperatively with a tattoo using an AIMS tattoo system (Braintree Scientific,

ATS-3 Q), serving as a wayfinding tool during subsequent imaging sessions. The tattoo enables easy visualization of colonic shifts from day to day and requires no special techniques to observe during imaging setup. Finally, the window is inserted such that the rim lies between the abdominal muscle and the skin and adhered to the surrounding tissue using Loctite 406 (Ellsworth, 135436).

Figure 4: Schematic of window implant.The window (grey) is implanted into the abdominal wall, with frame edges between the abdominal muscle and skin. The scaffold (green) is placed below the colon (red), with sutures between the scaffold and the abdominal wall above and below the window frame. When magnets are applied on the window surface, the scaffold is drawn upward, pressing the colon against the window glass and holding it still for imaging. When the magnets are removed, the scaffold floats freely below the colon and normal motion is restored.

Implanted mice were maintained without complication for multiple weeks, with imaging sites consistently identifiable by tattoo (Figure 5). Mice were provided additional post-operative analgesia 24 hours after implantation. Upon recovery animals show no

obvious indications of pain, discomfort, or impediment as evaluated by veterinary specialists. Mice with the implant have no problems with locomotion or grooming, and the window remains clear for imaging for multiple weeks. A veterinary pathologist has evaluated post-mortem colonic tissue harvested two weeks after tattoo and window implantation and determined there was no evidence of necrosis, degeneration, lesioning, or other abnormalities (Figure 6).

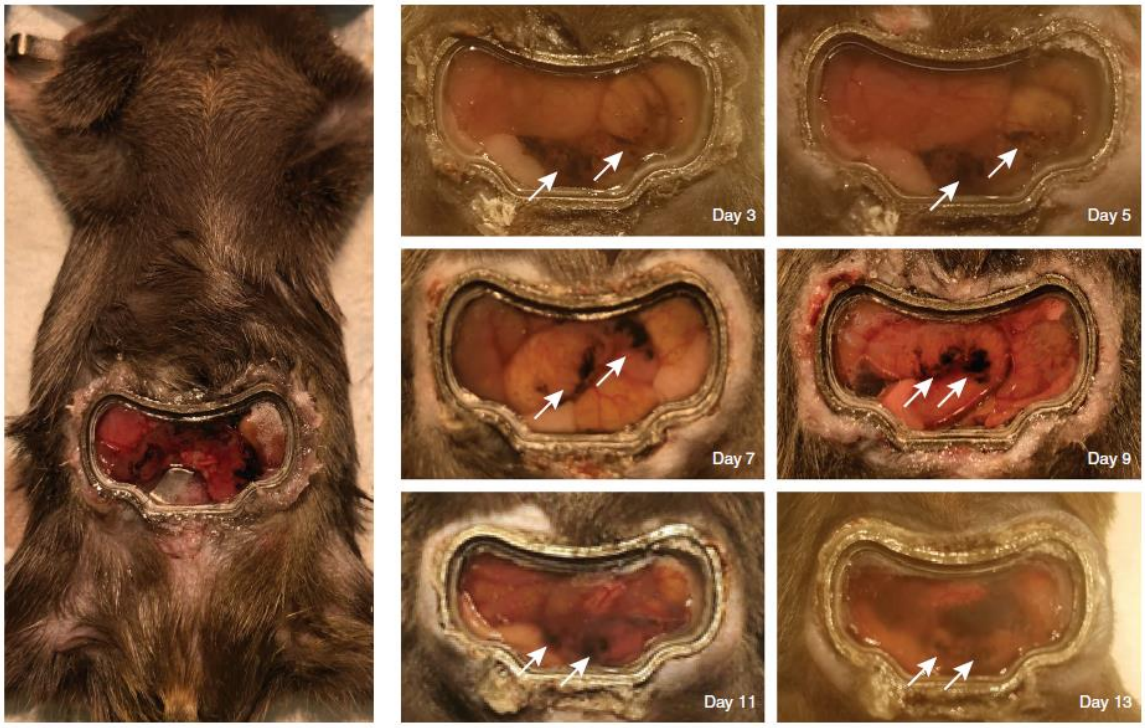

Figure 5: A C57BL6/J mouse implanted with colon window.Leftmost photograph is freshly implanted ("Day 0"), with other photographs marked with timepoint post-implantation. White arrows indicate visible tattoo locations.

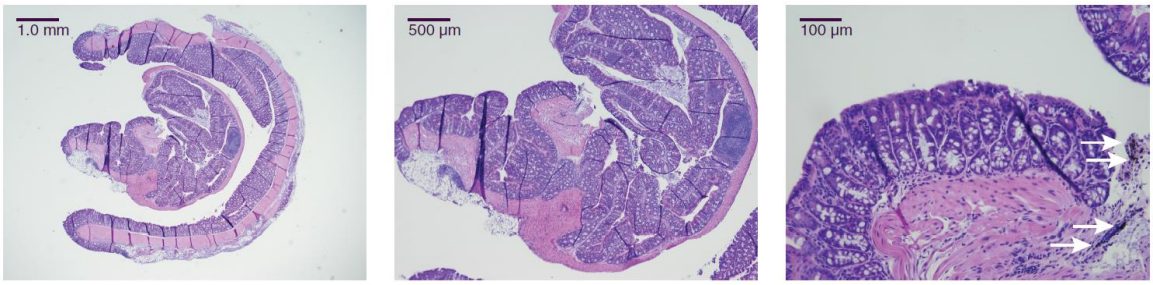

Figure 6: Photomicrographs of hematoxylin- and eosin-stained tattooed colon. The musculature and epithelium of the colon appear healthy and normal with no gross abnormalities. The far-right image, at highest magnification, has white arrows pointing at black inclusions in the colon wall; this is tattoo dye.

2.1.1.4 Window Holder and Intravital Imaging

In preparation for imaging, mice are anesthetized with isoflurane (4% by volume in oxygen for induction, 2% by volume in oxygen for maintenance). Mice are place supine onto the imaging stage with the window secured between 3D-printed window holders (Figure 7). Magnets (K&J Magnetics, D18) were placed on the window surface, positioned to draw up the ferromagnetic scaffold and restrain the colon against the inner window surface.

Figure 7: Render of a 3D-printed window holder.Two holders, one for each side, are mounted to form an imaging jig which holds the window stable and reduces motion artifacts caused by respiration.

Restraint of the colon resulted in an over three-fold reduction in motion and significant reduction in motion artifacts (Figure 8). Multiphoton microscopy was performed using a

Bruker Ultima IV, Zeiss LSM880, or Olympus FV1000, with at least one recovery day allowed between imaging sessions. Individual imaging sessions were kept to a maximum of two hours to reduce likelihood of isoflurane overdose.

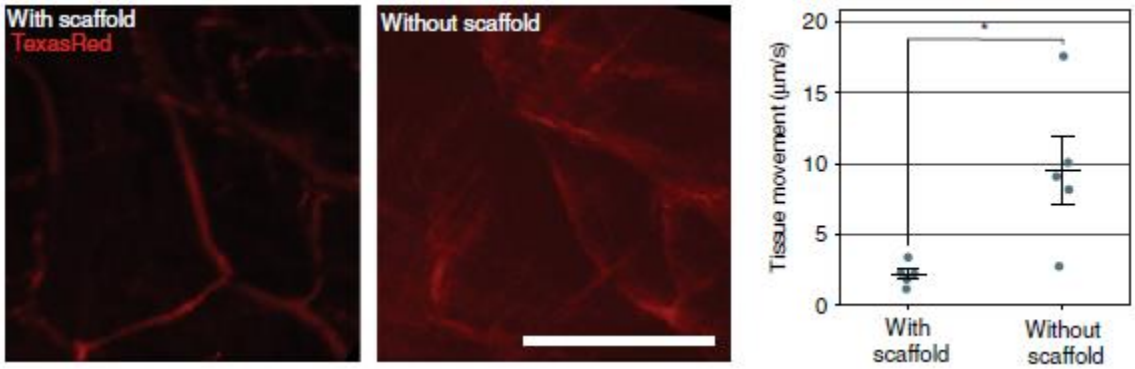

Figure 8: Engagement of ferromagnetic scaffold dramatically reduces motion artifacts.Left and center panels show representative sums of 150 consecutive frames of B6/J mouse vasculature visualized by TexasRed injection with the scaffold engaged or without. The image is significantly crisper, as the colon does not shift over the imaging period. Scale bar 100 μm. The rightmost panel is a quantification of tissue movement in microns per second in these images. Circles represent measurements from individual mice, with bars indicating mean ± SEM. Asterisk indicates statistical significance as evaluated by an unpaired, two-tailed t-test (n=5, $p < 0.05$). Scale bar 100 μm.

2.1.2 Intravital Imaging of Intestinal Stem Cell Rejuvenation

Maintenance of the colonic epithelium is critical for normal function, as this surface provides a barrier against the gut microbiome and ingested organisms, provides the surface area necessary for nutrient and water absorption, and produces mucous to lubricate the passage of waste (Barker et al., 2007). Lgr5-positive stem cells, which are reportedly radiation sensitive, are responsible for regeneration of these rapidly renewing cellular populations (Barker et al., 2007, Cheng and Leblond, 1974). These cells are also of interest in colorectal cancer, which is associated with Lgr5-positive stem cell proliferation induced hyperplasia (de Sousa e Melo et al., 2017, Baker et al., 2015). To

demonstrate the utility of the colon window for imaging colonic stem cells, I exposed Lgr5-eGFP transgenic reporter mice to 18 Gy irradiation and tracked the colon over five days in the same mice (Figure 9). Mice were irradiated in an XRAD 320 irradiator (Precision X-ray Inc., North Branford, CT) four days post-window implantation.

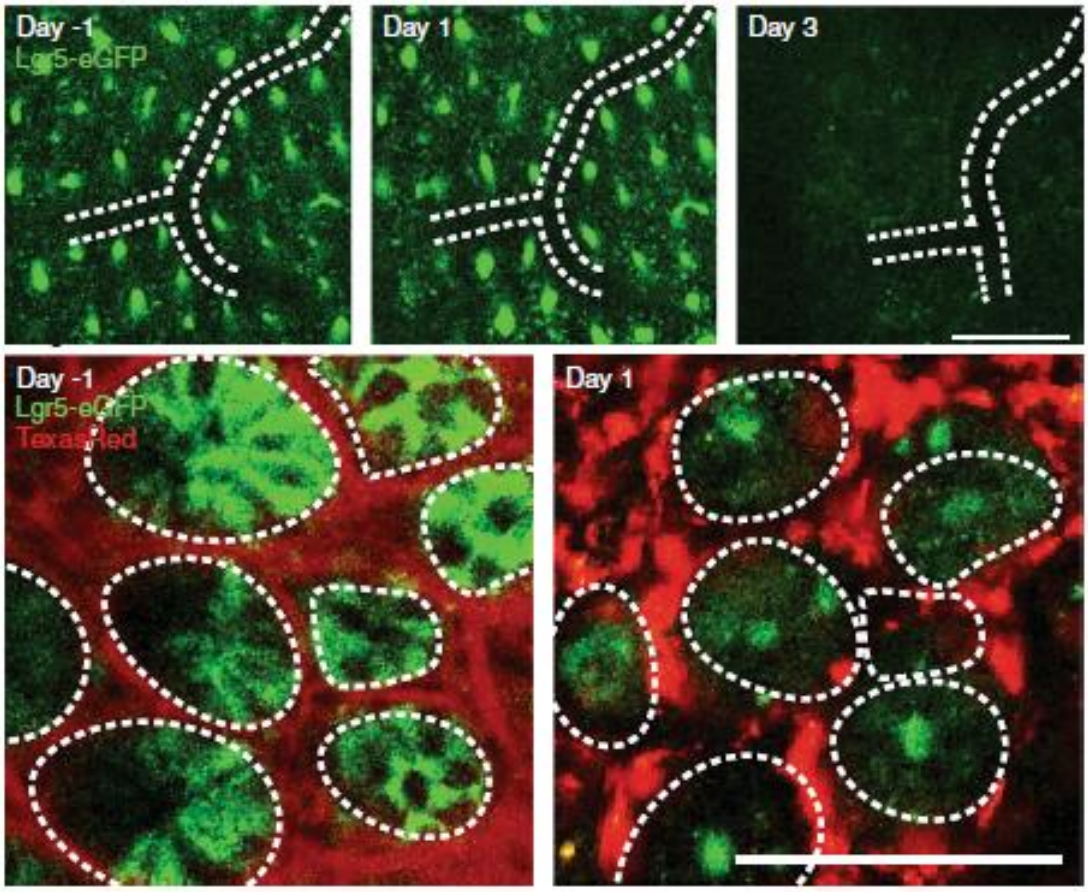

Figure 9: Representative images of Lgr5^{+} stem cells in mouse crypts. Initial images were taken the day before irradiation (Day -1), with subsequent images taken on Day 1 and Day 3 (dependent on mouse survival). Animals were either imaged using only the tattoo for guidance (top row) or with additional vascular landmarks visualized by injection of TexasRed vascular dye (bottom row). Lgr5^{+} stem cells (green) are prominent prior to irradiation, but the population declines over time. Morphological landmarks are indicated by dashed white lines. Scale bars 100 µm.

Unanesthetized mice were placed dorsally in a pie cage without restraints or shielding 47.46 cm from the irradiation source and exposed to 320 kVp, 12.5 mA X-rays through a 2.0 mm A1 filter. Imaging region was located during each session with help of a colon tattoo, with or without vascular dye administered as 100 uL 2.5% w/v Texas Red Dextran (Thermofisher, D1863) injected into the tail vein immediately prior to imaging. Imaging of identical regions on subsequent days enabled direct quantification of stem cell death based on both crypt area and number of Lgr5-positive cells per crypt (Figure 10). A statistically significant decrease in both size of crypts and Lgr5-positive cells per crypt supports the observation that Lgr5-positive stem cells are radiation sensitive and demonstrates the utility of this intravital window for tracking cellular populations over multiple days. This experiment supports the value of this technique for monitoring cell-type specific responses in isolated regions, such as during injury response.

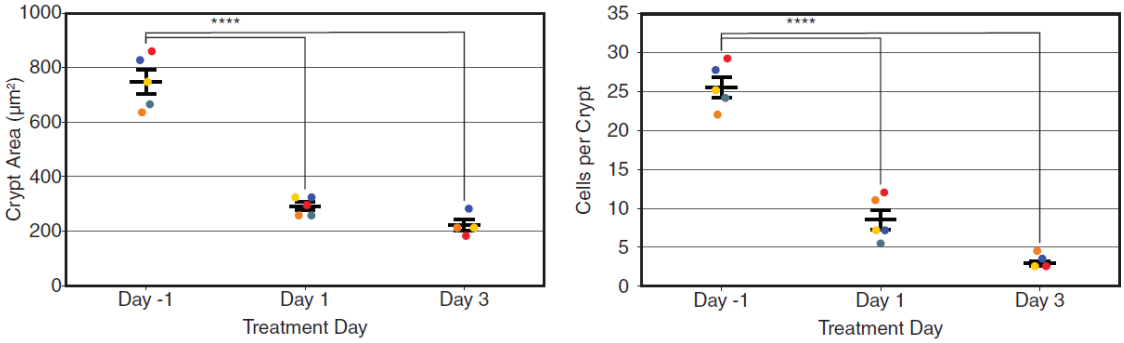

Figure 10: Quantification of Lgr5-positive cell abundance after irradiation. Left: Quantification of Lgr5-positive crypt area in μm^2, Right: Quantification of Lgr5-positive cells per crypt. Irradiation was delivered on Day 0. Circles represent individual mice (by color), with bars indicating mean ± SEM. Asterisks indicate statistical significance from control (unirradiated) by Dunnett's post-hoc test for multiple comparisons following repeated-measures ANOVA ($n \geq 4$, $p < 0.001$).

2.1.3 Imaging of Immune Response to Inflammatory Challenge

Chronic inflammation is a crucial aspect of many GI disorders, particularly IBD. Immune cells and enteric neurons are known to interact, modulating normal colonic motility and absorption as well as driving pathology during dysbiosis (Bonaz et al., 2017, Pinho and Frenette, 2019, Schneider et al., 2019). To establish the functionality of the window for observing immune cell activity, immune cell activation was imaged in a live, chronic model of murine colitis.

CX3CR1^{GFP} x CCR2^{RFP} mice were bred to label activated monocytes with a red fluorescent protein (RFP) and dendritic cells and inactivated monocytes with a green fluorescent protein (GFP) (Mizutani et al., 2012). Mice were then challenged with 2% w/v dextran sodium sulfate (DSS)(Alfa Aesar, J64606) in drinking water for 3-6 days. Texas Red Dextran (Thermofisher, D1863) was injected retro-orbitally immediately prior to imaging to visualize the vasculature, although high degrees of vascular disruption were noted secondary to prolonged DSS challenge (Figure 11). Leaky vasculature is a known feature of this model (Chassaing et al., 2014). As expected based on previous reports (Chassaing et al., 2014, Grimm et al., 1995, Okayasu et al., 1990), inflammatory challenge resulted in a dramatic increase in the number of activated monocytes infiltrating the colonic epithelium, demonstrating the ability of the colonic window for use in tracking immune-cell recruitment and activation during chronic inflammation.

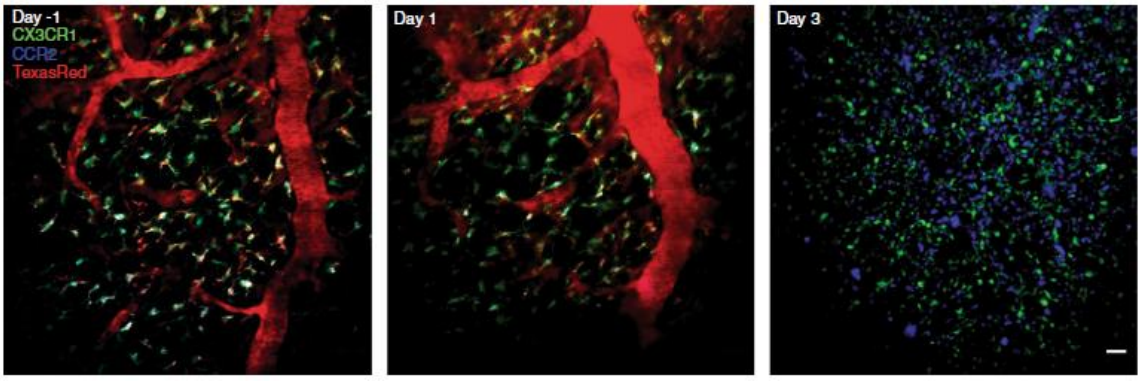

Figure 11: Immune cell activation and recruitment during DSS challenge. Representative images from a CX3CR1^{GFP} x CCR2^{RFP} mouse provided DSS-treated drinking water from Day 0 onward. Using a combination of colonic tattoo and vascular mapping a consistent location was imaged for vasculature (red), activated monocytes (blue), and inactivated monocytes and innate dendritic cells (green). Scale bar 100 µm.

2.1.4 Tracing Sacral Innervation of the Colon

The ENS is essential in regulating GI motility and immune function, with SNS emerging as a valuable too address motility and immune disorders including IBD and FGID (Carrington et al., 2014, Iachetta et al., 2012, Kenefick et al., 2002, Rakhilin et al., 2019, Sharma et al., 2013, Wexner et al., 2010, Kaplan, 2015, Payne et al., 2019). The value of this therapy is limited, however, without a complete understanding of its mechanism of action. One of the key unknowns is the relative innervation along the length of the gut by specific source locations, which continues to be a matter of debate in the field. While I address this question in more depth in our whole mouse atlas in Section 3, we performed several tracing studies using our abdominal window technologies to establish likely areas of impact for SNS.

Figure 12 shows AAV tracing of sacral innervation in wild type agouti mice. Oral gavage or intraluminal injection was used to introduce 200 µL of AAV9-hSyn-GCaMP3 at 1.0 x 10^5 virions/ml throughout the GI. This green fluorescence was broadly expressed in

the submucosal and myenteric plexuses of mice along the full length of the intestines and colon, serving as a visual marker for the ENS. 10 µL of AAV9-hSyn-TurboRFP at 1.0 x 10^5 virions/ml was injected into the S3 foramen for delivery to the sacral nerve. Red fluorescence is only detected in the lower GI (ileum, colon, and rectum), indicating areas of direct sacral innervation. Because these AAV9 constructs are asynaptic, that is, they are incapable of reproduction and infection of downstream cells, we see only cells and synapses which have processes or cell bodies, respectively, in the sacral nerve.

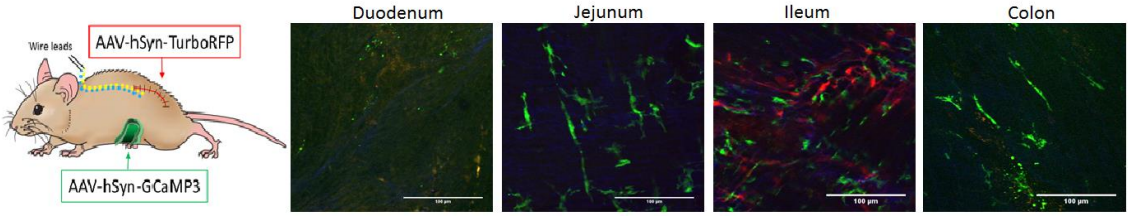

Figure 12: AAV-tracing of sacral innervation.AAV9-GFP administered inside the lumen of the mouse gut can be seen along the length of the digestive tract (green). AAV9-RFP injected into the S3 foramen, alongside the sacral nerve, can only be seen in the lower portion of the intestine, indicating that the sacral nerve only signals to this portion of the gut. Scale bars 100 µm.

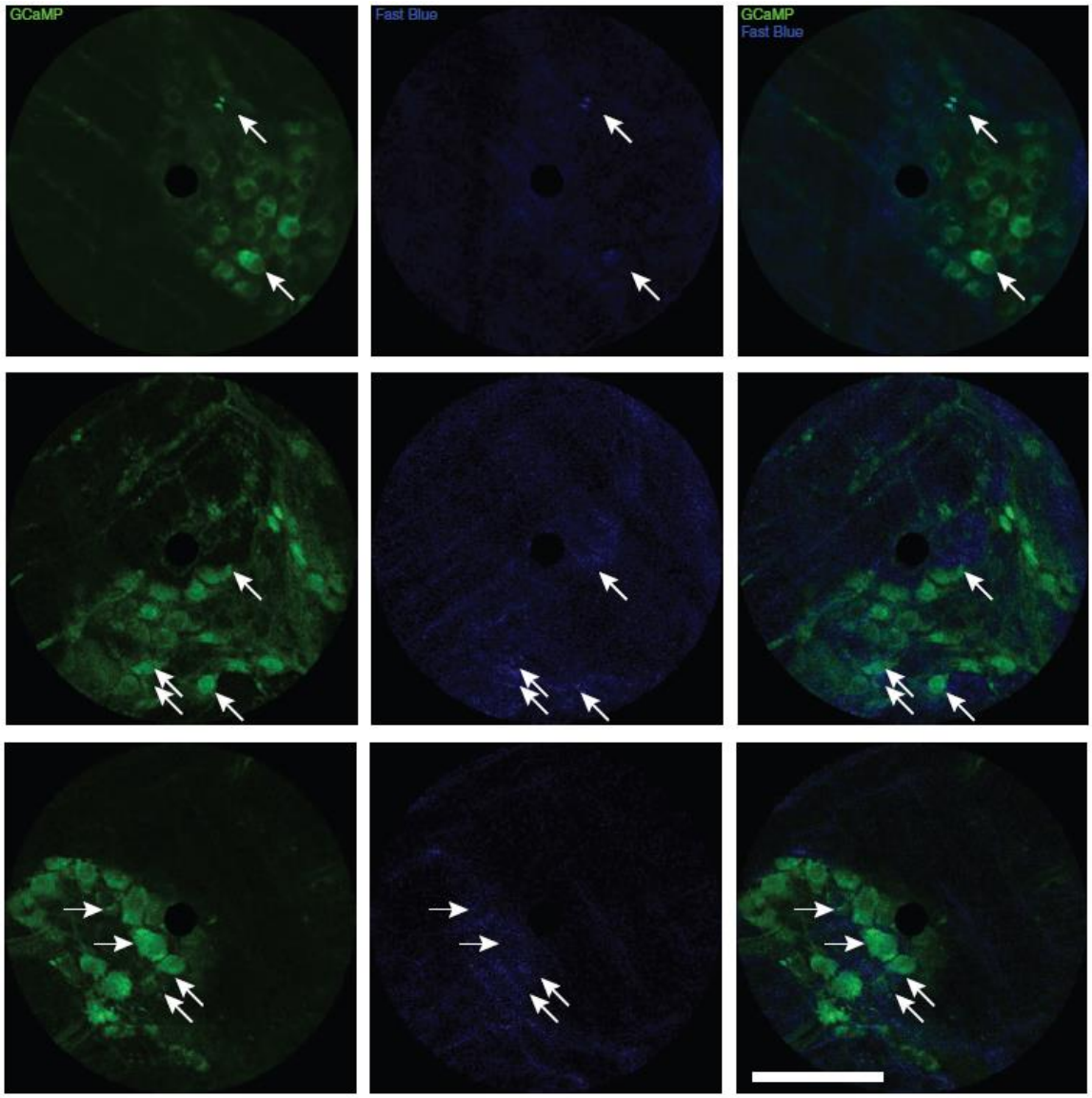

Figure 13: Fast blue tracing of sacral innervation in Pirt-GCaMP3 mice.Left: Pirt^{+} enteric neurons labeled with GFP (green). Center: Fast Blue labeled neurons with sacral projections (blue). Right: Overlay of both populations. Arrows indicate double-positive cells. Scale bar 100 µm.

We performed a similar tracing experiment using an asynaptic neuronal tracer dye, Fast Blue, in Pirt-GCaMP3 mice (Figure 13). 5 µL of 4 mM Fast Blue (Polysciences, 17740-1) was injected into the S2 foramen. Enteric neurons thus expressed green fluorescence with greater intensity during neuronal activation, while neurons with direct

connection to the sacral nerve expressed static blue fluorescence. This allowed us to visualize sacral innervation to the colon on a single cell level within individual ganglia and examine how cells with direct sacral innervation responded relative to their neighbors.

2.1.5 Enteric Neuron Response to Sacral Nerve Stimulation

To assess the local impacts of SNS on enteric neural activity, we implanted two cardiac pacing electrodes (Medtronic, 6494) as a scale appropriate analog for human SNS delivery leads. The stimulation electrode was placed into the S2 vertebral foramen and secured in place with Loctite 406 (Ellsworth, 135436), while the return electrode was placed subcutaneously lateral and dorsal to the sacrum and secreted with Loctite 406 as described in (Rakhilin et al., 2019). Leads were then tunneled subcutaneously to the back to the neck to allow access while reducing the ability of subjects to harm themselves by displacing the leads.

Confirmation leads did not drift over the course of the experiment was confirmed via X-ray fluoroscopy on the last day of the study (Figure 14). While under isoflurane anesthesia, mice were imaged with a GE OEC 9800 Plus C-arm X-ray machine. Images were taken during exhalation at 50% brightness and 60% contrast in both dorsal and lateral positions.

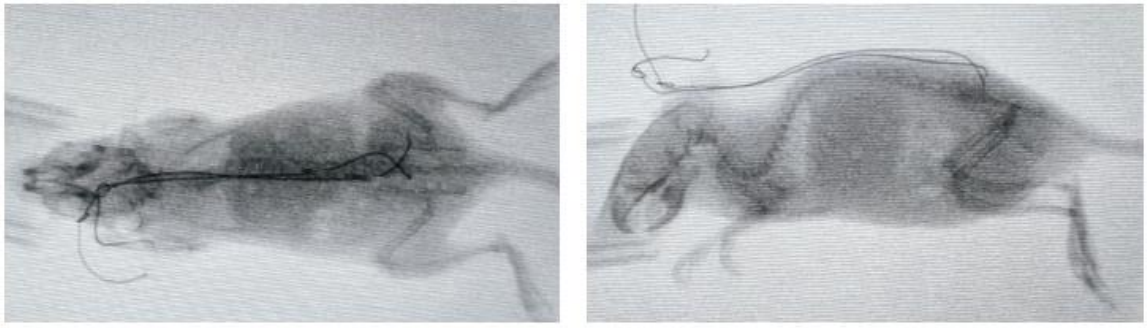

Figure 14: X-ray fluoroscopy of mice with SNS lead implants.A dorsal (left) and lateral (right) view clearly shows the stimulation lead inserted into the S2 foramen, with the return lead dorsal and lateral to this lead in the animal's lower back.

The ability of the window to reliably image a single location within the gut wall over a prolonged period for assessment of acute activity changes in enteric neurons during SNS was first established using a system with a static signal. Wnt1-tdTomato mice with endogenous, constant red fluorescence in the neurons and glia of the myenteric plexus were implanted with colon windows and imaged for 1.5 hours to ensure minimal drift during imaging (Figure 15).

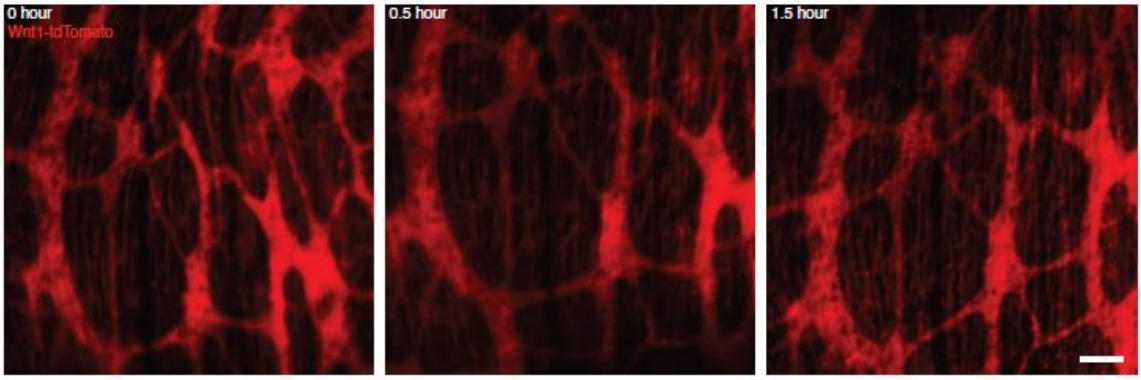

Figure 15: Visualization of colonic myenteric plexus over 1.5 hours. Representative *in vivo* imaging of Wnt1-tdTomato mice at initial time point, half an hour later, and 1.5 hours later demonstrating consistent visualization of landmarks over and extended imaging session. Scale bar 100 µm.

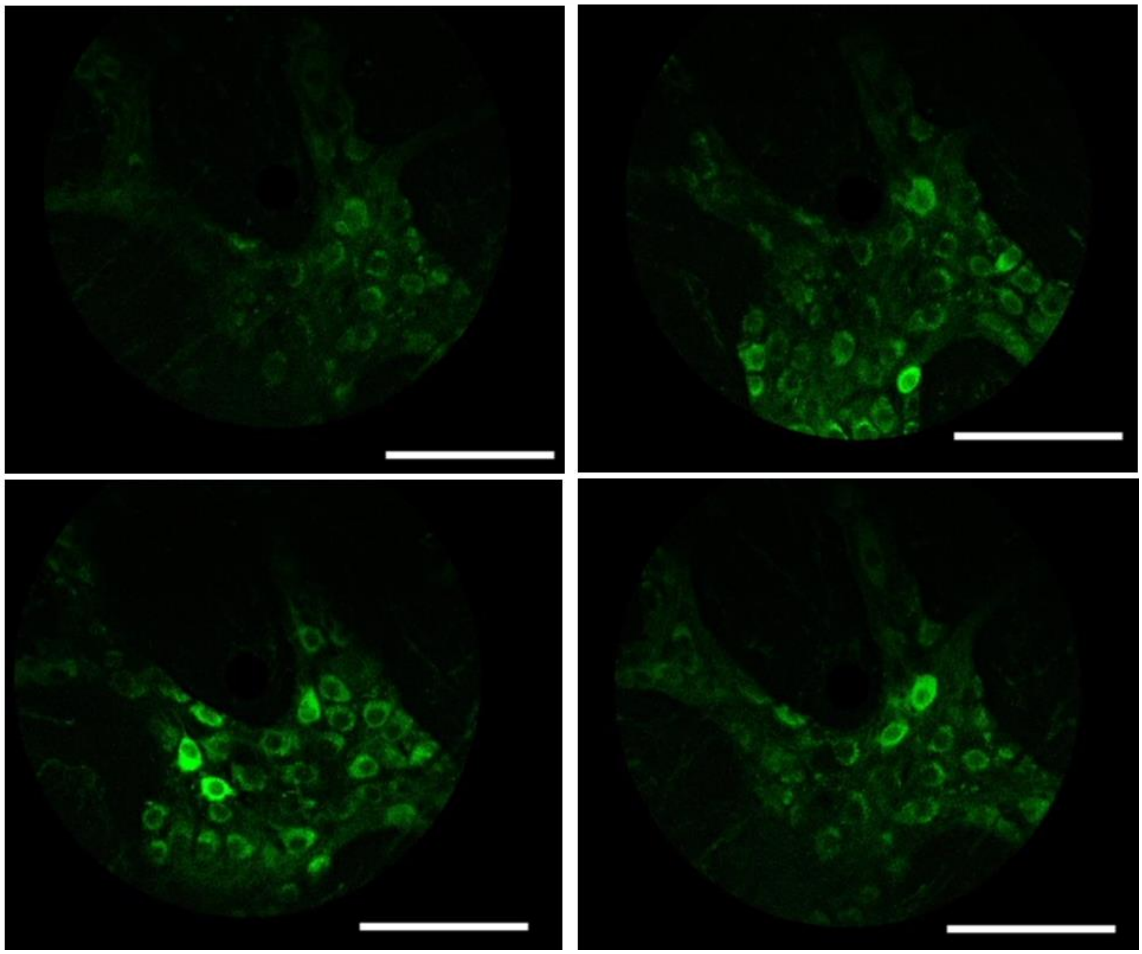

Figure 16: Response of neurons in a myenteric ganglion to SNS. Photomicrographs taken from a video of a Pirt-GCaMP3 mouse during SNS; in the first frame, low baseline fluorescence is observed in the neurons. In the subsequent frames, a sub-set of neurons are activated and have elevated green intensity. Scale bar 100 µm.

After establishing our ability to consistently capture the myenteric plexus using the colon window, we confirmed we could visualize and record calcium dynamics in GCaMP mice, which express higher fluorescence levels during neuronal activation as voltage gated ion channels open to induce a calcium flux during signaling (Figure 16). I have published videos of this activity (Rakhilin et al., 2019), but include here select still

frames to illustrate the visual change in fluorescence intensity when neuronal activation occurs. Electrical stimulation was delivered as biphasic current-controlled pulses from a biphasic stimulus isolator (Digitimer, DS4) drien by an arbitrary function generator (Tektronix, AFG1062) at 20% below motor threshold. Motor threshold was determined by gradually increasing current amplitude until a tail twitch was observed.

To quantify the neuronal response to SNS, ROIs were identified for each cell in the visual field in ImageJ. Fluorescence intensity of each cell was calculated in each frame for a 30 second window prior to stimulation, a 15 second stimulation interval, and 45 seconds following stimulation (Figure 17). F_0, the baseline activity level, was defined for each cell as the mean intensity for the pre-stimulus period. $\Delta F/F_0$, the fold change in intensity, was calculated as the instantaneous fluorescence intensity divided by the baseline intensity. Cell presentation within each animal in the calcium dynamic heat map is organized based on response magnitude, with those having the highest increase in activity over the recorded period at the top and those with the lowest on the bottom. We performed stimulation at several different frequencies to assess changes this made to the type and magnitude of neuronal response. 14 Hz stimulation, the clinical norm, evoked a statistically significant response compared to sham controls which did not receive stimulation but did receive implants, whereas 7 Hz and 21 Hz stimulation failed to produce a similarly robust response. This may be due to the stimulus frequency matching the frequency of the gut's native "pacemaker cells," interstitial cells of Cajal (ICCs) (Barth et al., 2017, Camborová et al., 2003).

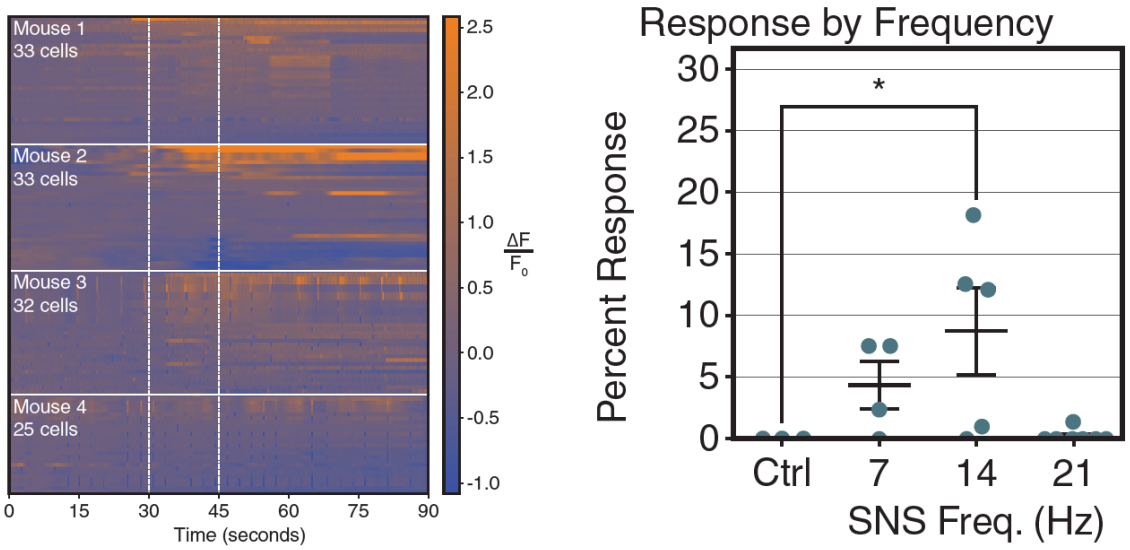

Figure 17: Quantification of calcium dynamics during SNS.Left: Calcium dynamics of at least 25 cells from 4 mice before, during, and after delivery of 14 Hz SNS (delivery period marked by vertical dashed white lines). Right: Quantification of percent of cells with a significant deviation from baseline (average pre-stimulus baseline level). 14 Hz stimulation evokes a statistically significant response when compared to unstimulated mice, but 7 Hz and 21 Hz stimulation do not. Asterisk denotes statistical significance by Dunnett's post-hoc test for multiple comparisons after ANOVA (p<0.05).

Notably, while many cells are unresponsive on an individual level, up to 20% of cells experience significant changes from baseline. Not all cells with altered activity level have increased activation, however; some cells (such as those shown at the bottom of the heatmap for Mouse 2) experience reduced fluorescence, indicating that SNS has an inhibitory effect on some neuronal populations. This hints at the complex neural circuits that modulate GI activity, with clinically relevant FGID occurring when the ENS is underactive as well as when it is overactive.

Staining for neuronal sub-populations along the length of the gut post-mortem suggests that SNS activates different neuronal populations dependent on location within the gut. For these studies, rats were implanted with SNS electrodes as described earlier in this

section. Two days after implantation, the rats receive painless SNS titrated to 10% less current than necessary to evoke a tail twitch response while awake and unanesthetized, gently restrained in clear plastic restraint cones. After 30 minutes of SNS, animals are euthanized by CO_2 overdose and perfused with PBS followed by 4% PFA. PFA perfused colonic segments were harvested and cleaned of luminal contents using a gavage needle and PBS wash. The colon was cut open along the mesentery and laid flat in a 10 cm plastic culture dish filled to a 1 cm depth with cured Sylgard 184 (Millipore Sigma, 761036). Edges of the tissue were held in place with stick pins and forceps were used under a dissecting microscope to peel away the mucosa, leaving the longitudinal muscle and myenteric plexus (LMMP). Samples were then washed with PBS and stained for 24 hours with rabbit anti-nNOS (Thermofisher, 61-7000) and chicken anti-cFos (Sigma, GW21144) antibodies, both at 1:500 dilution. Stained images of proximal (Figure 18) and distal (Figure 19) colon reveal that proximal neuronal activation (as evident by nuclear cFos expression) is not in inhibitory neurons (as evident by a lack of NOS staining in the cell bodies); the activated neurons are likely acetylcholine (ACh) mediated excitatory neurons. In the distal colon, however, cFos and NOS staining is mutually inclusive rather than mutually exclusive, indicating SNS activates inhibitory neurons in the distal colon rather than excitatory neurons. This variation in response along the spatial axis of the gut highlights the need to examine the response of heterogeneous neuronal populations in response to therapies treating the ENS.

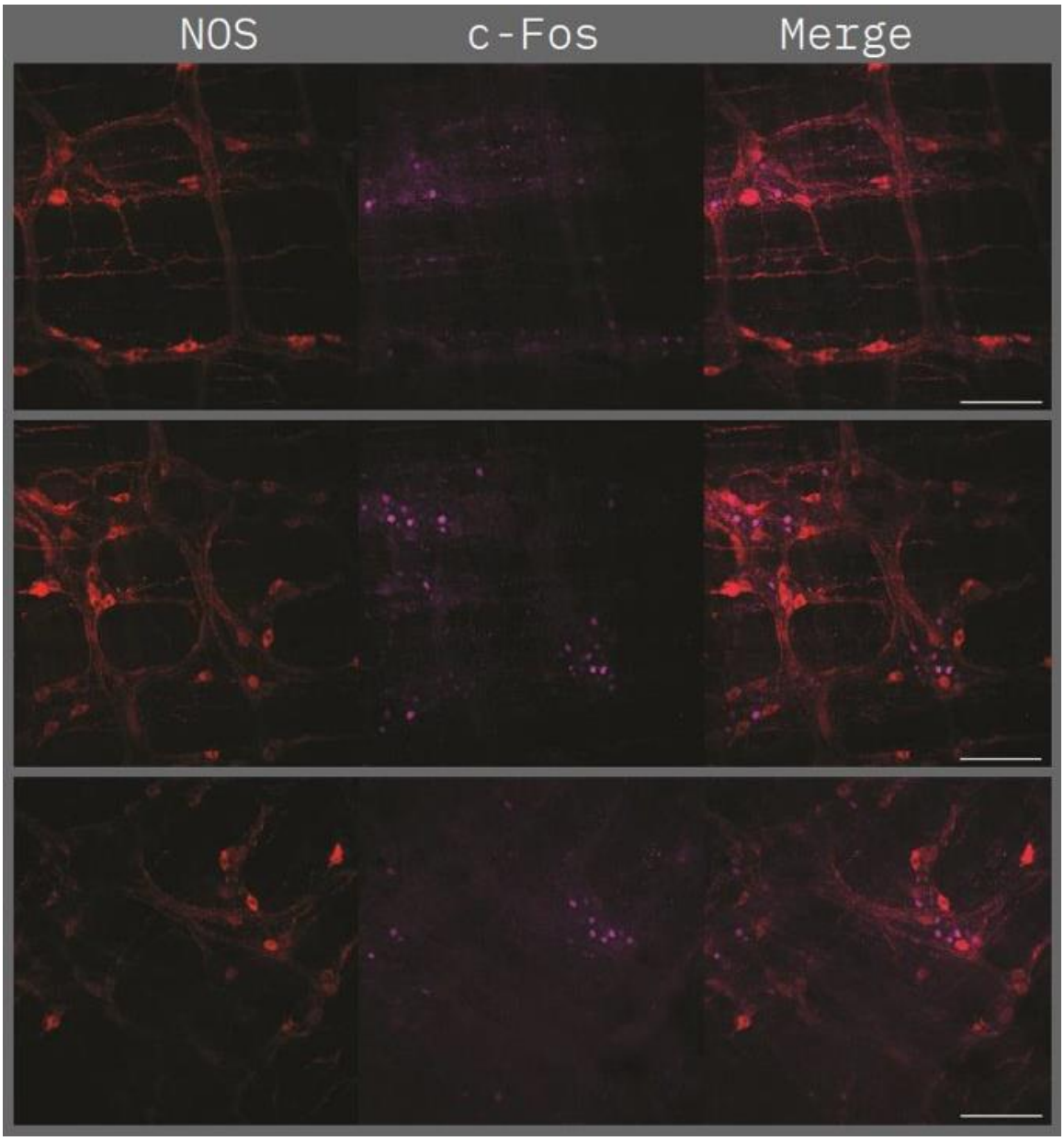

Figure 18: SNS exclusively activates NOS- neurons in the proximal colon. Images from a single rat after 30 minutes of awake sacral nerve stimulation. Red staining identifies NOS-positive neurons; purple staining identifies cFOS-positive neurons. Virtually all c-Fos-positive neurons are NOS-negative, virtually all NOS-positive neurons are c-Fos-negative. These populations being mutually exclusive indicates that SNS activates primarily excitatory neurons in the proximal colon. Scale bars 100 µm.

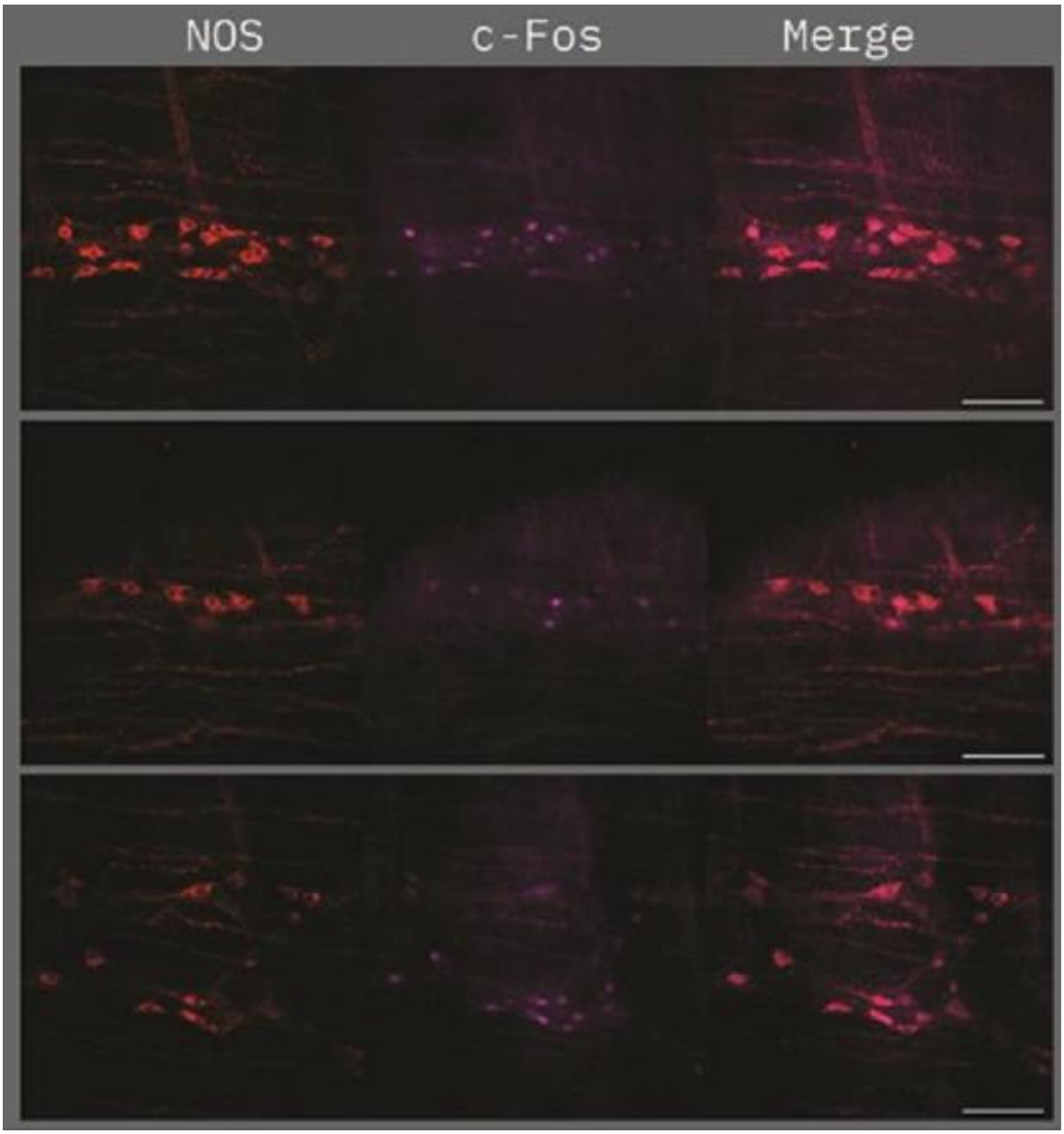

Figure 19: SNS exclusively activates inhibitory neurons in the distal colon. Images from a single rat after 30 minutes of awake sacral nerve stimulation. Red staining identifies NOS-positive neurons; purple staining identifies cFos-positive neurons. Staining for NOS and cFos is mutually inclusive; virtually all cFos-positive neurons are NOS-positive, indicating that SNS activates predominantly inhibitory neurons in the distal colon. Scale bars 100 µm.

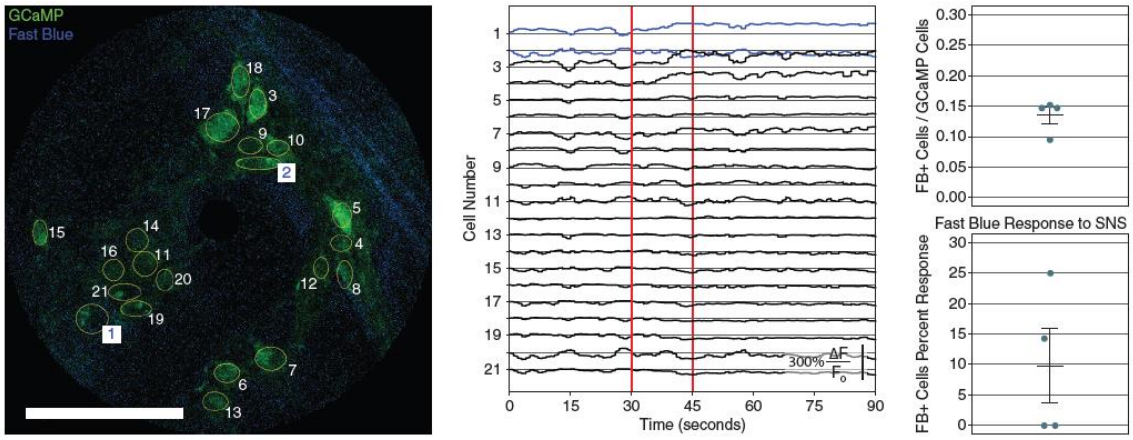

Figure 20: Response of cells with sacral connection to SNS.Left: Representative photomicrograph of a myenteric ganglia of a Pirt-GCaMP3 mouse with Fast Blue injected into the S3 foramen. GCaMP (green) expression is identified in 21 cells with labeled ROIs; 2 Fast Blue positive cells are identified with blue on white labels for their ROIs. Scale bar 100 µm. Center: Changes in GCaMP fluorescence from cells labeled in the photomicrograph in response to 14 Hz SNS (delivered in the time indicated by vertical red bars). Right top: Quantification of fraction of GCaMP-positive cells labeled with fast blue (n=4 mice). Right bottom: Quantification of percent of Fast Blue positive cells which response to SNS (n=4 mice). Circles represent individual mice, with bars indicating mean ± SEM.

To elucidate on whether cells with direct sacral connections had notable differences in their activation patterns in response to SNS relative to their nearest neighbors, I performed SNS while imaging the myenteric neuronal activation in Pirt-GCaMP3 mice implanted with windows and injected with Fast Blue dye to the S2 foramen as previously described (Rakhilin et al., 2019). Figure 20 shows a representative image demonstrating the quantification process, as well as the numerical summary of these studies. Like the quantification described in Figure 17, individual ROIs were identified for each neuron within the field of view. Instantaneous fold change in intensity relative to baseline was established for each neuron, with Fast Blue positive neurons explicitly noted. Fast Blue positive neurons were relatively rare within the quantified population, making up on average about 14% of the quantified neurons.

Degree of response to SNS was variable, however, ranging from no change to a 25% activation or inhibition rate. The rate of response amongst these cells was comparable to that of the general population of enteric neurons, suggesting that these cells likely contain a mixed population of motor neurons receiving signals from the CNS via the sacral nerve and sensory cells with afferents in the sacral nerve communicating gut conditions to the CNS with similar relative incidence of cell types to that of the global ENS population.

2.2 Embryo Window

Mice are a common embryonic development model with a handful of approaches for study with a variety of limitations (Piliszek et al., 2011). Fixed embryo imaging can be done at high resolution with numerous molecular markers, but this is limited by the fixed temporal point at which fixation occurs. Meanwhile, ultrasound and MRI can be repeated at multiple timepoints along development, they have limited resolution and cannot take advantage of transgenic strains with fluorescent reporters and molecular contrast agents available for these imaging technologies are limited (Huang et al., 2021). Early-stage peri-implantation embryos can be imaged *ex utero* in culture medium for up to 48 hours but maintaining embryos from embryonic day 9 (E9) onward has yet to be successful despite efforts to mimic the intrauterine environment (Shahbazi and Zernicka-Goetz, 2018). These developmental stages from E9-birth (typically E19.5-E20.5) are crucial, however, with most organogenesis occurring after this point and significant neuronal development and migration including to the gut occurring in this phase.

Intravital imaging has had clear value for progress visualizing deep organs and tissues longitudinally but had not been applied to embryonic imaging prior to the seminal window design I produced for a collaboration with members of the Shen lab (Huang et

al., 2020, Huang et al., 2021). I've produced two distinct windows with application to different embryonic states on implantation for imaging from E9.5 to birth to support investigation of embryonic development.

2.2.1 Circular Window for Imaging Murine Embryos

The circular window for murine embryonic imaging from E9.5 forward was designed in AutoCAD 2016 (AutoDesk). The window consists of three main elements – a titanium frame, a coverslip, and a plastic clip to secure the cover glass (Figure 21). The window frame was 3D-printed from titanium (Materialise). Cover glass was cut to fit the frame from borosilicate heat-resistant UV fused-silica glass (Mark Optics, Corning 7980) with a 30W CO_2 laser (Epilog, Zing). The clip is 3D printed from ABS plastic on an Ultimaker 2+ 3D printer. The cover glass sits in a raised lip in the frame with a press fit clip holding the window in place as described in (Huang et al., 2020). The clip system allows for direct access and manipulation of embryos during development, such as to introduce experimental pharmaceuticals, viral vectors, CRISPR gene editing constructs, fluorescent labels, or other compounds of interest directly into the embryo without additional surgical procedures.

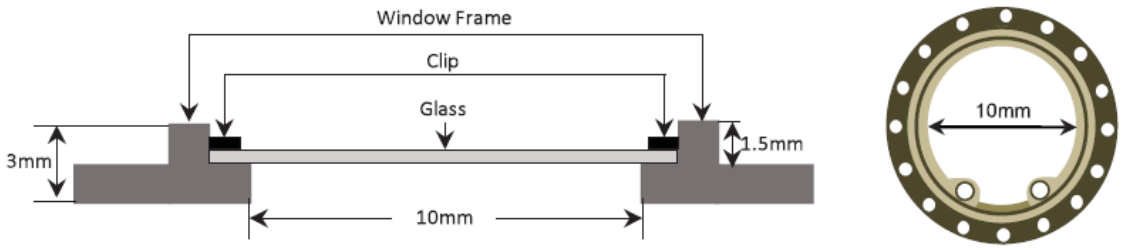

Figure 21: Schematic of the circular embryo window for E9.5 and older.The window has a 1 cm cross-sectional profile for the cover glass with a 3 mm outer ring featuring anchor holes for sutures.

The window is implanted by making a midline incision in the shaved, clean abdomen of a mouse under 2% w/v isoflurane anesthesia. The site is sterilized with three alternating swabs of iodine and 70% ethanol. A small section (~5 mm in diameter) of abdominal muscle is then removed to allow access to the embryos. An embryo close to the ovary is selected and the uterine wall is sutured to the abdominal muscle surrounding the incision site. The abdominal muscle is then sutured to the anchors on the window, and the incision is closed by adhering the skin to the top of the window border with Loctite 406 (Ellsworth, 135436). Analgesia is provided as described for the colon window, providing bupivacaine and meloxicam subcutaneously during the immediate recovery period (Rakhilin et al., 2019). Figure 22 shows the embryo window implanted *in vivo* to allow visualization of embryos at several stages from E9.5 through E13.5.

Figure 22: Circular window allowing direct visualization of embryonic pups. From left to right, the windows show pups at E9.5, E10.0, E12.5, E13.0, and E13.5. Pups are outlined with a dashed yellow line in the E9.5 and E10.0 stills to aid with visualization.

2.2.2 Elliptical Window for Imaging Murine Embryos

Embryos of E15.5 and up typically exceed 1 cm in length, necessitating a larger window to enable imaging of multiple sites across the whole embryonic form. While the smaller window is more appropriate for imaging embryos before E11.5 due to their small size and sensitivity to thermal stress, a larger elliptical window design accommodates

visualization of whole embryos until birth (Figure 23). The materials and manufacture of this elliptical window are the same as those for the circular window. The surgical procedure for implantation is similar as well, with the only major difference being a larger incision made on implantation, removing a 5 mm x 10 mm section of abdominal muscle rather than a 5mm diameter circle.

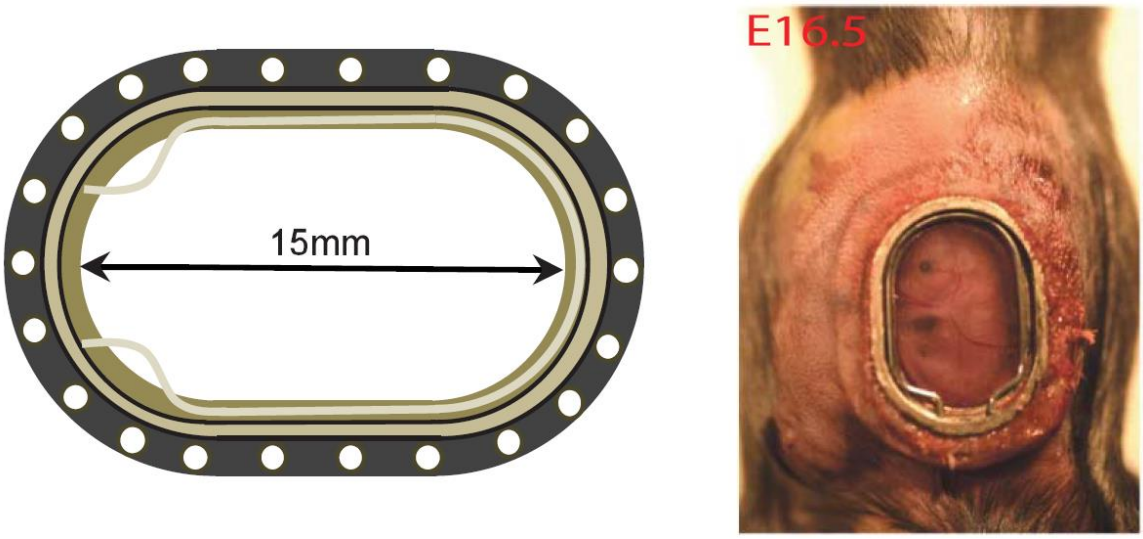

Figure 23: Elliptical window for whole embryo visualization until birth.Left: schematic of the elliptical window, which has a maximum coverslip width of 15 mm and maximum height of 10 mm. Right: implanted elliptical window, with E16.5 pup visible beneath.

2.2.3 Pups Imaged In Utero Are Viable for Postnatal Studies

Pups imaged via the window not only seem to be developmentally normal when assessed based on known developmental landmarks from previous studies that did not make use of an intravital window, the pups are viable after birth (Huang et al., 2020). Dams with window implants engage in normal feeding and care of pups following delivery. While pups which developed below the window are slightly smaller than their littermates (Figure 24), after birth these animals develop and behave normally to adulthood without excess mortality.

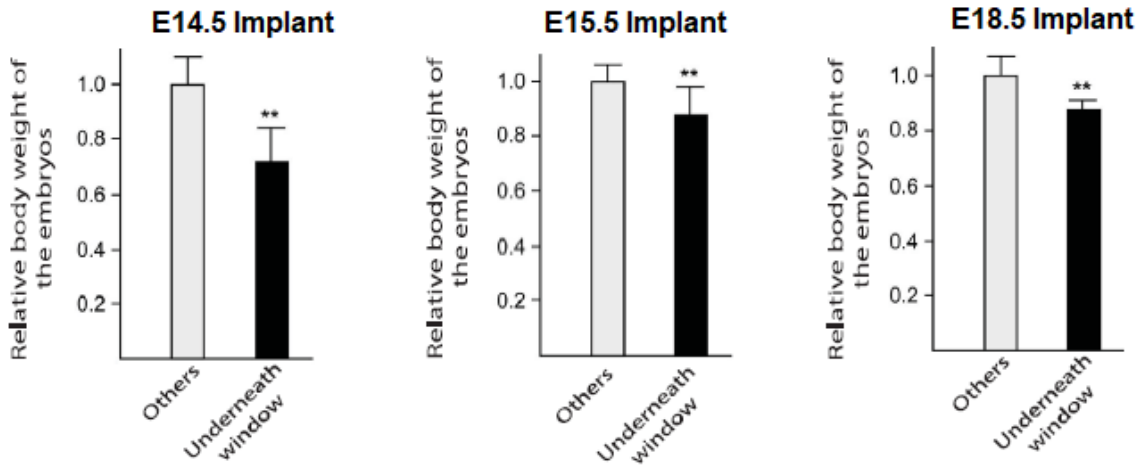

Figure 24: Embryos imaged through the window are viable, but slightly smaller than littermates.Graphs show weight presented as mean ± SD for normal pups versus pups placed under the window (3 litters per condition). Dams were implanted at E14.5, E15.5, or E18.5 for this study, and pups were collected 3 days after the window was implanted. ** indicates $p < 0.01$.

3. Mapping the Peripheral Nervous System in an Intact Mouse via Compressed Sensing Diffusion Tensor Magnetic Resonance Imaging

The PNS is comprised of numerous nerves which are responsible for sensation, motor control, and constant two-way communication of the body's status between the brain and other tissues (Garrett et al., 2021, Liu and Xu, 2019). The main elements of the PNS are the dorsal roots originating in the spine and the cranial nerves originating from the brain, which progressively form smaller tight fiber bundles containing sensory efferents and motor afferents (Yuan and Silberstein, 2016, Haberberger et al., 2019, Spencer et al., 2016b, Johnson and Wilson, 2018). Each fiber is surrounded by the perineurium, a membrane that protects the fibers from tensile and compression stresses and acts as an insulator for electrical signals (Morris et al., 2017).

The PNS has two main elements – the autonomic nervous system and the somatic nervous system. The somatic nervous system drives voluntary actions, while the autonomic controls reflexes and unconscious behaviors which support homeostatic function. The autonomic nervous system is comprised of the sympathetic and parasympathetic systems, which act in balance to control all involuntary processes.

The two main parasympathetic branches between the brain and the abdominal organs are the sacral and vagus nerves (Browning and Travagli, 2014). The vagus innervates the spleen, upper GI, lungs, and heart, and has known roles in inflammation, respiration, cardiovascular function, nociception, and appetite (Browning et al., 2017, Yuan and Silberstein, 2016, Rakhilin et al., 2016). The sacral nerve originates from the sacral roots that exit the sacral foramen, connecting the bladder and colon to the spinal

cord where it plays important roles in voiding and continence (Spencer et al., 2016b, Carrington et al., 2014).

Sympathetic signaling largely occurs via the splanchnic nerves. The greater splanchnic nerves are the primary sympathetic innervation source for the liver, stomach, and small intestine (Browning and Travagli, 2014, Amir et al., 2020). The colon is innervated by the lesser splanchnic nerves, while the kidneys are innervated by the least thoracic and lumbar splanchnic nerves (Miller and Szurszewski, 1997, Fazan et al., 2002, Sata et al., 2018). Meanwhile, the heart and lungs are innervated by the cardiopulmonary nerves of the sympathetic chain ganglia (Hasan, 2013, Chang et al., 2015, Hilton et al., 2017). These nerves often have long, indirect paths between the brain and target tissues, with frequent branching and formation of complex extraspinal plexuses which complicate straightforward start to finish tracing, resulting in inadequate understanding of the innervation of key organs (Abell et al., 2015, Johnson and Wilson, 2018, Rakhilin et al., 2019). This lack of fundamental knowledge significantly impedes research into clinical therapies such as nerve regeneration, neural blockade, and peripheral nerve stimulation.

The traditional approach to analyze peripheral nerve tracts is via tracing with neural specific dyes, AAV, or other neuron-specific viruses such as modified rabies and herpes viruses which are tagged with fluorescent reporters or pigments (Naso et al., 2017, Kaplan and Vatter, 1959, Wickersham et al., 2013). However, visualization of these markers is typically limited to 1 mm or less during microscopy, and visualization of small fibers is often challenging so neural bundles are analyzed histologically only at the origin of large nerve fibers or the terminal tissue, not along the full pathway (Huang et

al., 2021). Tissue clearing techniques such as iDISCO, CUBIC, and CLARITY have enabled imaging of fluorescent markers at increased depths, but these techniques tend to quench native fluorescence in transgenic reporter lines and antibody-based methods to identify nerves in thick tissues remain underwhelming due to issues diffusing antibodies evenly as well as the destruction or modification of epitopes of interest during the clearing process (McKey et al., 2020, Renier et al., 2014, Du et al., 2018, Matsumoto et al., 2019). Even with tissue clearing, however, current limitations in microscopy technology most light sheet microscopes restrict imaging to superficial level, with few models able to accommodate samples more than a few centimeters deep, making them impractical for whole organism tractography (Chu et al., 2019, Combs and Shroff, 2017, Huang et al., 2021).

Magnetic resonance imaging (MRI) has proved a revolutionary tool in clinical medicine. In research settings the fundamental principles used in hospitals and clinics worldwide have been used to develop magnetic resonance microscopy (MRM), a high resolution imaging platform using stronger magnetic field gradients, perfusion of contrast agents, and sampling and reconstruction algorithms to achieve micron-scale resolutions (Ciobanu and Pennington, 2004, Johnson et al., 1993, Johnson et al., 2002). Diffusion tensor imaging (DTI) is a technique that encodes movement of protons in aqueous solution during MRI to reconstruct high-resolution structural information about the tissues (Jeon et al., 2018, Lope-Piedrafita, 2018). By examining motion during multiple magnetic gradient orientations, a tensor can be calculated for any point in the subject volume which can be diagonalized to provide magnitude and direction of diffusion and used to calculate the principal eigenvector for a given voxel, thus revealing directionality of fiber

structures such as neuronal projections (Calabrese et al., 2015, Jeon et al., 2018, Jiang and Johnson, 2010, Lope-Piedrafita, 2018, Mori et al., 2001). Nerves are an ideal tissue for such imaging due to their compact nature, uniform directionality, and insulation by the perineurium and the myelin sheathe of myelinated neurons. This highly structured form results in highly directed diffusion of water and cytoplasm within these nerves, which is distinct from adjacent tissues. Dedicated research scanners have previously been used to map neural tractography in the rodent brain, but whole-body acquisition has been prevented due to the long acquisition times necessary for high resolution scans (Mori et al., 2001, Allan Johnson et al., 2019, Jeon et al., 2018).

Herein I describe the first application of an image acquisition and reconstruction algorithm created at the Duke Center for In Vivo Microscopy to peripheral nerve mapping, allowing for an 8-fold reduction in acquisition time compared to traditional DT-MRI without loss of resolution, originally published in the Journal of Neuroengineering (Garrett et al., 2021). This study resulted in the first whole mouse peripheral nerve atlas generated from an intact animal, as well as the first quantitative tractogram of the peripheral nervous system, highlighting relative innervation of the major abdominal and thoracic organs by the vagus nerve or nerves originating at each spinal vertebra and providing a useful tool for researchers wishing to specifically target downstream tissues with neuromodulation therapies.

3.1 Generation of a Peripheral Nerve Atlas

Scanning was completed using a compressed sensing scanning algorithm on a 7 T research MRI (7 T horizontal-bore magnet driven by a GE Excite console, General Electric Healthcare). The compressed sensing scanning utilized a 3D Stesjkal Tanner

spin-echo pulse sequence with repetition time (TR) of 100 ms, echo time (TE) of 23.189 ms, and b-value of 2000 s mm^{-2} (Garrett et al., 2021). An acquisition matrix of 1000 x 400 x 400 over a 70 mm x 28 mm x 28 mm field of view was used to capture a whole 23 g adult mouse mounted in a custom birdcage coil for radiofrequency transmission (Figure 25). Diffusion sampling was completed for 46 unique diffusion angles and five non-diffusion weighted baseline (b0) measurements with an 8-fold compression factor. The final isotropic spatial resolution for the whole mouse was 70 µm.

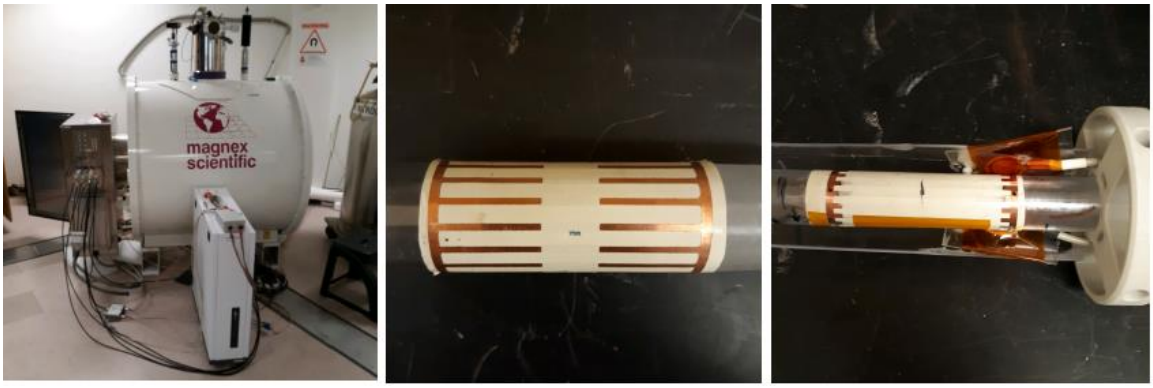

Figure 25: DT-MRI acquisition setup for whole mouse tractography.Left – GE 7T research MRI unit. Center – inverted custom birdcage coil showing the interior material patterning. Right – Homemade low pass birdcage coil using a custom dielectric, mounted with pickups. The mouse is placed in the center of the coil, and the coil is centered in the magnet chamber for optimal field exposure.

Conventional scanning of the whole mouse would have taken 226.4 hours, whereas the compressed scanning sequence enabled capture in just 28.3 hours (Garrett et al., 2021, Wang et al., 2019). This is critical because while the high resolution is necessary to detect and trace fine nerve tracts, extended scan times can produce artifacts due to heating and warping of the sample (Wang et al., 2019, Garrett et al., 2021), a key barrier to peripheral nerve tractography on this scale in the past.

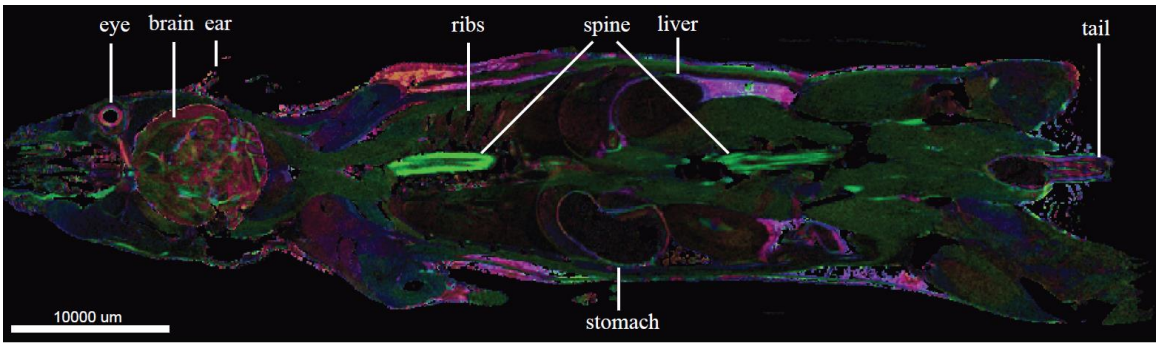

Figure 26: Coronal fractional anisotropy cross section of whole mouse MRI. Colors indicate the relative fractional anisotropy values of the tissue; dorsal-ventral alignments are blue, medial-lateral alignments are red, and rostral-caudal alignments are green. Several clear landmarks are notated in white for orientation.

Image reconstruction was performed in DSI studio (Figure 26). A diffusion sampling length ratio of 1.25, a deconvolution ODF sharpening of 5.0, and an eight-fold ODF tessellation were used in the DTI reconstruction. Masking was done manually to isolate tissues of interest for tractography; ROI spheres of influence of 1-2 mm in diameter were used as references for the dorsal root ganglia (DRGs) and vagus nerve, while larger volume solids were constructed to encompass the full spine and organs of interest. Pathways were isolated via deterministic tractography using a threshold of 0.17, angular threshold of 70, step size of 0.04, smoothing of 0.3, minimum length of 0.3 mm, maximum length of 800 mm, and maximum tracks shown value of 1,000. Tract density images were exported from DSI Studio for visualization and analysis in Imaris (Figure 27).

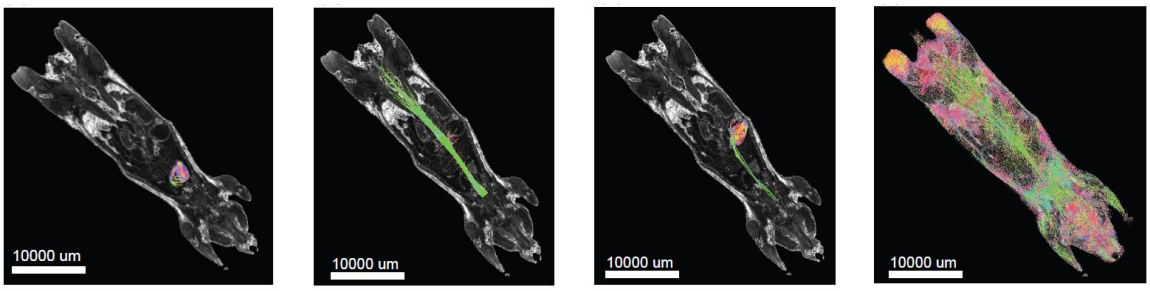

Figure 27: Representative tractography visualization.Left to right: tractography of the heart, tractography of the spinal cord and DRGs, tractography of the stomach and esophagus, tractography of the whole mouse PNS.

3.2 Validation of Deterministic Tractography via Light Sheet Microscopy

While DT-MRI is routinely used to generate connectomes in the brain, it has rarely been applied to the periphery in part due to the challenges heterogeneous tissues introduce to validation and parameter selection for reconstruction and tractography (Calabrese et al., 2015, Jeon et al., 2018, Jiang and Johnson, 2010, Lanzman and Wittsack, 2017, Mori et al., 2001). This work represents the first such application of DT-MRI at this scale, so validation using a conventional imaging technique – specifically fluorescence imaging of the mouse leg via light sheet microscopy – was performed.

Parameters such as angular threshold and anisotropic threshold are crucial for differentiation of small diameter nerve fibers from surrounding tissues, especially fibrous tissues such as muscle (Jeon et al., 2018). While these parameters are determined by the physical properties of the tissues and have a limited range of biologically viable values, small variations impacted by the MRI equipment used can have profound impacts on the calculated tractography (Table 1). This includes variations in identified total nerve fiber length, number of fibers identified, and even the final destination of a given fiber. This is further illustrated in Figure 28.

Table 1: Impact of angular threshold and step threshold parameters on length and number of nerve fibers identified.Biologically viable angular threshold values (50 to 70) and step threshold values (0.160 to 0.175) were swept during tractography between the spine and an arbitrary ROI in the abdomen. Identical seed regions were used as start and end points, but different mean fiber lengths (first number, µm) and numbers of fibers (parenthetical second number) were identified. The green-highlighted cell uses the validated parameters generated in this study.

		Angular Threshold				
		50	55	60	65	70
Step Threshold	0.160	920 (5)	864 (5)	870 (5)	874 (5)	881 (5)
	0.165	154 (2)	175 (3)	181 (3)	176 (3)	175 (3)
	0.170	34 (1)	37 (1)	36 (1)	35 (1)	33 (2)
	0.175	34 (1)	37 (1)	36 (1)	35 (1)	33 (2)

To directly visualize peripheral nerve structure and intelligently select parameters to ensure deterministic tractography agreed with ground truth, we performed modified iDISCO+ clearing of the experimental mouse after DT-MRI scanning (Figure 29) as previously published (Garrett et al., 2021). Briefly, the skin was removed from the mouse and the remaining tissues were incubated in 66% dichloromethane (DCM) / 33% methanol overnight on a rocker. The mouse was then washed twice for 15 minutes with 100% methanol and chilled to 4 ˚C. Tissues were next bleached in 5% hydrogen peroxide in methanol overnight at 4 ˚C. Tissues were subsequently incubated in anti-Tuj1 antibody (abcam, ab18207) and anti-SMA antibody (Sigma, C6198) for 5 days. Next, tissues were incubated in 66% DCM/33% methanol for 3 hours while rocking at room temperature followed by two additional washes in 100% DCM for 15 minutes each. Finally, the mouse was incubated in dibenzyl ether (DBE) and flipped three times to

ensure total immersion in the solution. The mouse was stored in DBE in an opaque container and imaged on a LaVision Ultramicroscope II (Figure 30).

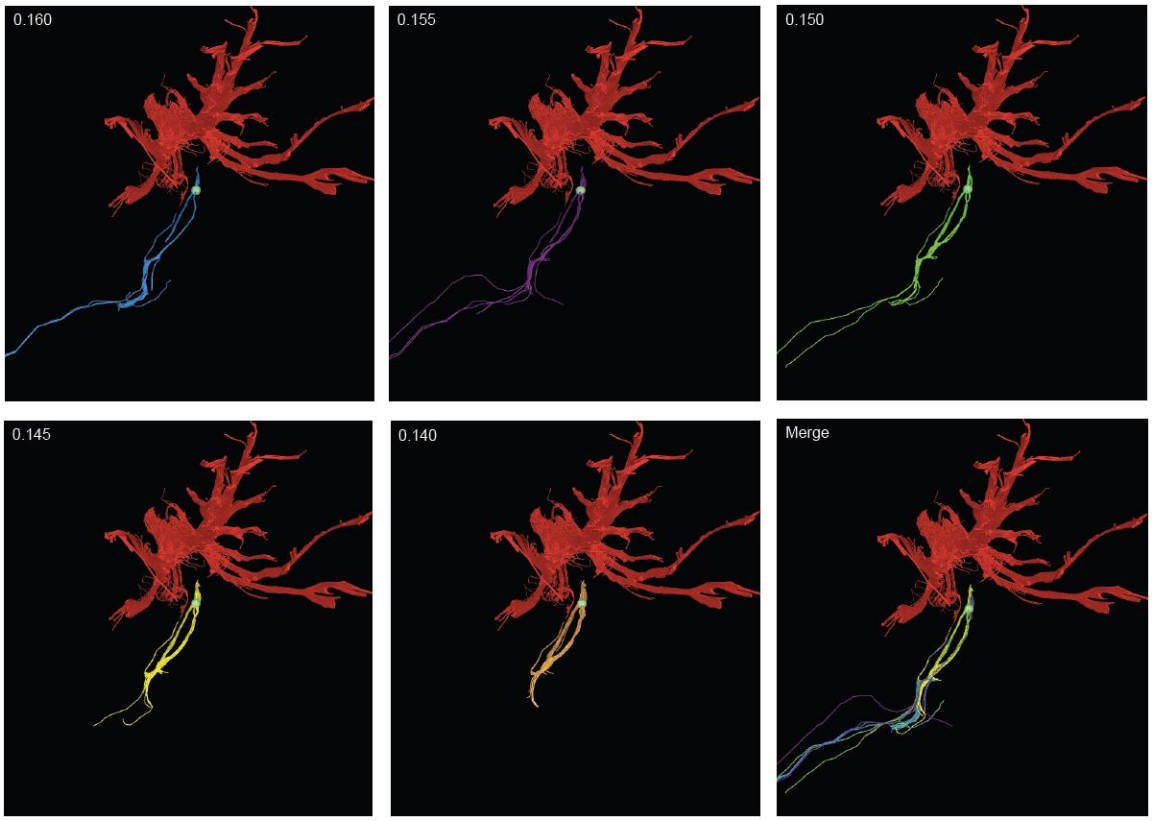

Figure 28: Peripheral nerves running between the spine and abdomen as calculated under different physiologically relevant anisotropic threshold values.The spine is visualized in red, and anisotropic threshold is noted in the top left corner. There is significant variation as seen in the merged panel despite identical seed regions of interest.

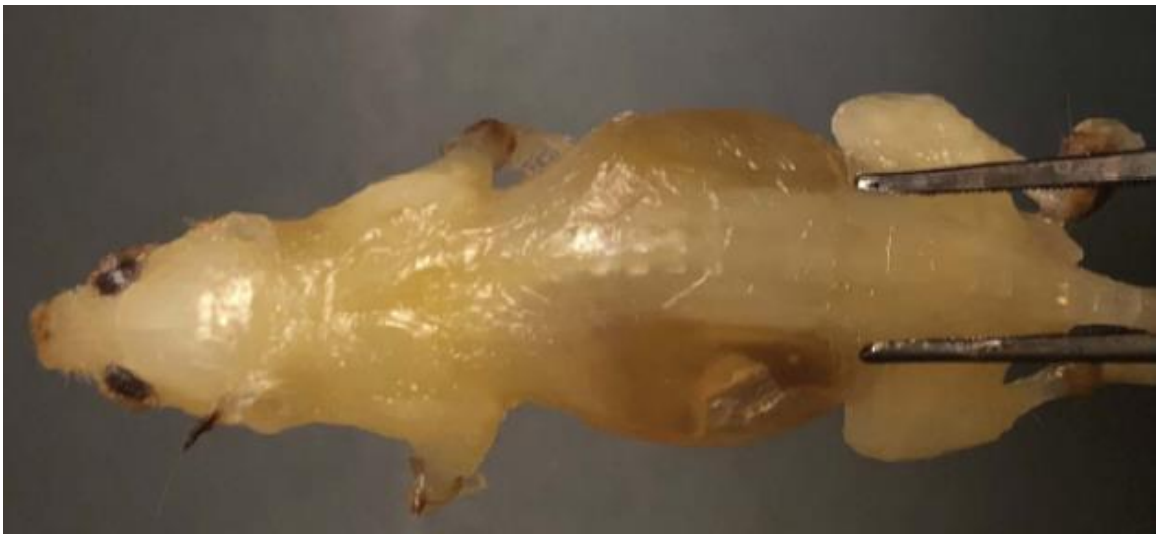

Figure 29: An adult B6 mouse optically cleared using iDISCO+.While some pigment remains, allowing for visualization of the animal against the background, most of the pigmentation has been removed and features such as the vertebrae and abdominal organs are visible through the overlying flesh.

The light sheet imaging of the leg was compared to a DT-MRI reconstruction of the leg imaged in a custom copper solenoid coil under the same conditions as the mouse, except the acquisition matrix was 800 x 400 x 400 over a 32 mm x 16 mm x 16 mm field of view, yielding 40 μm isotropic voxels (Garrett et al., 2021). The sciatic nerve, visible even without tractography in z-projections of the leg MRI, served as a key landmark for orientation and is clearly identified in the tractography of the leg (Figure 31). Analogous regions of the leg were identified in both the light sheet and DT-MRI reconstructions (Figure 32) and compared using a series of parameters as illustrated in Table 1 to determine the parameters which best reflected ground truth. These are recorded at the end of Section 3.1. Despite some characteristic warping associated with clearing protocols, the reconstructions are highly consistent.

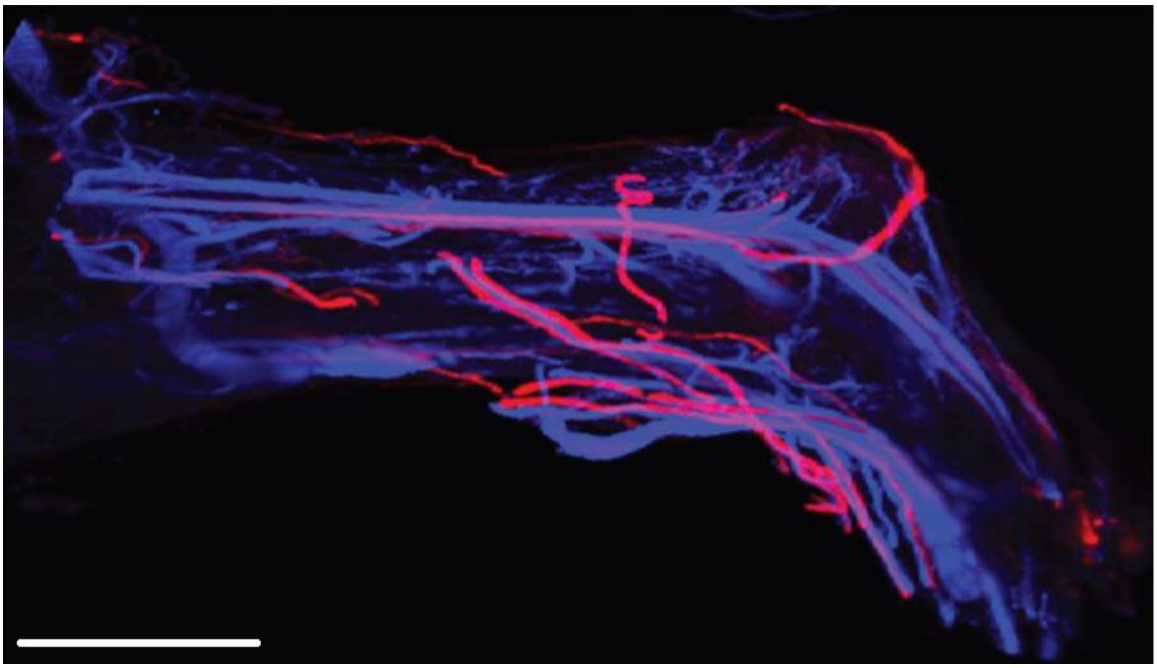

Figure 30: Light sheet microscopy of a mouse leg stained for nerves and vasculature.Nerves (blue) are stained by an antibody against pan-neuronal marker Tuj1. Vasculature (red) is stained by an antibody against smooth muscle actin (SMA). The thigh is located on the top left of the image, with the foot in the lower right. Scale bar 500 µm.

Figure 31: MRI reconstruction of mouse leg with DT-MRI nerve tractography. Top: z-projection of mouse leg MRI, with arrow pointing to sciatic nerve. Scale bar 300 µm. Bottom: Major nerve fibers of the mouse leg as identified by DT-MRI. Scale bar 500 µm. The sciatic nerve is shown in yellow.

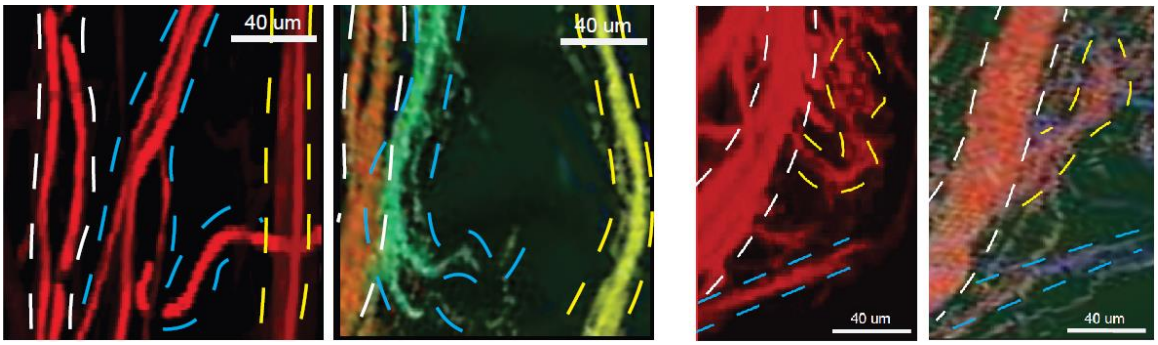

Figure 32: Side by side comparison of leg nerves visualized by light sheet microscopy or DT-MRI.Two illustrative regions from each technique are provided – for each pair light sheet is presented on the left, with DT-MRI on the right. Dashed lines identify landmark nerves seen in both image sets. Light sheet photomicrographs show Tuj1 in red, while DT-MRI photomicrograph colors distinguish unique tracts.

3.3 Differentiating the Vagus Nerve and Tracts Originating at Spinal Foramens

Of crucial importance to identifying pathways with sufficient granularity to be of use to clinicians or researchers looking to perform targeted neuromodulation is identifying nerves originating in the spinal column at the vertebral level they diverge from the spine. To this end each vertebral location on the MRI is noted (Figure 33) and ROIs just outside the foramen are drawn to encapsulate fibers leaving the spine but not those remaining within the bulk of the spinal cord. This enabled visualization of both individual nerve fibers leaving a given vertebral foramen, as well as composite tractography originating from multiple spinal levels (Figure 34). With those tract origins identified, we also have seed ROIs for calculation of innervation for any tissue of interest by nerves originating at those points.

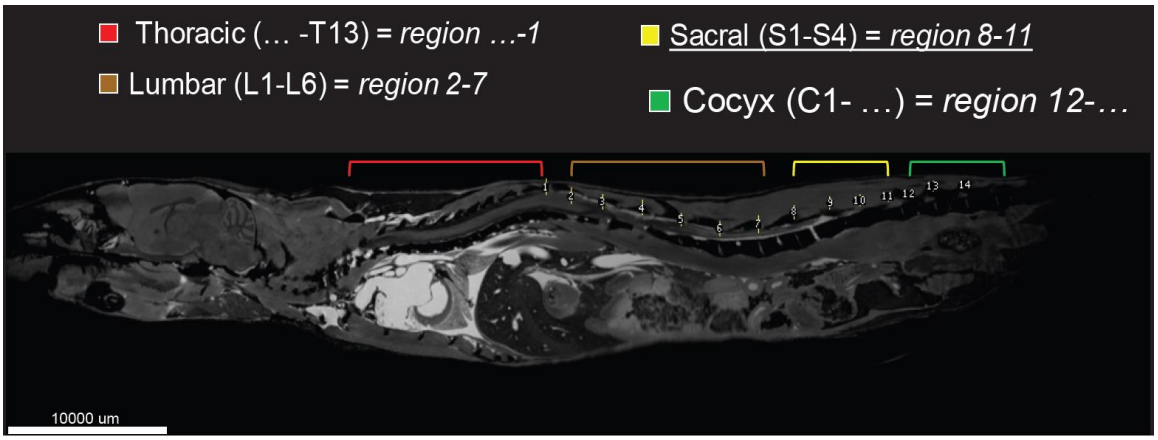

Figure 33: Sagittal cross-section of DT-MRI view of the entire mouse.The thoracic, lumbar, and sacral spine are notated, as is the coccyx. ROIs are drawn around the fibers leaving the spine; these are visible even at low magnification for some reasons, particularly the large fibers of the DRGs, visible here below the lower lumbar and upper sacral vertebral levels.

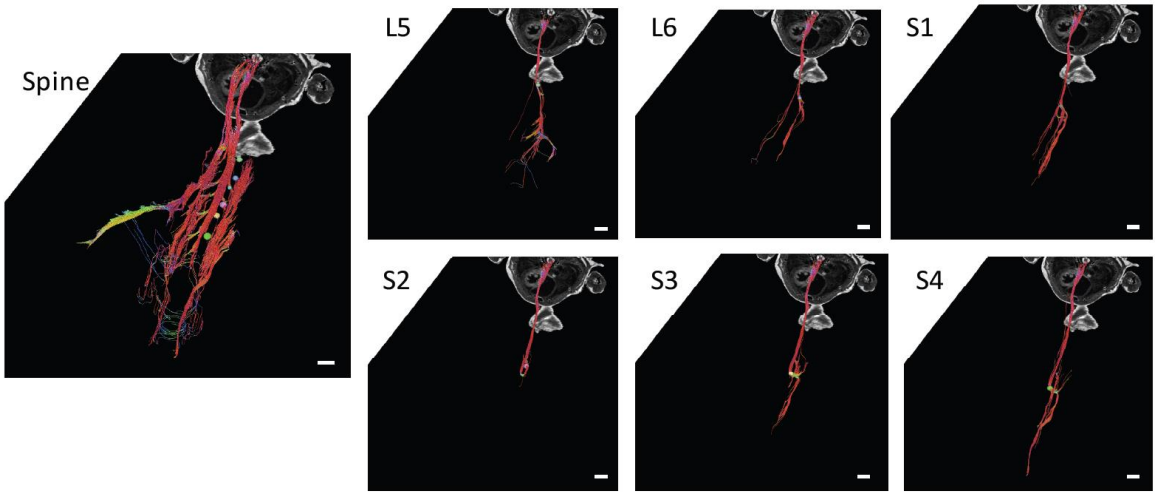

Figure 34: DT-MRI tractography of the lumbar and sacral spine.A cross-section of the mouse at L4 is seen in greyscale at the top of each image for spatial context, with nerves leaving the spine at each vertebral level visualized in the labeled panel. On the left is a composite image of all the DRGs, which overlap and combine to form complex extra-spinal plexuses.

Similar attention is paid to the vagus nerve, which is uniquely pervasive in its innervation of the abdominal and thoracic organs amongst the cranial nerves. The ROI for the vagus nerve was placed in the neck as the cervical vagus nerve is sizeable and

has a predictable location with the esophagus and the carotid arteries as useful landmarks. The tractography of the vagus nerve can be visualized in Figure 35.

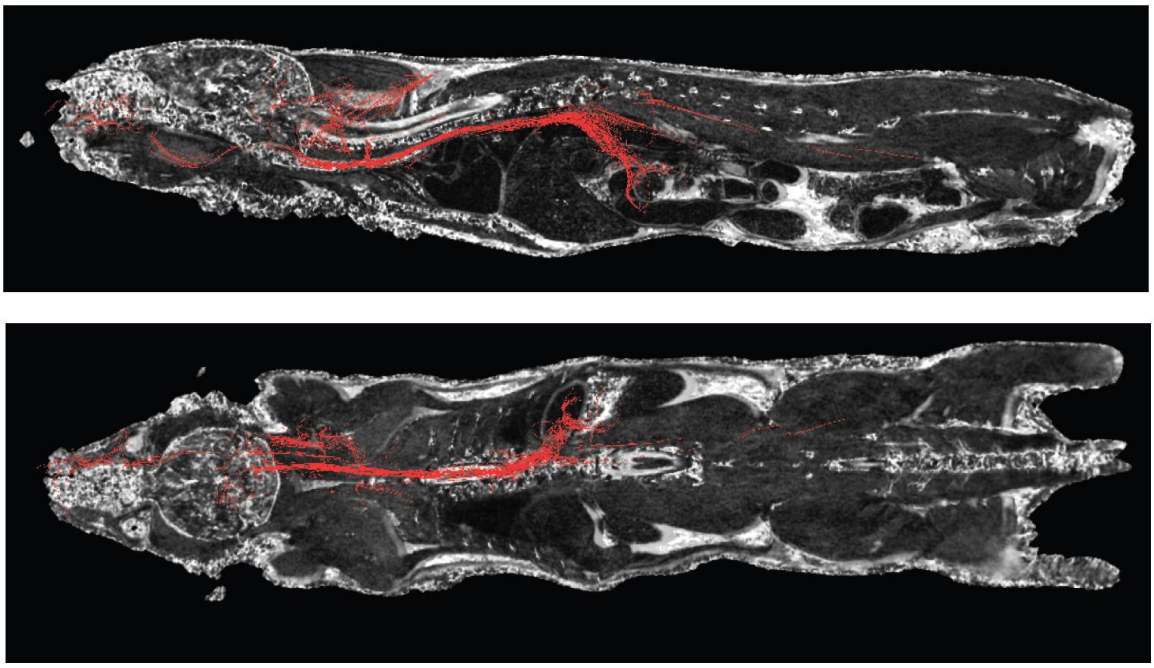

Figure 35: Vagal innervation of the mouse visualized by DT-MRI. Tractography is overlaid with sagittal (top) and transverse (bottom) cross-sections of the mouse for spatial context.

3.4 Innervation of the Heart

The heart is heavily innervated by the vagus (Figure 36), which has known impacts on cardiac function; right vagus nerve stimulation has been noted to cause bradycardia, and VNS is under investigation as a potential therapeutic measure in patients with congestive heart failure (Abraham and Smith, 2013, Hasan, 2013, Hilton et al., 2017, Yoo et al., 2013). Innervation of the heart also arises from the cardiopulmonary plexus, specifically fibers in the sympathetic chain ganglion originating from C3 – T1, with the greatest degree of innervation from C8. The heart itself is heavily innervated, with myelinated neurons previously described along the coronary vessels, mitral valve, and ascending aorta (Hilton et al., 2017).

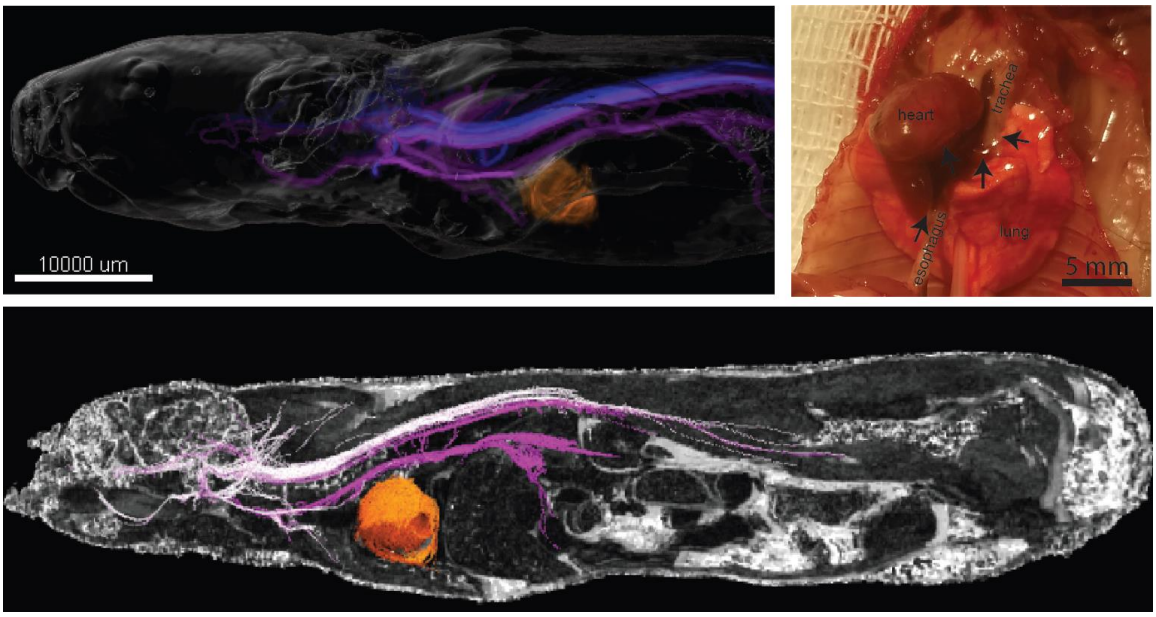

Figure 36: The heart is innervated by thoracic fibers and the vagus nerve.Top left: the heart (orange) is innervated by the vagus (purple) and fibers originating from the cervical and thoracic spine (blue), specifically C3-T1. Top right: gross dissection of the mouse thorax, exposing the trachea, esophagus, heart, and lungs. Large vagal fibers and fibers from the cardiopulmonary plexus are marked with arrows. Bottom: Sagittal cross-section of the mouse MRI overlaid with innervation of the heart (orange) with origins from the vagus (purple) and spine (lilac).

3.5 Innervation of the Lungs

The lungs are innervated by the vagus nerve and the sympathetic chain ganglion (Figure 37) (Chang et al., 2015, Kaelberer and Jordt, 2016). Like the heart, vagal stimulation is known to have an impact on respiratory rate, and is a consideration when setting clinical vagus nerve parameters (Chang et al., 2015, Groves and Brown, 2005, Mwamburi et al., 2017, Yuan and Silberstein, 2016). The DT-MRI based tractography reveals innervation of the lungs via the cardiopulmonary plexus from levels C4 – T3, with the greatest portion of innervation coming from level T3.

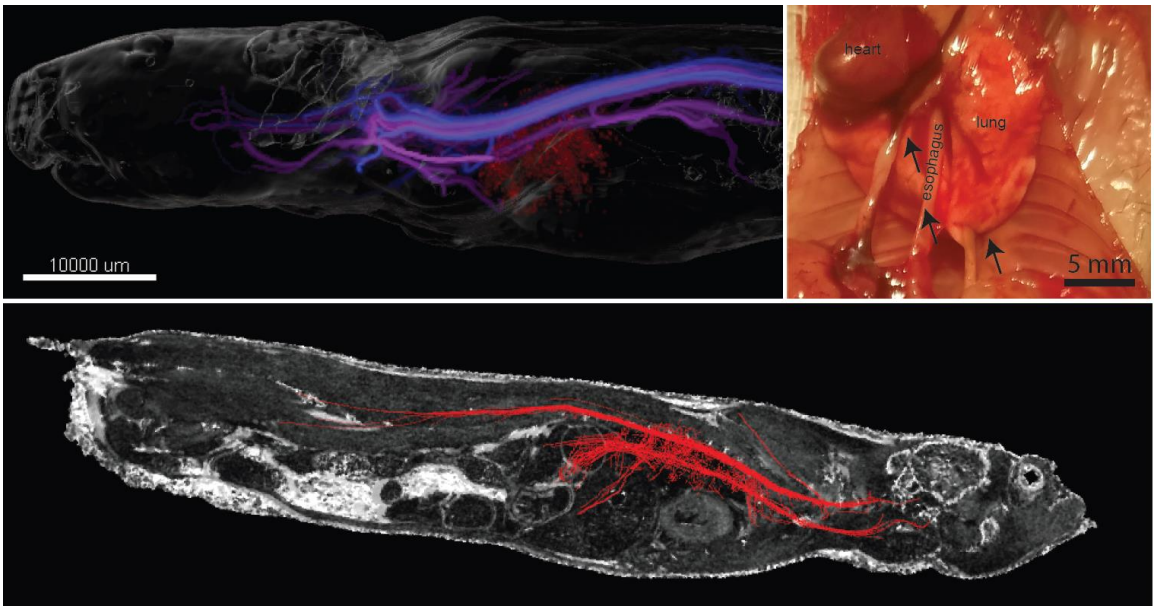

Figure 37: Innervation of the lungs as identified by DT-MRI.Top left: innervation of the lungs (red) originates from the vagus nerve (purple) and the spine (blue), specifically the C4-T3 vertebra. Top right: dissection of the mouse thorax, revealing heart, lungs, and esophagus. Large fibers from vagus nerve and the sympathetic chain ganglion are marked with arrows. Bottom: Sagittal cross-section of the mouse MRI overlaid with fibers which innervate the lungs in red.

3.6 Innervation of the Kidneys

Figure 38 shows the innervation of the kidney as mapped by DT-MRI, which highlights innervation from the least thoracic splanchnic nerve originating from T8-T13, as well as the lumbar splanchnic nerves originating from L1-L4. Of these origins, L1 has the greatest proportionate innervation, although the vagus is the single largest source of innervation for the kidneys, with roughly half of the relative innervation coming from spinal sources and half from the vagus. These findings are consistent with previous reports (Bonaz et al., 2017, Fazan et al., 2002, Sata et al., 2018).

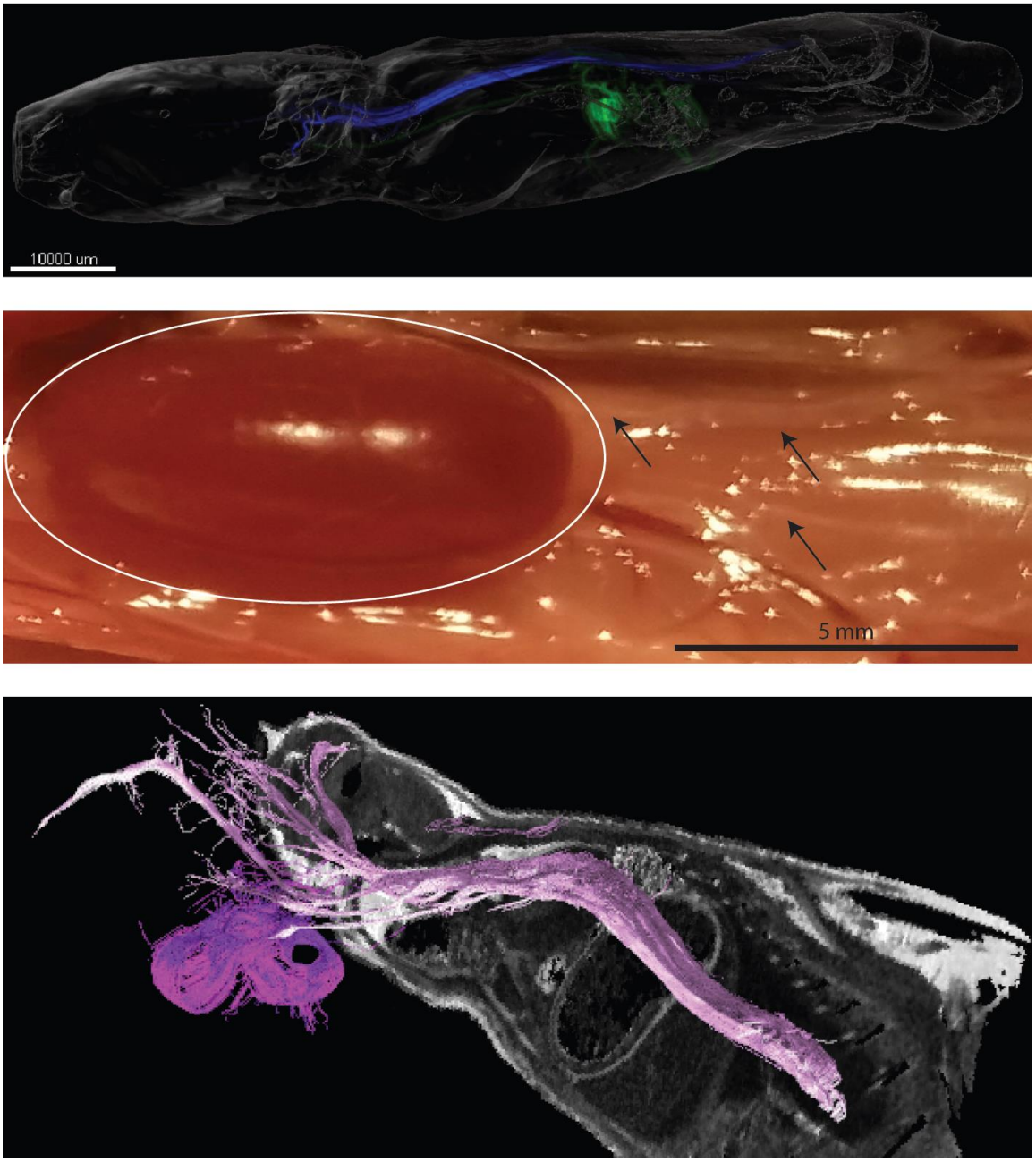

Figure 38: Innervation of the kidney visualized by DT-MRI.Top: Innervation within the kidneys (green) largely originates from the spine (blue). Middle: Photomicrograph of grossly dissected kidney, with large nerve fibers of the least thoracic and lumbar splanchnic nerves marked with arrows. Bottom: Innervation of the kidneys (violet) is largely spinal (mauve), but also includes vagal (lilac) innervation.

3.7 Innervation of the Bladder

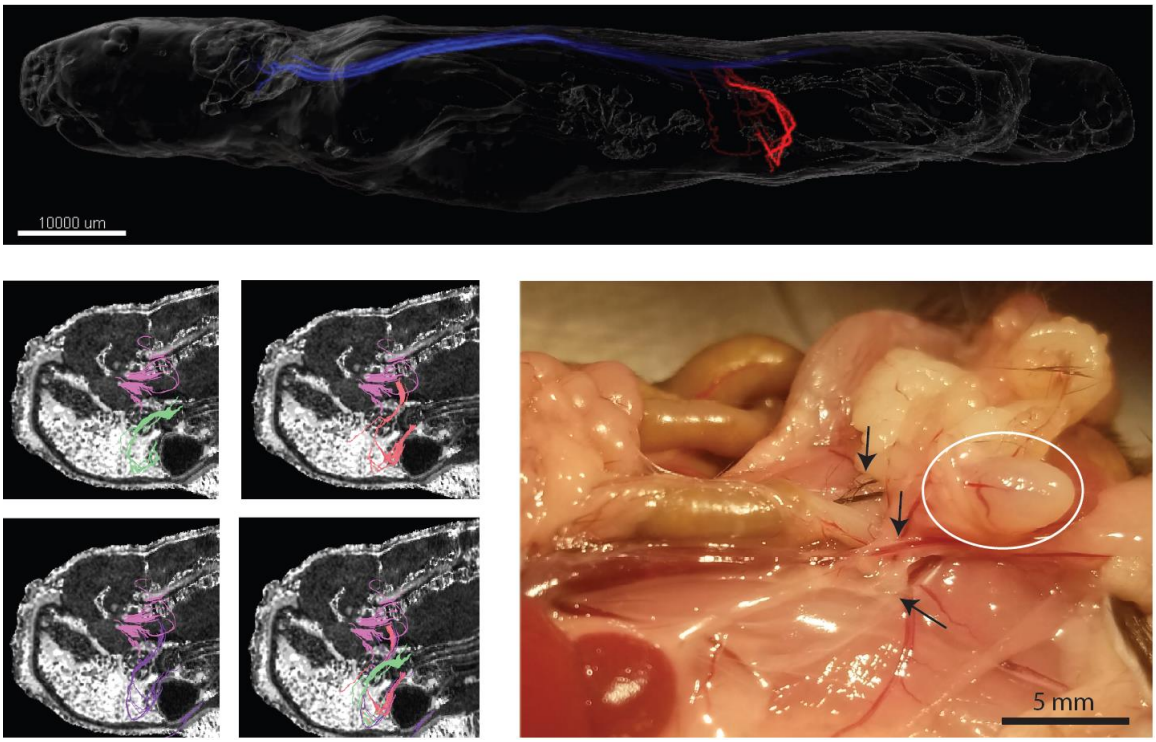

Figure 39: Innervation of the bladder visualized by DT-MRI.Top: bladder innervation (red) originates mostly from the lower spine (blue). Bottom left: three distinct nerve tracts (green, orange, and purple) originate from the spine (pink) and innervate the bladder. Bottom right: Dissection of the mouse pelvic region with a focus on the bladder (white circle). Large fibers of the pelvic parasympathetic nerve and the hypogastric nerves are marked with arrows.

The bladder is innervated predominantly by the hypogastric, lumbar sympathetic, and pelvic parasympathetic nerves (Figure 39). Specifically, pelvic parasympathetic nerves originating from S2-S4, lumbar sympathetic nerves originating from T11-L2, and hypogastric nerves originating from L2-S1 have been reported (Furness, 2012, Herrity et al., 2014, Spencer et al., 2016b), although our tractography finds that the hypogastric nerves have the most significant degree of innervation.

3.8 Innervation of the Liver

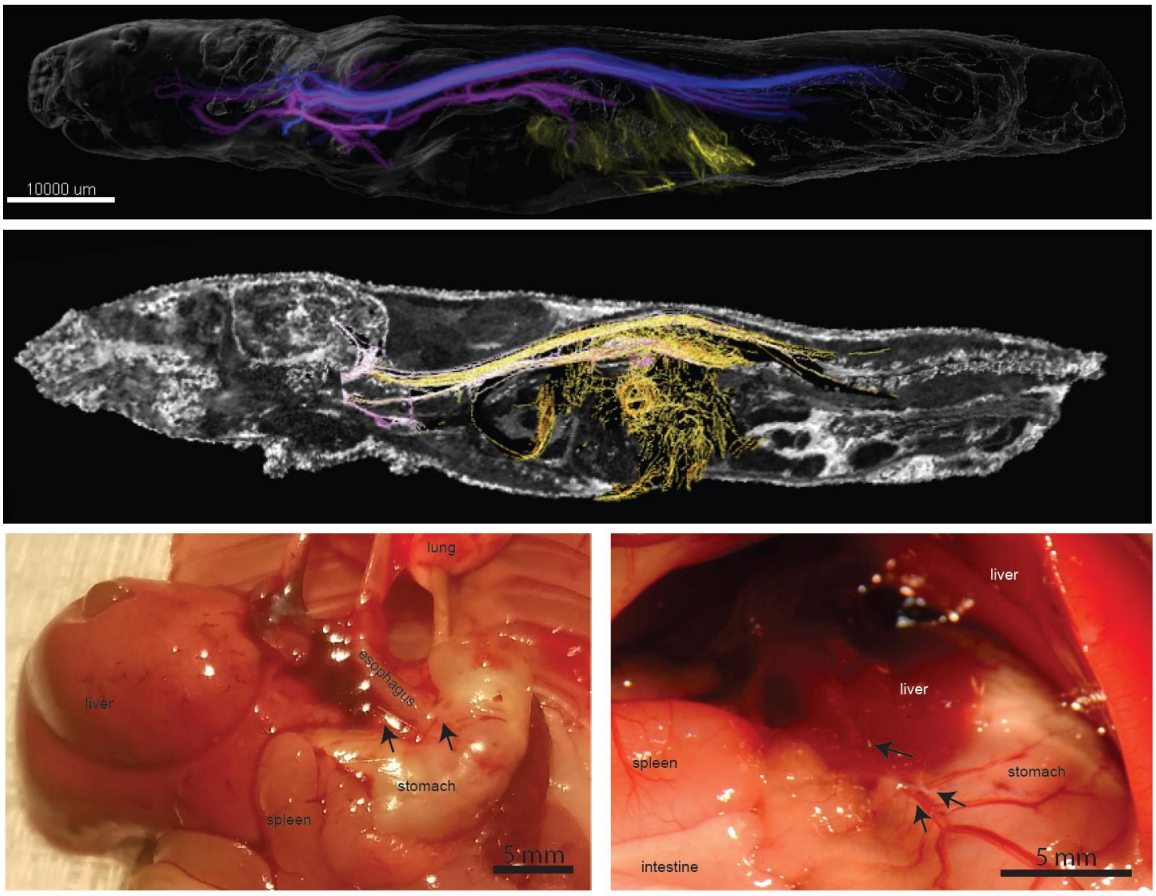

Figure 40: Innervation of the liver visualized by DT-MRI.Top left: DT-MRI tractography showing the innervation of the liver (yellow) by the vagus (purple) and spinal nerves (blue) comprising the greater splanchnic nerves. Middle: liver tractography (yellow) overlaid on a sagittal cross-section of the mouse MRI alongside vagal tracts (lilac). Bottom: Dissection of the mouse abdomen to reveal the liver, with major vagal fibers identified with arrows.

The liver is innervated by the liver and the greater splanchnic nerves (Amir et al., 2020, Matsuhisa et al., 2000, Yahagi, 2017). Spinal liver innervation originates predominantly from the T10, T13, and L1 vertebral foramens (Figure 40). Neuromodulation of liver function, particularly via the vagus nerve, has been proposed previously to address conditions caused by metabolic dysfunction or hyperinflammation (Amir et al., 2020, Malbert et al., 2017, Yahagi, 2017, Guo et al., 1987). This is

particularly appealing for pervasive conditions within the population such as obesity and diabetes, which feature hallmarks such as abnormal glucose metabolism and non-alcoholic fatty liver, both of which have showed promising responses to vagal neuromodulation (Amir et al., 2020, Matsuhisa et al., 2000).

3.9 Innervation of the Esophagus and Stomach

The murine upper GI is heavily innervated by the vagus nerve, but also has notable innervation sources from T3 to L2, predominantly innervation from the greater splanchnic nerves arising from T11 (Figure 41) (Abell et al., 2015, Spencer et al., 2016a). The upper GI, particularly the stomach, has been an appealing target for neurostimulation for many years due to its clear role in digestion, appetite, and satiety (Abell et al., 2015, Browning and Travagli, 2014, Camborová et al., 2003, Paulon et al., 2017, Sung et al., 2014, Browning et al., 2017, de Lartigue, 2016, Göbel et al., 2017, Malbert et al., 2017, Pavlov and Tracey, 2012, Payne et al., 2019, Yao et al., 2018, de Sousa Cavalcante et al., 2020). Gastric neurostimulators and vagal neurostimulators have been studied for a variety of disorders including obesity, gastroparesis, and even Parkinson’s disease. Our tractography supports the vagus nerve as a primary therapeutic target but reveals T11-13 as promising alternatives which may have fewer off-target effects.

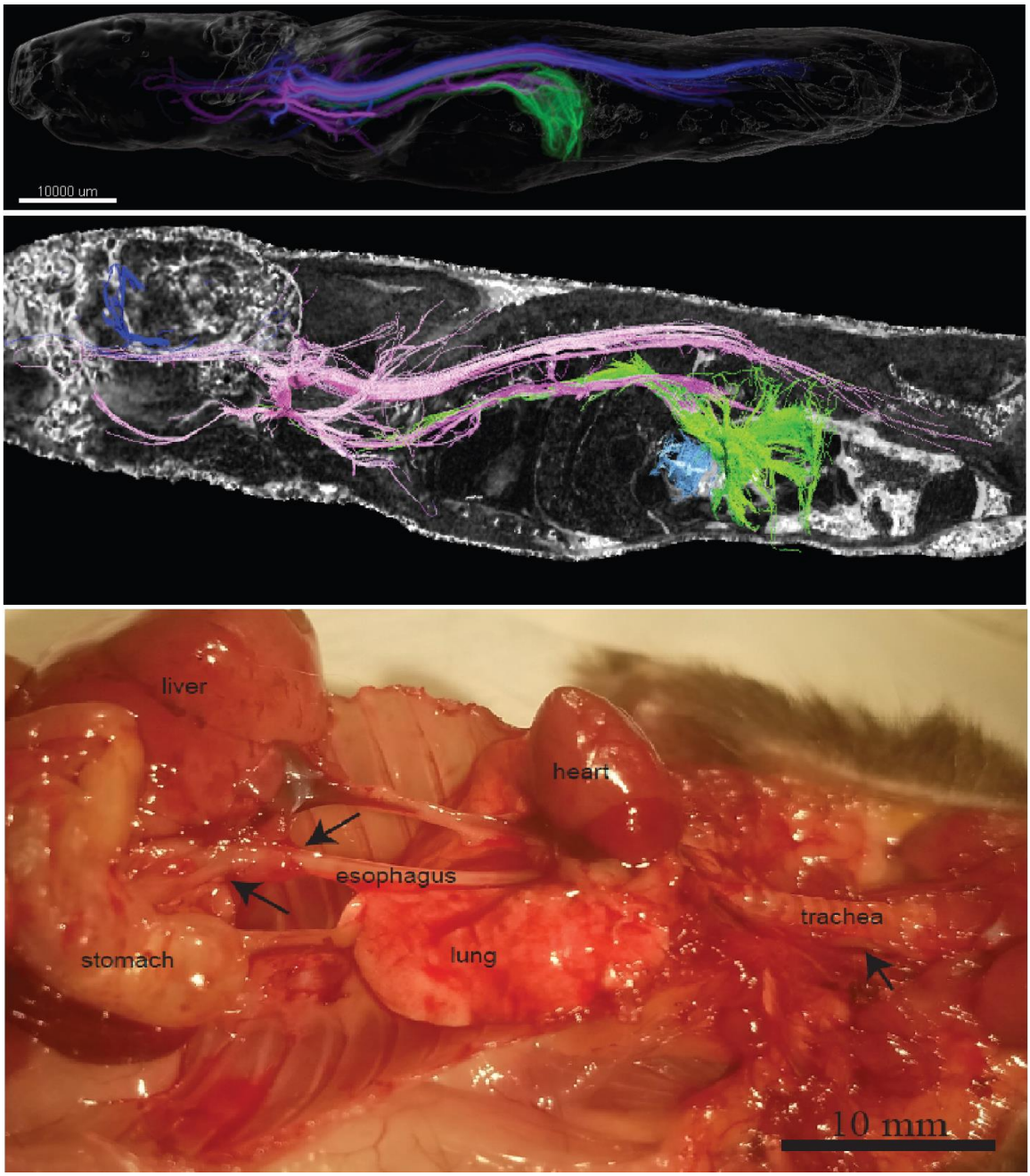

Figure 41: Innervation of the stomach and esophagus visualized by DT-MRI. Top: Innervation of the stomach and esophagus (green) overlaid with vagal fibers (purple) and spinal fibers (blue). Middle: Vagal pathways (purple), spinal pathways (lilac), stomach and esophageal innervation (green) and duodenal innervation (light blue) projected over a sagittal cross-section of the mouse MRI. Bottom: Dissection of the mouse abdominal and thoracic cavities to reveal the

stomach and esophagus. Relatively large vagal fibers are marked with black arrows.

3.10 Innervation of the Small Intestine

The small intestine is heavily innervated by the vagus nerve, which has known involvement in neural circuits regulating satiety, nutrient absorption, microbiome composition, and intestinal motility (Bercik et al., 2011, Bonaz et al., 2017, Browning et al., 2017, Feldman-Goriachnik et al., 2015, Foster et al., 2017, Kaelberer et al., 2018, Kupari et al., 2019, Pavlov and Tracey, 2012, Williams et al., 2016). The greater splanchnic ganglion also innervates the intestines (Browning and Travagli, 2014), with particularly high innervation observed from the L3, L4, and S2 vertebral nodes (Figure 42).

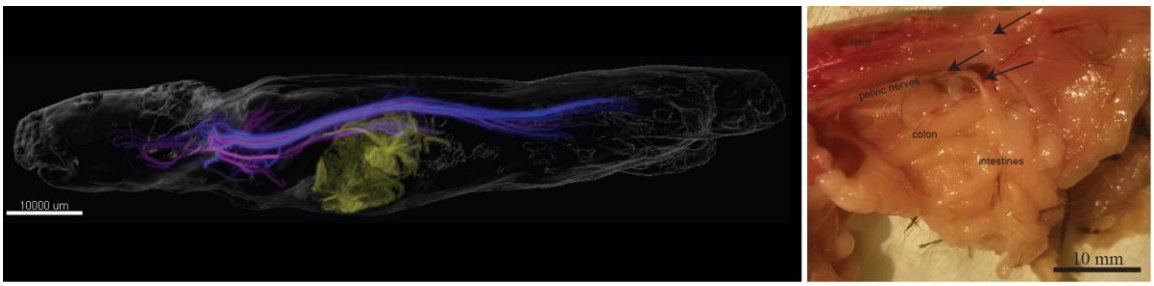

Figure 42: Innervation of the small intestine visualized by DT-MRI.Left: Innervation of the small intestine (yellow) with vagus nerve (purple) and spinal nerves (blue) providing innervation sources. Right: gross dissection of the mouse abdomen to reveal the GI tract. Large nerve fibers innervating the intestines from the greater splanchnic ganglion are marked with arrows.

3.11 Innervation of the Colon and Rectum

Canonically, innervation of the colon and rectum is predominantly through the sacral nerves and lesser splanchnic nerves. (Brierley et al., 2018, Vermeulen et al., 2014, Furness, 2012). These sources arise between T10 and S3 in this study, with higher densities arising from L4 and S1 (Figure 43). We also, however, see a significant

degree of vagal innervation, the degree of which has been previously debated and is frequently understated (Altschuler et al., 1993, Herrity et al., 2014).

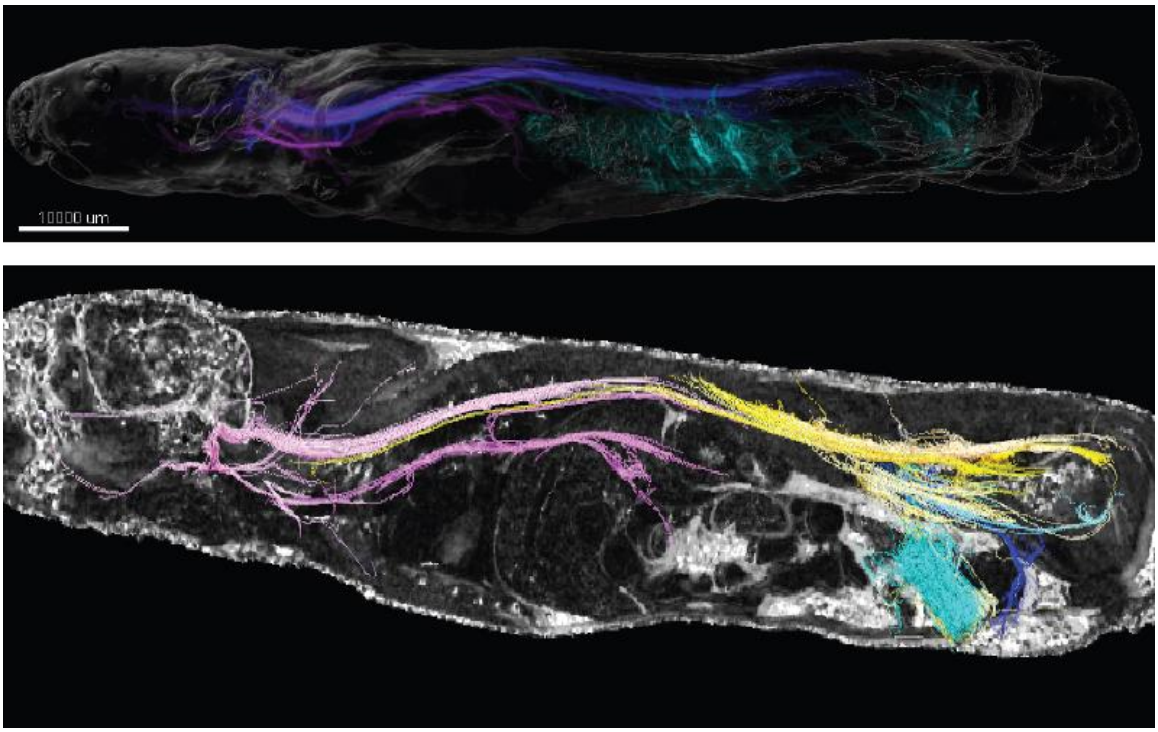

Figure 43: Innervation of the colon and rectum visualized by DT-MRI.Top: Innervation of the colon (cyan) is contributed to by the vagus nerve (purple) and nerves originating from the lower spine (blue). Bottom: The vagus (purple) and DRGs (yellow) both innervate the colon (teal) while the rectum (blue) is exclusively innervated by spinal fibers.

3.12 Quantitative Tractogram of the Murine Peripheral Nervous System

Using the whole mouse tractography generated with no seeded regions of interest, I then overlaid ROIs of the abdominal and thoracic organs and nerve pathways previously described to create a parcellation map of the whole mouse. I then generated a connectivity matrix counting the tracts connecting each organ with each vertebral foramen, as well as the vagus nerve. This was then normalized against the total number of tracts innervating the target organ to create a relative innervation heatmap (Figure

44). While this quantitative tractogram is largely in agreement with the canonical understanding of peripheral innervation, it provides a notable advantage in that for the first time the degree of innervation is noted for particular sources, and innervation sources are identified on a more granular level to easily isolated anatomical landmarks, enabling studies which rely on neuromodulation. Furthermore, because this tractogram explicitly highlights innervation to all organs, this provides a useful tool to determine likely off-target effects a therapy might have.

This quantitation is particularly interesting, however, for the innervation schema for the GI organs. While vagal innervation of the upper GI has long been established, vagal innervation of the distal small intestine and colon has been debated; similarly, while sacral innervation of the colon is readily accepted, there continues to be debate regarding the degree of innervation of the colon and distal small intestine, particularly with regards to nerves originating from the lower sacral foramens. Herein we show conclusively that the small intestine receives innervation from as far as the S2 foramen, and the colon receives significant innervation from the vagus nerve as well as sacral nerves originating as low as S3.

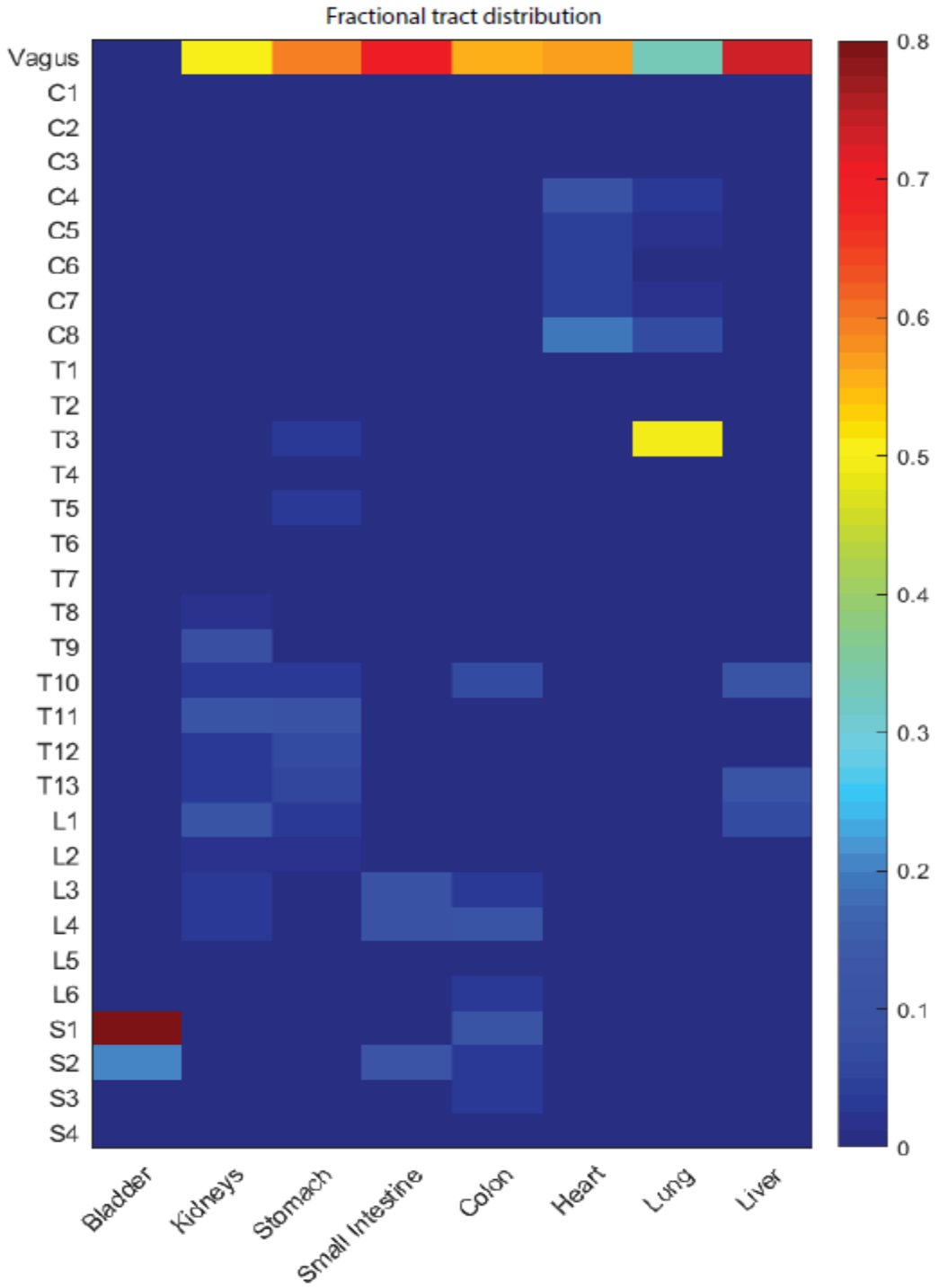

Figure 44: A quantitative tractogram of peripheral innervation of major abdominal and thoracic organs based on deterministic tractography by DT-MRI

4. Vagotomy as a Treatment for Cancer Associated Cachexia

Cancer-associated cachexia (CAC) is a multifactorial syndrome defined by weight loss greater than 5%, weight loss greater than 2% in those with a body mass index (BMI) < 20 kg/m^2, or depletion in skeletal muscle mass (Fearon et al., 2011). In addition to weight loss, CAC-related metabolic dysfunctions include adipose tissue wasting, muscle atrophy, and decreased appetite (Kalantar-Zadeh et al., 2013). The onset of CAC increases chemotherapy toxicity and complications from surgeries, decreases quality of life in patients, and leads to higher mortality rates (da Rocha et al., 2019). Prevalence of CAC is as high as 80% in some cancers, and an estimated 30% of cachexic patients will ultimately die from the syndrome (Dhanapal et al., 2011, Aoyagi et al., 2015, Arthur et al., 2014, Baracos et al., 2018). Ultimately, half of all cancer deaths are directly attributable to CAC.

It is estimated by that 0.5 - 1 % population of all developed world countries suffer from CAC with 1.3 million patients in the US alone (Arthur et al., 2014, Baracos et al., 2018, Dhanapal et al., 2011, von Haehling et al., 2016). CAC cannot be reversed by standard nutritional intervention, and no correlation has been demonstrated between dietary intake and body composition parameters (Dodson et al., 2011, Gullett et al., 2011). Furthermore, pharmacologic interventions, including corticosteroids, anabolic steroids, and anti-inflammatory drugs, have all failed to produce meaningful improvements in clinical settings (Ohnuma, 2003). No treatment for CAC exists, but as of 2019 palliative care for CAC represents a 2.02 billion dollar global market and 800 million dollar US market (Arthur et al., 2014, Marceca et al., 2020, Vaughan et al., 2013, von Haehling et al., 2016).

The vagus plays key roles in pathways related to ingestion, appetite, nutrient sensing, digestion, metabolism, inflammation, and glucose homeostasis, which are disrupted in CAC patients (de Lartigue, 2016, Bonaz et al., 2017, Groves and Brown, 2005, Kaelberer et al., 2018, Matsuhisa et al., 2000, Pavlov and Tracey, 2012). The role of the vagus nerve in multiple hallmark symptoms and mechanisms of CAC makes it an appealing target for a more comprehensive approach to CAC therapy, given the failure of current approaches which are focused on treating singular clinical symptoms. In this section I discuss how disruption of aberant vagal signaling by vagotomy relieves CAC symptoms and ultimately improves model rodent condition and survival.

4.1 Right Vagotomy Attenuates Cachexic Weight Loss in KPC and LLC Injected Mice

To assess the potential benefits of vagotomy in CAC, 6 week old wild type B6/J mice were injected with 5 x 10^6 Lewis lung carcinoma (LLC) cells (ATCC, CRL-1642) intramuscularly into the left flank or 5 x 10^6 $KRAS^+$ pancreatic cancer (KPC) cells (Naqvi et al., 2018) intraperitoneally. Healthy control mice were injected with PBS. Cancer injected mice either received no treatment or therapeutic right cervical vagotomy. Ten days post-injection KPC cohort mice were harvested, and 14 days post-injection LLC cohort mice were harvested.

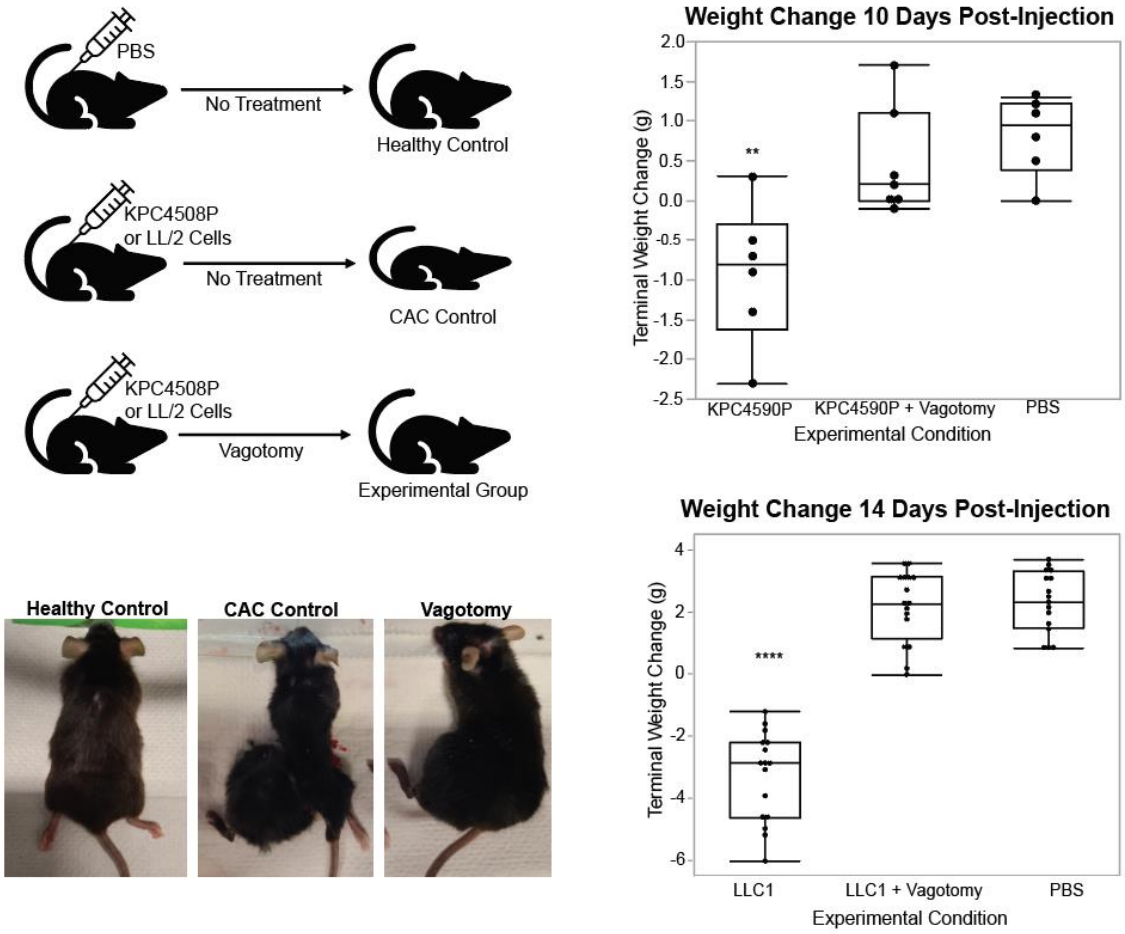

Figure 45: Mice injected with KPC or LLC cells develop cachectic weight loss which is attenuated by vagotomy.Top left: schematic of experimental system; wild type B6 mice are injected with PBS, KPC, or LLC cells. Mice injected with cancer cells either receive no treatment or therapeutic vagotomy. Bottom left: Mice injected with LLC cells develop large flank tumors at the injection site. In untreated mice they experience profound cachectic weight loss, but vagotomized experience no weight loss to accompany their tumor growth. Right: Quantification of weight change in KPC cohort mice (top) and LLC cohort mice (bottom). Untreated cancer mice are statistically significantly different from both vagotomized and control mice, with no significant difference detected between control and vagotomized mice. ** indicates $p < 0.01$, ** indicates $p < 0.0001$ by ANOVA with Tukey post-hoc correction for multiple comparisons.**

In both cohorts a statistically significant reduction in weight was noted for the untreated cancer group compared to controls or vagotomized cancer mice when final

weight was corrected for tumor mass, while vagotomized mice were not statistically different from healthy controls (Figure 45). While I employed a KPC model to ensure the treatment was effective in multiple cancer cell types, all further data in this study uses exclusively LLC data. The KPC model has limitations in that the tumor burden for individual animals cannot be readily assessed. Additionally, as these cells are injected IP they do not form a single easily isolated tumor mass, making correction for added tumor weight challenging. Unfortunately, without correction for tumor weight it is challenging to differentiate between control mice and cachectic mice in the KPC model as the abdominal tumor is lethal far earlier than the LLC flank tumors despite producing less obvious cachectic weight changes.

4.1.1 Right Vagotomy Better Attenuates Cachectic Weight Loss than Left Vagotomy

It is established that the vagus nerve is asymmetrical in its composition and innervation of organs and tissues (Han et al., 2018, Kupari et al., 2019, Yuan and Silberstein, 2016). While clinical interventions focus currently utilized focus on the left cervical vagus, safety and feasibility has been established for targeting the right vagus in several case studies, and vagotomy is generally well tolerated by patients if not preferred due to its permanent nature (Krahl, 2012, Liu et al., 2017). Based on neural circuits for gut-based reward identified exclusively in the right vagus (Han et al., 2018), however, we theorized that right vagotomy would be more effective than left (Figure 46).

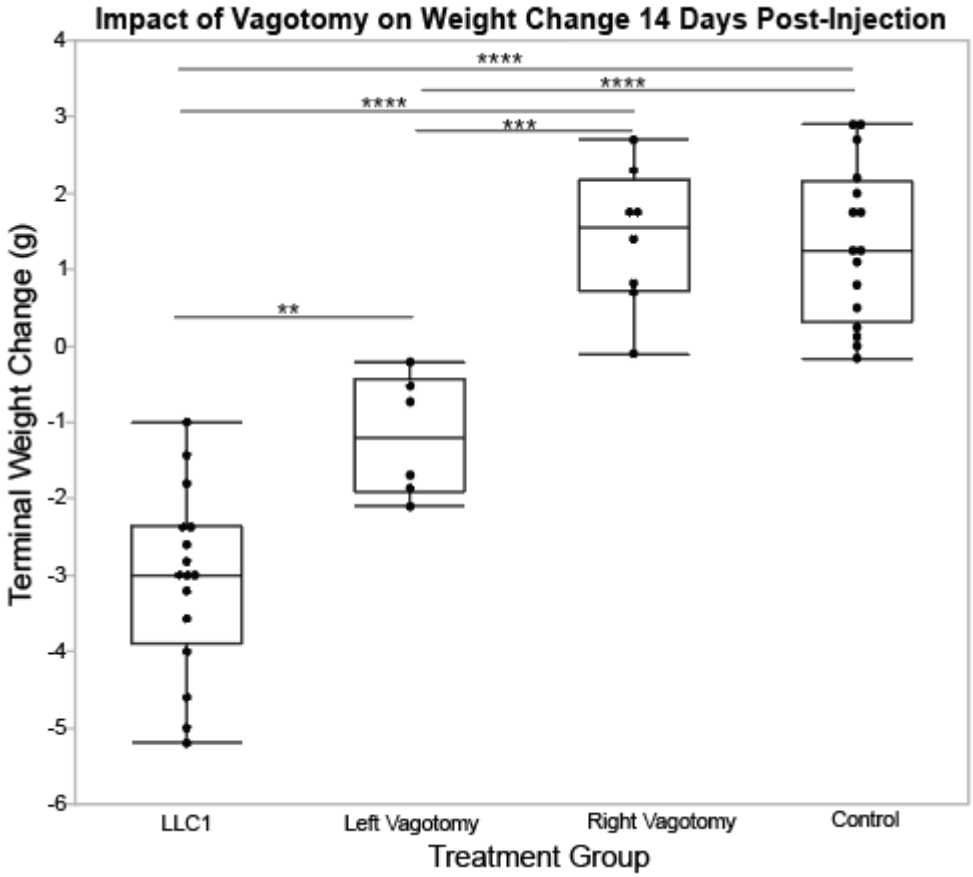

Figure 46: Right vagotomy better attenuates cachectic weight loss than left vagotomy.LLC mice receiving right vagotomy were not statistically significant from healthy controls, but all other groups were statistically significant from both healthy controls and cancer mice with right vagotomy. Mice receiving left vagotomy did see some attenuation of cachectic weight loss, but not as much as those receiving right vagotomy. Statistical significance assessed by ANOVA with Tukey post-hoc correction for multiple comparisons. ** indicates $p < 0.01$, * indicates $p < 0.001$, **** indicates $p < 0.0001$.**

Indeed, right vagotomy results in no significant weight difference when compared to healthy controls, whereas animals receiving left vagotomy or no treatment experienced significant weight loss. Left vagotomy does appear to attenuate weight loss, as this group is statistically different from untreated cancer mice, perhaps due to sparse redundant pathways of therapeutic value being present in the left vagus. Having

demonstrated the greater efficacy of right vagotomy, from this point on animals receiving vagotomy treatment should be understood to be receiving right vagotomy.

4.2 Right Vagotomy Attenuates Cachexic Muscle Atrophy

One of the hallmarks of CAC is skeletal muscle atrophy; caused by aberrant proteolysis, this phenomenon results in reduced quality of life and further metabolic disruptions (Baracos et al., 2018). Clinically, two main metrics are used to quantify muscle atrophy, cross-sectional area of skeletal muscle fibers and electromyogram (EMG). The force a muscle cell is capable of generating is directly proportional to the cross-sectional area of that muscle fiber; as a result, biopsied tissue can determine if muscle atrophy has occurred. In an EMG, the measured electrical activity generated by a muscle contraction evoked by an upstream stimulus is used to quantify muscle recruitment and conduction, both contributing to generation of force.

To assess the cross-sectional area of skeletal muscle for these mice, the right gastrocnemius muscle was collected immediately post-mortem and fresh frozen embedded in OCT (Fisher Scientific, 23-730-571). Frozen tissue blocks were stored at -80 ˚C until cryosectioned with 10 µm thickness slices. Tissues were then stained with Alexa-488 conjugated WGA (ThermoFisher, W11261) diluted 1:1000 in HBSS (ThermoFisher, 14025092) for 30 minutes and imaged on a Leica DM500 fluorescence microscope (Figure 47). Muscle fiber area was quantified in ImageJ (FIJI, NIH) using the muscle morphometry plug-in developed by Anthony Sinadinos using Eclipse IDE (Figure 48).

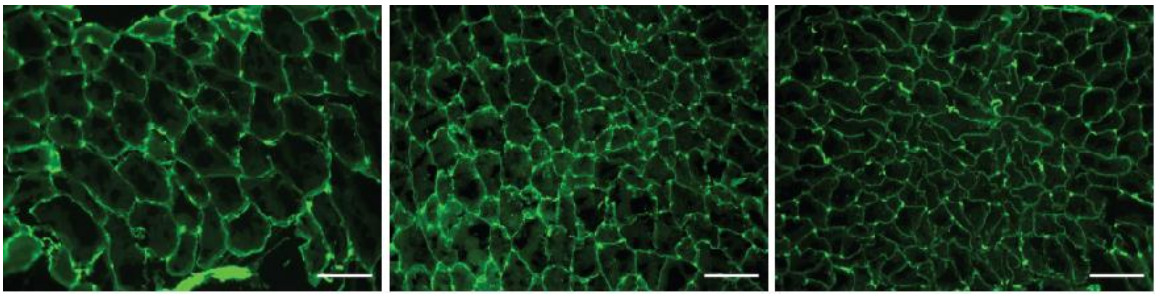

Figure 47: Representative wheat germ agglutinin staining of right gastrocnemius muscle fibers.Harvested from (left to right) control, vagotomized LLC, and untreated LLC mice. Scale bars 100 µm.

Quantification for evoked EMG magnitude can also be seen in Figure 48; just prior to euthanasia, mice were anesthetized with 2% w/v isoflurane and implanted with a microwire hook electrode on the right sciatic nerve. A recording electrode was then embedded in the right gastrocnemius muscle, and a return electrode was embedded subcutaneously over thigh (Figure 49). A 500 µA stimulus was delivered to the sciatic nerve, and the magnitude of the subsequent m-wave generated by the muscle contraction was recorded.

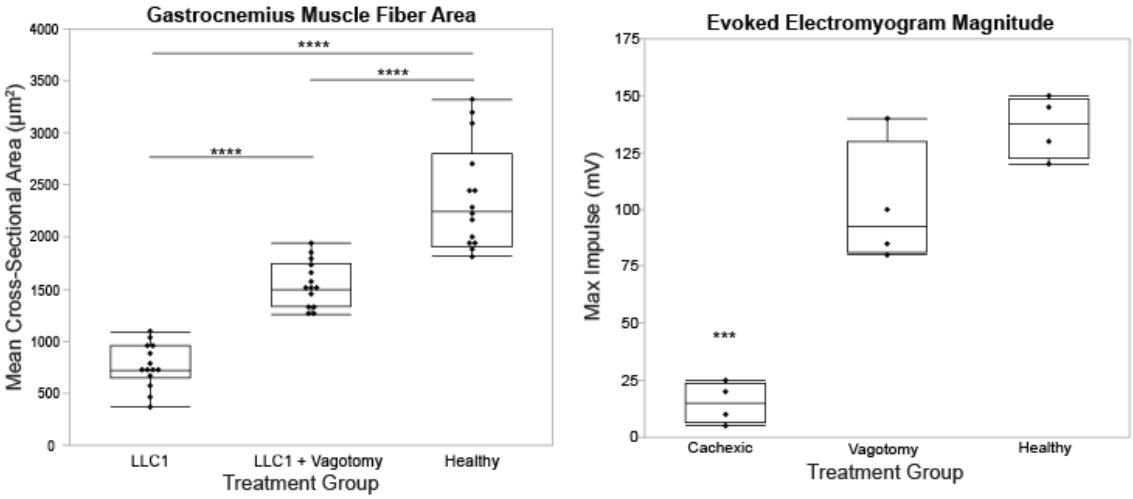

Figure 48: Quantification of mean muscle fiber area and evoked EMG magnitude demonstrates attenuation of muscle atrophy in vagotomized animals. Statistical significance determined by ANOVA with Tukey post-hoc correction for multiple comparisons; * indicates $p < 0.001$, **** indicates $p < 0.0001$.**

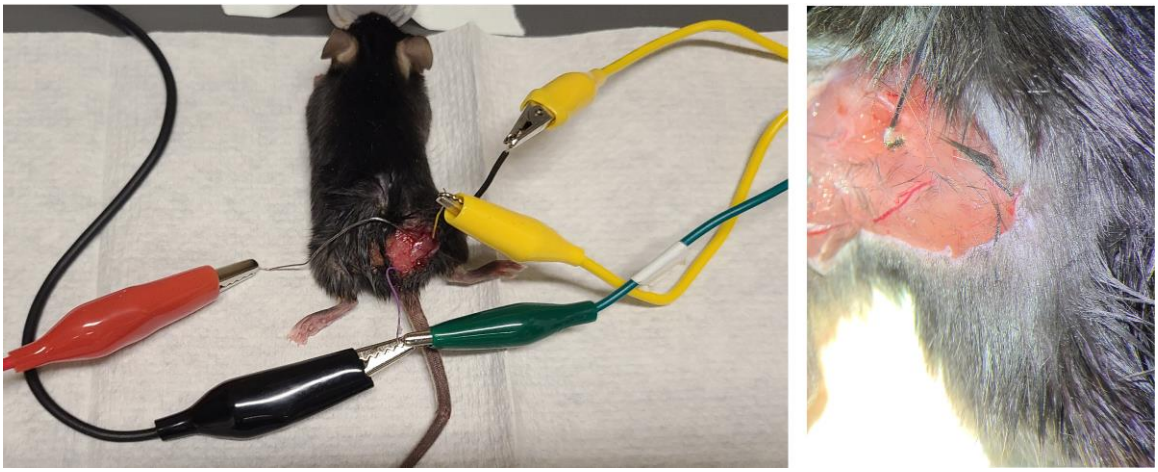

Figure 49: Mouse with sciatic electrode implanted for EMG.Left: full stimulation and recording setup; red wire is the stimulus input, with black return wire which is also the reference wire for recording. Yellow recording wires are connected to the recording electrode in the gastrocnemius and a ground. Right: close-up of exposed sciatic nerve in the microwire cuff stimulation electrode.

Both the mean muscle fiber area and evoked EMG magnitude tests suggest that vagotomy attenuates cachexic muscle atrophy, although there is a statistically significant difference in mean muscle fiber area between vagotomized animals and healthy controls, although it is of lesser magnitude than that between untreated cancer animals and healthy controls.

4.3 Right Vagotomy Attenuates Anorexic Eating Patterns

Another recognized symptom of CAC is anorexia, which likely contributes to cachectic weight loss although clinical studies have shown anorexia alone does not account for cachectic weight loss (Aoyagi et al., 2015, Campos et al., 2017, Dhanapal et al., 2011, Fearon et al., 2011). To assess whether our mice developed anorexic eating behaviors we supplied mice with unrestricted access to food, which was weighed daily. Average daily food intake for the week prior to euthanasia was calculated and compared between treatment groups (Figure 50). Vagotomized LLC mice have no statistically

significant differences in food consumption habits when compared to healthy controls, but untreated LLC mice consume significantly less food than vagotomized LLC mice or healthy controls, indicating that they do experience a lack of appetite and anorexic behaviors akin to those described clinically.

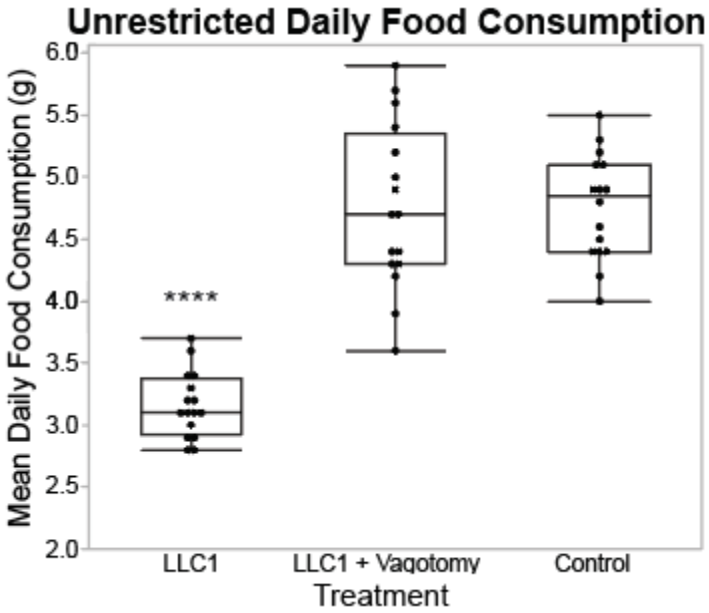

Figure 50: Vagotomy prevents development of anorexic eating behaviors present in untreated CAC mice.Statistical significance determined by ANOVA with Tukey post-hoc correction for multiple comparisons. ** indicates p < 0.0001.**

4.4 Right Vagotomy Normalizes Inflammatory Cytokine Levels

Elevated inflammatory cytokine levels are routinely noted in cancer patients, particularly in patients with CAC (Aoyagi et al., 2015, Baracos et al., 2018, Durham et al., 2009, Marceca et al., 2020, Petruzzelli and Wagner, 2016, Vaughan et al., 2013, Wyart et al., 2020). However, presence of inflammatory cytokines alone is not predictive of whether patients will develop CAC and neutralizing cytokine levels with antibodies has not proved clinically meaningful as a CAC therapeutic (Aoyagi et al., 2015, Marceca et al., 2020, Vaughan et al., 2013). Still, multiple established pathways exist for

inflammatory cytokines to drive abnormal metabolism, specifically proteolysis and lipolysis, which contribute to weight loss and muscle atrophy (Aoyagi et al., 2015, Durham et al., 2009, Petruzzelli and Wagner, 2016, Vaughan et al., 2013, Wyart et al., 2020).

To measure systemic circulating cytokine levels, blood was collected from mice via terminal cardiac puncture and centrifuged at 1000x g for 2 minutes. Serum was then transferred to a clean lo-bind Eppendorf tube. An MSD V-Plex Mouse Cytokine 19-Plex Kit (MSD, K15-2255D) was used to quantify serum levels of 19 cytokines – IFNγ, IL-1β, IL-2, IL-4, IL-5, IL-6, IL-9, IL-10, IL-12p70, IL-15, IL-17A/F, IL-27p28/IL-30, IL-33, IP-10, KC/GRO, MCP-1, MIP1α, MIP-2, and TNF-α. Statistically significant differences were identified in untreated cancer mice relative to vagotomized and healthy control animals, but no significant difference was identified between healthy controls and vagotomized animals for IFN-γ, TNFα, IL-1β, IL-2, and MIP-2 (Figure 51). MCP-1 and MIP-1a levels were significantly different between untreated cancer animals and healthy control animals, but no significant difference was identified between vagotomized animals and either group, suggesting incomplete attenuation of elevated levels of those cytokines (Figure 52). No significant differences were detected between any treatment groups for IL-4, IL-5, Il-6, IL-10, Il-27p28/IL-30, IL-33, or KC/GRO. Serum levels of IL-9, IL-12, IL-15, and IL-17 were below the detection threshold for most animals, precluding analysis.

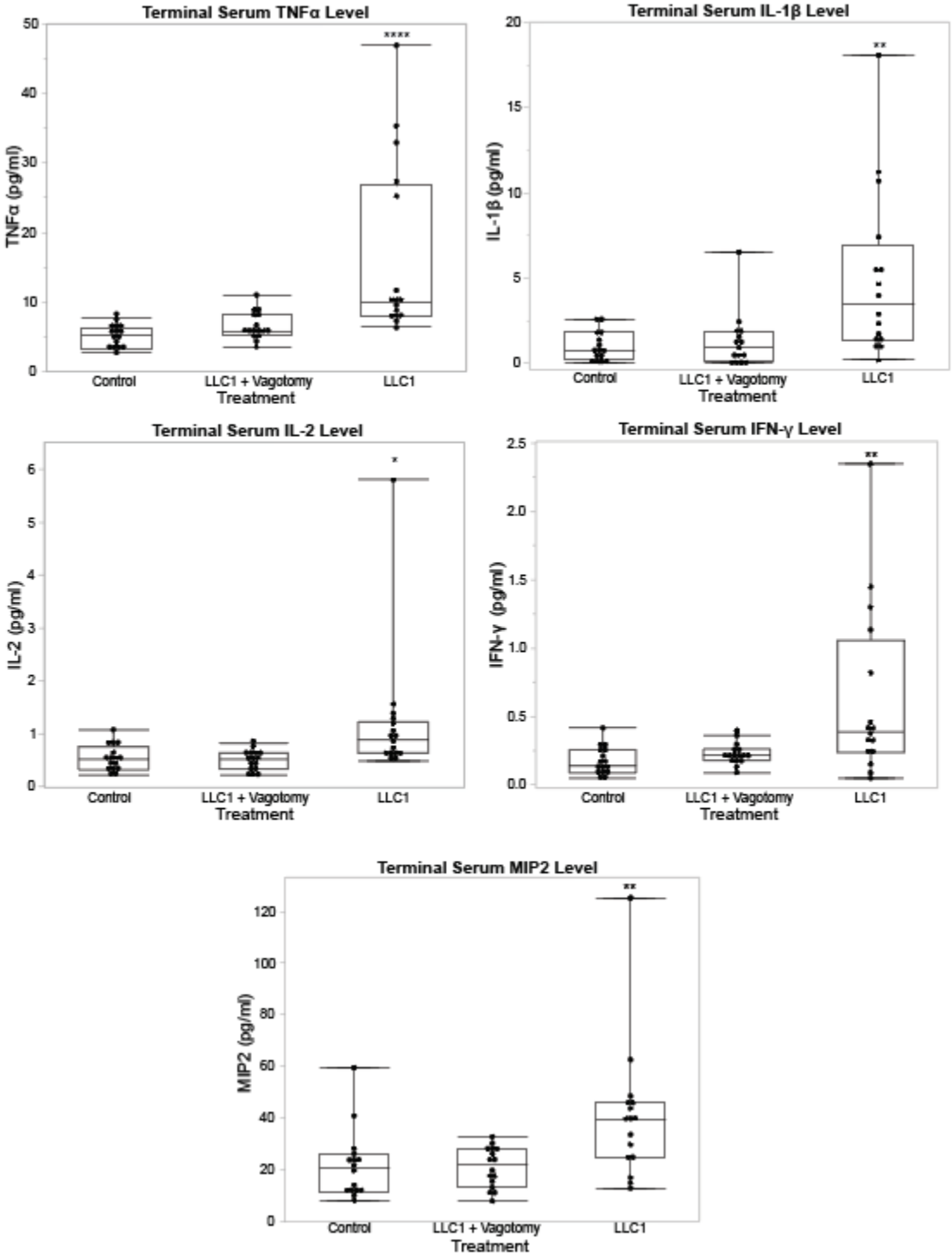

Figure 51: Elevated inflammatory cytokine levels in untreated LLC mice are not observed in vagotomized LLC mice.Serum levels of TNFα, IL-1β, IL-2, IFN-γ, and MIP-2 are elevated in untreated cancer mice compared to both healthy

controls and vagotomized animals, but there is no significant difference between vagotomized animals and healthy controls. Statistical significance determined by ANOVA with Tukey post-hoc correction for multiple comparisons. * indicates p < 0.05, ** indicates p < 0.01, ** indicates p < 0.0001.**

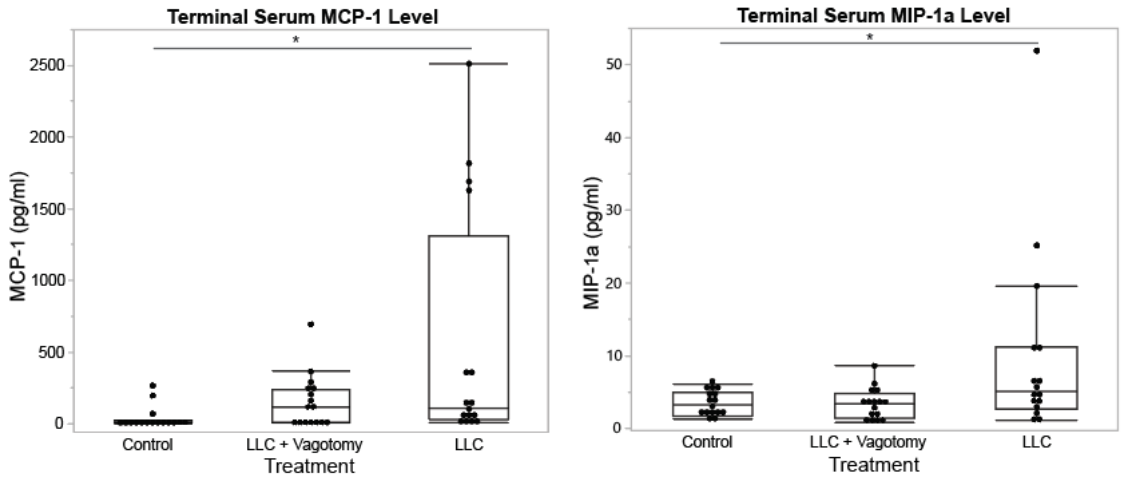

Figure 52: Vagotomy partially attenuates MCP-1 and MIP-1a elevation in tumor bearing mice.Statistical significance is observed between healthy control and untreated cancer animals, but vagotomized animals are not significantly different from either condition. Statistical significance evaluated by ANOVA with Tukey post-hoc correction for multiple comparisons. * indicates p < 0.05.

4.5 Right Vagotomy Increases Survival Duration in Cancer Bearing Mice

Perhaps the most important metric for any therapeutic delivered for a terminal condition is whether it extends survival. To assess whether vagotomy provided any survival benefits to the tumor-bearing animals, we recorded the number of days it took untreated LLC animals and vagotomized LLC animals to die or reach humane endpoints. Vagotomized animals did see a statistically significant extension of life compared to untreated controls (Figure 53), which may have been greater than shown here if vagotomized animals were treated further to reduce the tumor mass. Some of deaths in the vagotomized cohort after day 21 were due not to cachectic symptoms but rather

because their flank tumors were so large that they were impeding normal mobility and/or had ulcerated such that animals needed to be euthanized for humane endpoints.

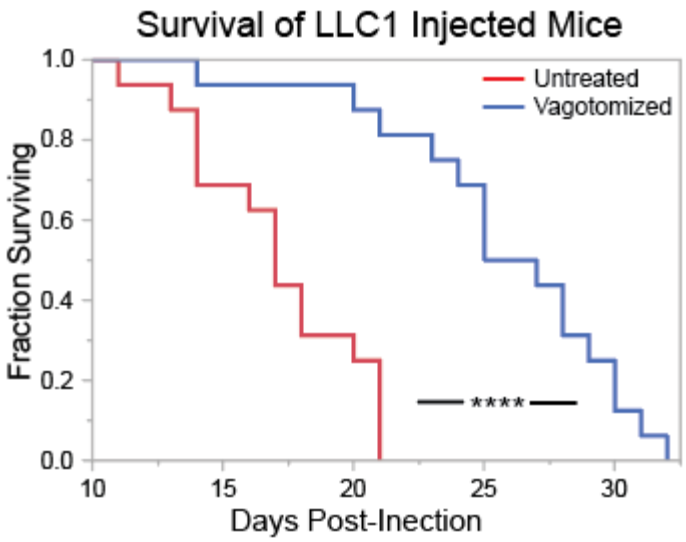

Figure 53: Vagotomized mice had extended survival compared to untreated LLC mice. Survival analyzed with the Kaplan-Meier method and compared with the log-rank test; ** indicates p < 0.0001.**

5. Electrical Vagal Perturbation as a Treatment for Cancer Associated Cachexia

While vagotomy is historically well tolerated clinically, it is not an ideal solution due to the irreversible nature of the surgery. VNS provides a more attractive alternative to vagotomy for clinical application; it's an FDA approved therapy with a clear path to adoption as it is currently used, and the reversible nature of vagal block induced by an electric field makes it preferable to vagotomy or other permanent vagal disruptions (Groves and Brown, 2005, Johnson and Wilson, 2018, Krahl, 2012). This is particularly true with the emergence of transcutaneous VNS devices; without the need for surgical implantation of a stimulator and electrodes, cost and risk to implement VNS are both reduced (Butt et al., 2020, Mkaya Mwamburi et al., 2017, Mwamburi et al., 2020). One such device on the market is specifically approved for their transcutaneous vagal block therapy which is used for relief of cluster headaches, migraines, and hemicrania (Mkaya Mwamburi et al., 2017, Tajti et al., 2019).

5.1 Vagal Low Frequency Alternating Current Block

Vagal blockade has been under research as a possible clinical tool for several years, with the dominant approach to achieving vagal block the use of kilohertz frequency alternating current to produce vagal block (KHFACb) (Patel et al., 2017, Pelot and Grill, 2020). KHFACb is appealing compared to the leading previous approach, DC block, as the low amplitude currents necessary to produce block do not exceed the Water window resulting in hydrolysis, tissue damage, and electrode corrosion (Conde, 2021, Pelot and Grill, 2020). However, KHFACb has a major drawback - the onset response. KHFACb initially produces activation of the nerve fibers before the block is initiated, which when applied to the vagus can induce dangerous bradycardia and

reduction in respiration (Foldes et al., 2009). Additionally, KHFACb has high energy demands relative to implanted VNS devices, making power supply and hardware design for such techniques unfeasible in most clinical settings (Conde, 2021).

Recently, a new method of vagal block has been described by delivering sinusoidal pulses at <10 Hz with pulse widths 100 – 1000 μs and 0.2 to 1.2 mA (Muzquiz et al., 2021). This low frequency alternating current block (LFACb) has been demonstrated successfully in earthworms, dogs, and pigs (Horn et al., 2019, Mintch et al., 2019, Muzquiz et al., 2021). LFACb has lower power demands than KHFACb and does not produce a demonstrable onset response but does produce safe and reversible vagal block (Conde, 2021, Mintch et al., 2019, Muzquiz et al., 2021).

To produce vagal block in this study LFACb was delivered by a current controlled wireless stimulator chip programmed through StimWare (Triangle BioSystems); current pulses were delivered at 5 Hz with 200 ms pulse widths and 0.2 – 0.8 mA pulse amplitudes, consistent with the parameter range described in (Muzquiz et al., 2021). Implantation of the microwire hook electrodes was performed with animals under isoflurane anesthesia (2% w/v). The neck was shaved, and the incision site was cleaned with alternating swabs of iodine and ethanol. Mice were injected with bupivacaine (0.25% <2 mg/kg) and meloxicam (2 mg/kg) subcutaneously prior to surgery and again 24 hours after surgery. A midline incision was made over the trachea. Thyroid glands were gently pushed to either side of the field and connective tissue above the trachea was blunt dissected. The right cervical vagus nerve was visualized between the esophagus and carotid artery. The vagus nerve was dissected away from adjacent tissues and the microwire hook was drawn under the nerve. Custom microwire hook electrodes were fabricated from 40-gauge stainless steel hookup wire with (Cooner Wire

Company, AS814). The hook was gently pinched shut with forceps and anchored with sutures and/or Loctite 406 to adjacent muscle (Figure 54). A ground electrode was placed into the pectoral muscles. Both electrode leads were tunneled subcutaneously to the back of the neck, where they would be accessible for the study but the mice would not be tempted to injure themselves by dislodging the wires. The incision was sutured closed and mice were allowed 48 hours of recovery prior to intramuscular flank injection of the LLC cells as described in Section 4.1. Implanted animals were assigned to either receive LFACb or no stimulation (a sham control). Animals were given another 24 hours before LFACb was administered for the first time; LFACb was administered for 30 minutes daily at the start of the wake cycle.

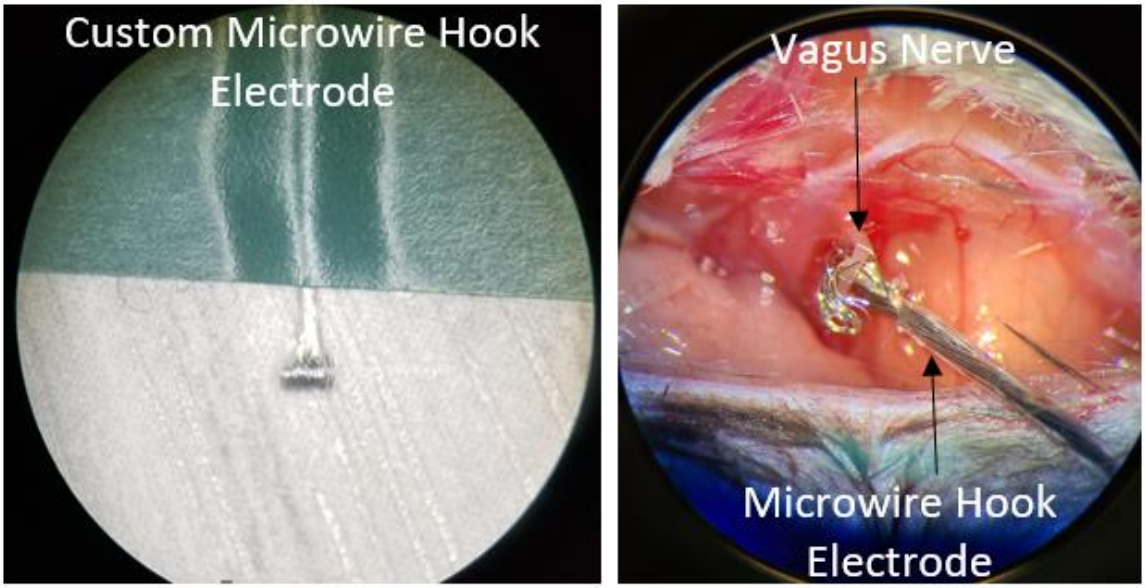

Figure 54: A custom microwire hook electrode was used to deliver LFACb to the cervical vagus nerve.Left: newly fabricated microwire hook electrode. The microwire is 0.11 mm in diameter. Right: microwire hook electrode implanted around the right cervical vagus nerve of a mouse. The murine cervical vagus nerve is approximately 100 µm in diameter.

5.2 Vagal Block Attenuates Cachexic Weight Loss

As outlined in Section 4.1, LLC mice were euthanized and weighed 14 days post-injection. Excised tumor weight was subtracted to determine the adjusted terminal weight (Figure 55). All conditions were signficantly different from the healthy control group as well as the LFACb group. However, the untreated cancer group and sham group were not significantly different. This indicates LFACb attenuates, but does not eliminate, cachectic weight loss. Notably, the inter-animal variability of the LFACb cohort is greater than that of the vagotomy cohort, potentially indicating incomplete block or variable response due to variations in lead placement or impedance.

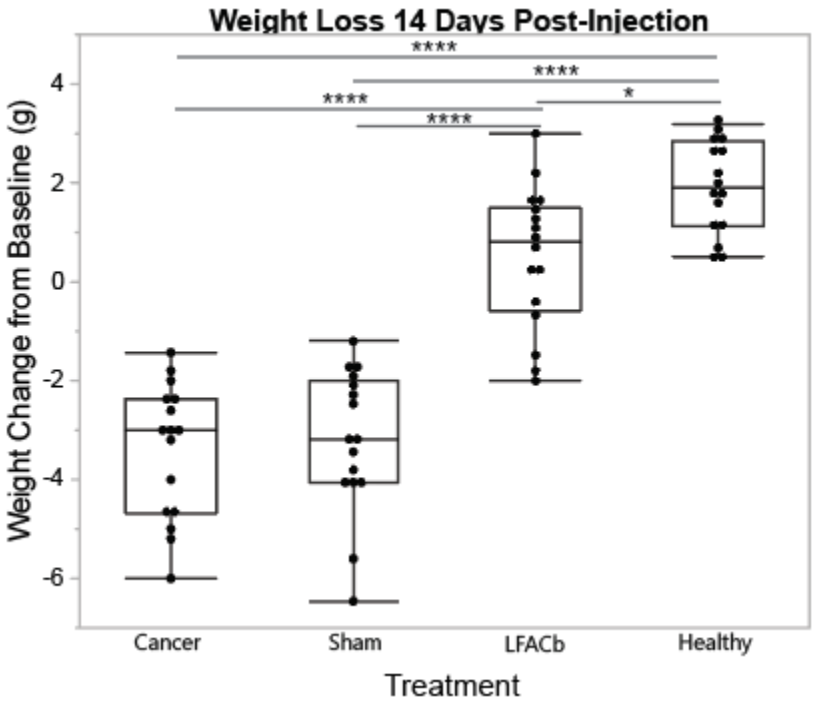

Figure 55: LFACb attenuates, but does not eliminate, weight loss in tumor-bearing animals.Statistical significance determined by ANOVA with Tukey post-hoc correction for multiple comparisons. * indicates p < 0.05, ** indicates p < 0.0001.**

5.3 Vagal Block Attenuates Cachexic Muscle Atrophy

As described in Section 4.2, EMG was performed on mice prior to euthanasia, and the right gastrocnemius was embedded in OCT to be cryosectioned and stained with WGA-Alexa488. Statistical analysis of the quantification of mean fiber diameter in the right gastrocnemius revealed all groups except untreated cancer and sham animals were statistically significantly different, with LFACb animals experiencing a lower magnitude of atrophy compared to untreated or sham animals (Figure 56). Analysis of peak-to-trough measurements of the m-wave following sacral stimulation indicates that with the exception of cancer and sham, all groups are significantly different from one another. The magnitude of decrease in EMG impulse is reduced in LFACb compared to sham and untreated cancer cohorts, indicating in combination with the fiber size analysis that LFACb attenuates but does not eliminate cachectic muscle atrophy.

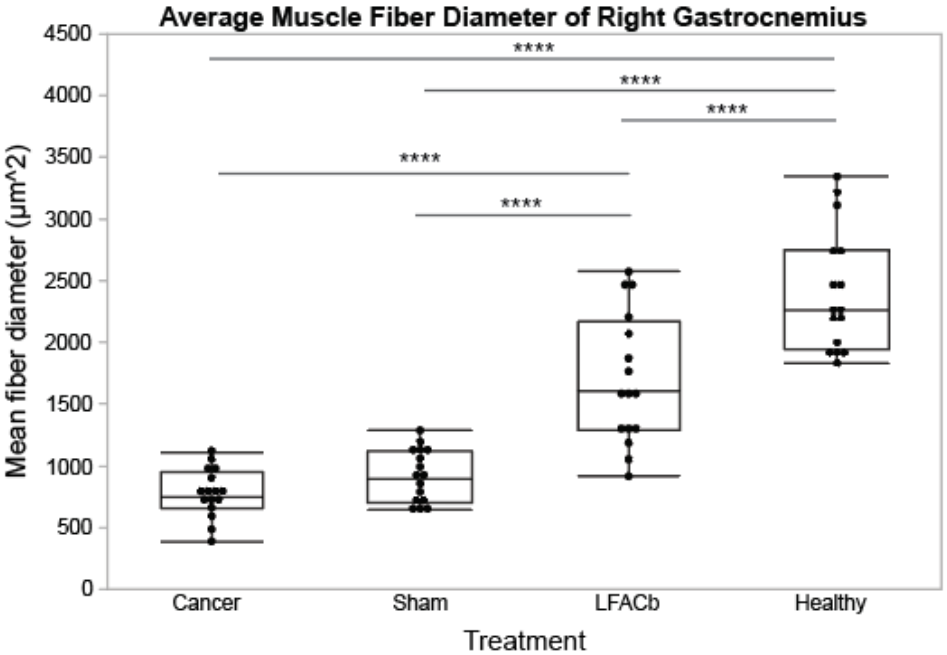

Figure 56: LFACb reduces, but does not eliminate, muscle fiber cross-sectional area decreases indicative of atrophy. Statistical significance determined

by ANOVA with Tukey post-hoc correction for multiple comparisons. ** indicates p < 0.0001.**

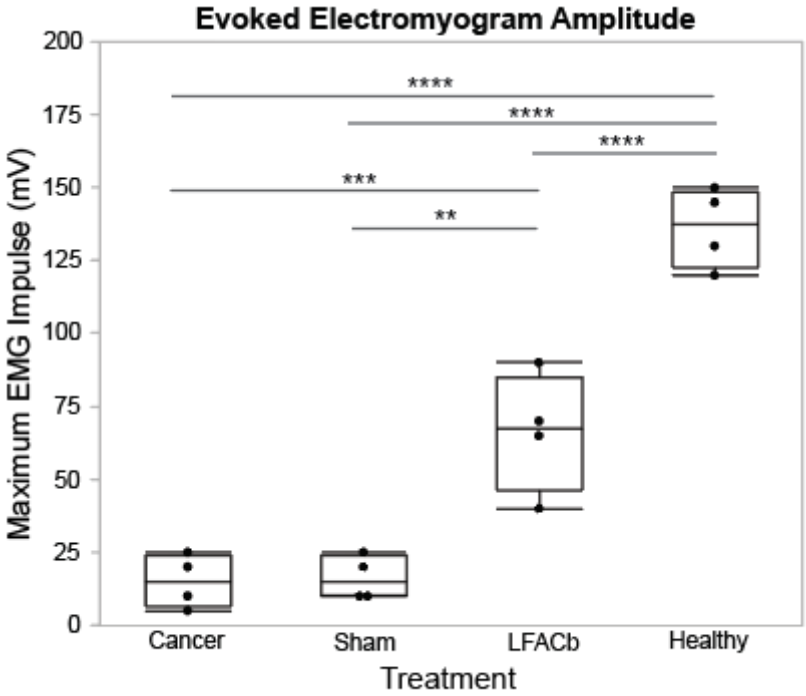

Figure 57: LFACb attenuates but does not eliminate reduction in magnitude of evoked EMG.Statistical significance determined by ANOVA with Tukey post-hoc correction for multiple comparisons. ** indicates p < 0.01, * indicates p < 0.001, **** indicates p <0.0001.**

5.4 Vagal Block Attenuates Anorexic Eating Patterns

As described in section 4.3, daily food consumption by mice provided unrestricted access to food was recorded. The average daily food consumption during the last week prior to euthanasia is plotted in Figure 58. All groups except untreated cancer animals and sham animals are significantly different. LFACb animals consume significantly more food than untreated cancer animals and sham animals, but still consume significantly less food than healthy controls.

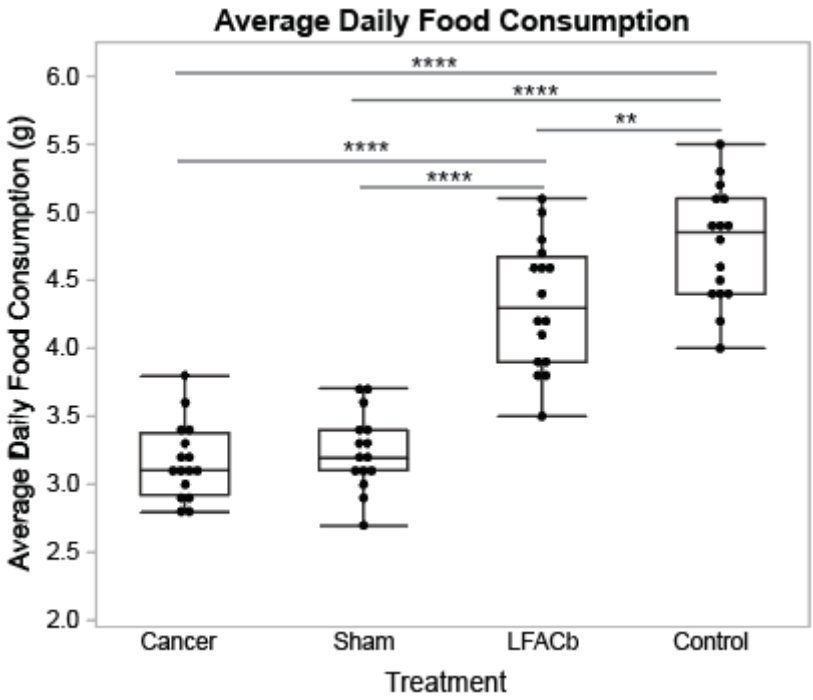

Figure 58: LFACb reduces anorexic eating behaviors.Statistical analysis of average daily food consumption was assessed by ANOVA with Tukey post-hoc correction for multiple comparisons. ** indicates p < 0.01, ** indicates p < 0.0001.**

5.5 Vagal Block Normalizes Inflammatory Cytokine Levels

Vagal block also attenuates inflammatory cytokine elevation observed in CAC (Figure 59). While the degree of reduction is not as great as that demonstrated in vagotomized animals, levels of TNFα, IL-1β, IL-2, IFN-γ, MIP-2, and IL-27p28/IL-30 levels in animals receiving LFACb are not statistically significant from healthy controls although untreated animals consistently are. There appears to be some mild attenuation of IL-1β in sham animals as well; this could be a result of random sampling error, or it could be an indicator that the implant surgery may impact the vagus nerve subtly even in absence of current delivery. No significant differences were detected between any treatment groups for IL-5, Il-6, IL-10, IL-33, or KC/GRO. Serum levels of IL-4, IL-9, IL-12, IL-15, and IL-17 were below the detection threshold for most animals, precluding analysis.

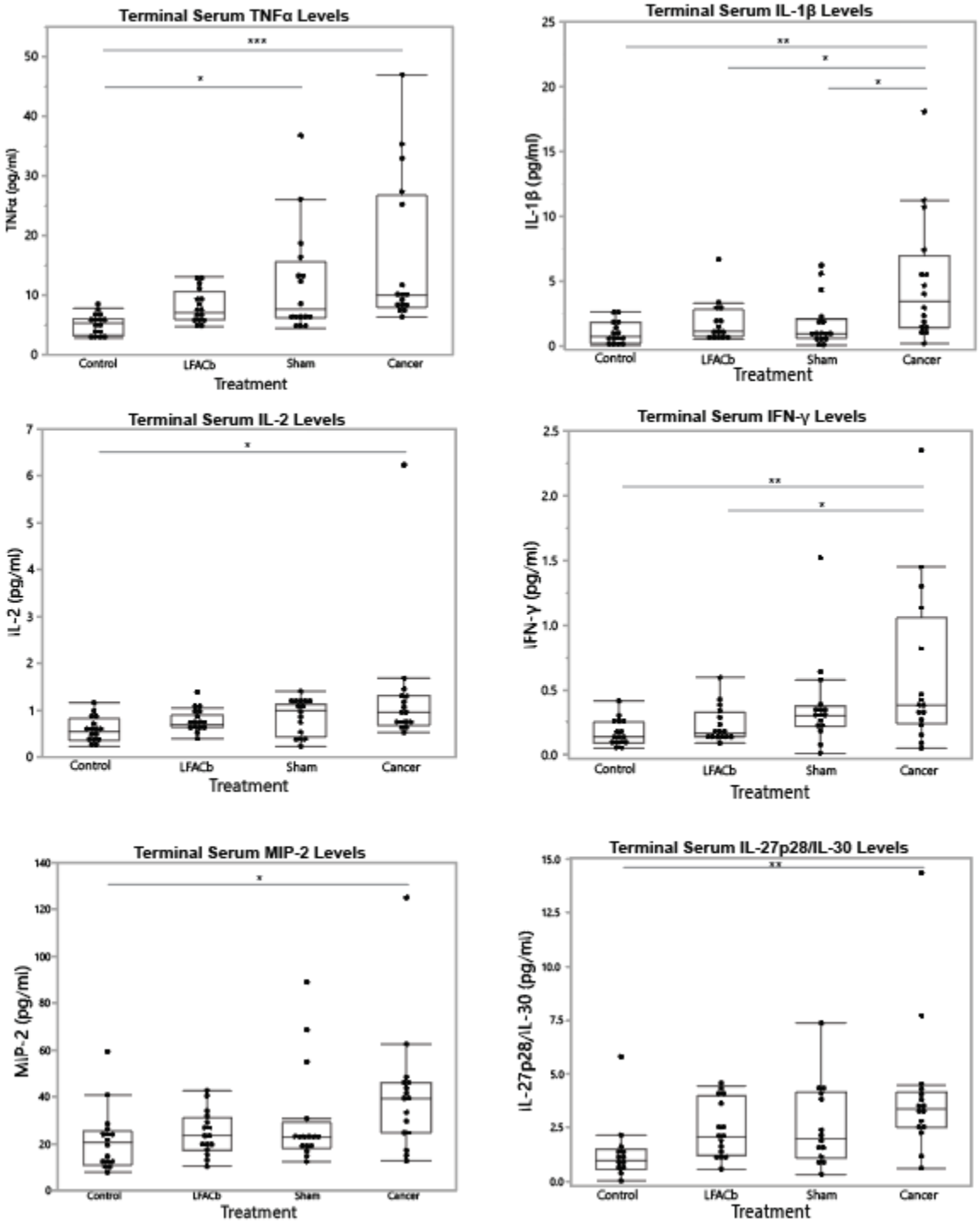

Figure 59: LFACb partially relieves inflammatory cytokine elevation in tumor-bearing rodents. Statistical significance was determined by ANOVA with

Tukey post-hoc correction for multiple comparisons. * indicates p < 0.05, ** indicates p < 0.01, * indicates p < 0.001.**

5.6 Vagal Block Increases Survival Duration in Cancer Bearing Mice

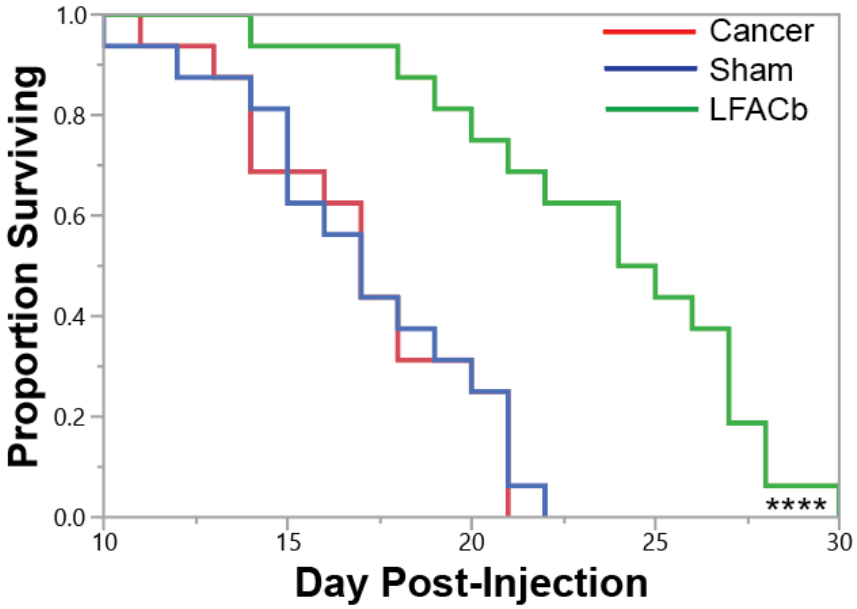

Figure 60: Mice receiving LFACb have extended survival compared to sham animals and untreated animals. Survival analyzed with the Kaplan-Meier method and compared with the log-rank test; ** indicates p < 0.0001.**

While sham and untreated animals have similar survival expectancies, LFACb have significantly extended lifespans, like vagotomized animals. Conservation of this critically important clinical metric for success reinforces the hypothesis that this therapeutic approach could provide meaningful improvement in outcomes for CAC patients with clinical translation.

6. Conclusion

In this dissertation I describe a toolbox to support neuromodulation of the gut-brain axis. In Section 2 I describe two novel abdominal windows for imaging colonic (Rakhilin et al., 2019) and embryonic (Huang et al., 2020) tissues chronically, at high resolution, in real time. These are supplemented by a whole mouse peripheral nerve atlas and quantitative tractography of the abdominal and thoracic organs described in Section 3 (Garrett et al., 2021). Together these tools provide a useful platform through which to select targets to modulate neuronal components of the gut-brain axis and visualize their downstream effects, with a focus on alleviating off-target impacts and improving our understanding and efficacy of neuromodulation therapies for clinical application. A proof-of-concept application of such neurostimulation is presented in Sections 4 and 5, in which cervical vagotomy or cervical vagal block respectively are used as two modes of neuromodulation in murine models of cancer-associated cachexia. This pervasive and fatal condition currently has no meaningful clinical treatments, making it a prime example of a space where development of therapeutics using novel approaches such as neurostimulation where drugs and biologics have previously failed of high importance.

References

Abell, T. L., Chen, J., Emmanuel, A., Jolley, C., Sarela, A. I. & Törnblom, H. 2015. Neurostimulation of the Gastrointestinal Tract: Review of Recent Developments. *Neuromodulation,* 18**,** 221-7; discussion 227.

Abraham, W. T. & Smith, S. A. 2013. Devices in the Management of Advanced, Chronic Heart Failure. *Nat Rev Cardiol,* 10**,** 98-110.

Alieva, M., Ritsma, L., Giedt, R. J., Weissleder, R. & Van Rheenen, J. 2014. Imaging Windows for Long-Term Intravital Imaging: General Overview and Technical Insights. *Intravital,* 3**,** e29917.

Allan Johnson, G., Wang, N., Anderson, R. J., Chen, M., Cofer, G. P., Gee, J. C., Pratson, F., Tustison, N. & White, L. E. 2019. Whole Mouse Brain Connectomics. *Journal of Comparative Neurology,* 527**,** 2146-2157.

Altschuler, S. M., Escardo, J., Lynn, R. B. & Miselis, R. R. 1993. The Central Organization of the Vagus Nerve Innervating the Colon of the Rat. *Gastroenterology,* 104**,** 502-9.

Amir, M., Yu, M., He, P. & Srinivasan, S. 2020. Hepatic Autonomic Nervous System and Neurotrophic Factors Regulate the Pathogenesis and Progression of Non-alcoholic Fatty Liver Disease. *Frontiers in Medicine,* 7.

Aoyagi, T., Terracina, K. P., Raza, A., Matsubara, H. & Takabe, K. 2015. Cancer Cachexia, Mechanism and Treatment. *World J Gastrointest Oncol,* 7**,** 17-29.

Arthur, S. T., Noone, J. M., Van Doren, B. A., Roy, D. & Blanchette, C. M. 2014. One-Year Prevalence, Comorbidities and Cost of Cachexia-Related Inpatient Admissions in the USA. *Drugs Context,* 3**,** 212265.

Baker, A.-M., Graham, T. A., Elia, G., Wright, N. A. & Rodriguez-Justo, M. 2015. Characterization of LGR5 Stem Cells in Colorectal Adenomas and Carcinomas. *Scientific Reports,* 5**,** 8654.

Baracos, V. E., Martin, L., Korc, M., Guttridge, D. C. & Fearon, K. C. H. 2018. Cancer-Associated Cachexia. *Nature Reviews Disease Primers,* 4**,** 17105.

Barker, N., Vanes, J. H., Kuipers, J., Kujala, P., Van Den Born, M., Cozijnsen, M., Haegbarth, A., Korving, J., Begthel, H., Peters, P. J. & Clevers, H. 2007. Identification of Stem Cells in Small Intestine and Colon by Marker Gene Lgr5. *Nature,* 449**,** 1003-1007.

Barth, B. B. & Shen, X. 2018. Computational Motility Models of Neurogastroenterology and Neuromodulation. *Brain Res,* 1693**,** 174-179.

Barth, B. B., Henriquez, C. S., Grill, W. M. & Shen, X. 2017. Electrical Stimulation of Gut Motility Guided by an In Silico Model. *J Neural Eng,* 14**,** 066010.

Bercik, P., Park, A. J., Sinclair, D., Khoshdel, A., Lu, J., Huang, X., Deng, Y., Blennerhassett, P. A., Fahnestock, M., Moine, D., Berger, B., Huizinga, J. D., Kunze, W., McLean, P. G., Bergonzelli, G. E., Collins, S. M. & Verdu, E. F. 2011. The Anxiolytic Effect of Bifidobacterium Longum NCC3001 Involves Vagal Pathways for Gut-Brain Communication. *Neurogastroenterol Motil,* 23**,** 1132-9.

Bharucha, A. E., Rao, S. S. C. & Shin, A. S. 2017. Surgical Interventions and the Use of Device-Aided Therapy for the Treatment of Fecal Incontinence and Defecatory Disorders. *Clin Gastroenterol Hepatol,* 15**,** 1844-1854.

Bonaz, B., Sinniger, V. & Pellissier, S. 2017. The Vagus Nerve in the Neuro-Immune Axis: Implications in the Pathology of the Gastrointestinal Tract. *Frontiers in Immunology,* 8.

Bray, F., Ferlay, J., Soerjomataram, I., Siegel, R. L., Torre, L. A. & Jemal, A. 2018. Global Cancer Statistics 2018: GLOBOCAN Estimates of Incidence and Mortality Worldwide for 36 Cancers in 185 Countries. *CA Cancer J Clin,* 68**,** 394-424.

Brierley, S. M., Hibberd, T. J. & Spencer, N. J. 2018. Spinal Afferent Innervation of the Colon and Rectum. *Frontiers in Cellular Neuroscience,* 12**,** 467-467.

Browning, K. N. & Travalgi, R. A. 2014. Central Nervous System Control of Gastrointestinal Motility and Secretion and Modulation of Gastrointestinal Functions. *Compr Physiol,* 4**,** 1339-68.

Browning, K. N., Verheijden, S. & Boeckxstaens, G. E. 2017. The Vagus Nerve in Appetite Regulation, Mood, and Intestinal Inflammation. *Gastroenterology,* 152**,** 730-744.

Butt, M. F., Albusoda, A., Farmer, A. D. & Aziz, Q. 2020. The Anatomical Basis for Transcutaneous Auricular Vagus Nerve Stimulation. *J Anat,* 236**,** 588-611.

Calabrese, E., Badea, A., Coe, C. L., Lubrach, G. R., Shi, Y., Styner, M. A. & Johnson, G. A. 2015. A Diffusion Tensor MRI Atlas of the Postmortem Rhesus Macaque Brain. *Neuroimage,* 117**,** 408-16.

Camborovà, P., Hubka, P., Sulková, I. & Hulín, I. 2003. The Pacemaker Activity of Interstitial Cells of Cajal and Gastric Electrical Activity. *Physiol Res,* 52**,** 275-84.

Campos, C. A., Bowen, A. J., Han, S., Wisse, B. E., Palmiter, R. D. & Schwartz, M. W. 2017. Cancer-Induced Anorexia and Malaise are Mediated by CGRP Neurons in the Parabrachial Nucleus. *Nat Neurosci,* 20**,** 934-942.

Carabotti, M. Scirocca, A., Maselli M. A. & Severi, C. 2015. The Gut-Brain Axis: Interactions Between Enteric Microbiota, Central and Enteric Nervous Systems. *Ann Gastroenterol,* 28**,** 203-209.

Carrington, E. V., Evers, J., Grossi, U., Dinning, P. G., Scott, S. M., O'Connell, P. R., Jones, J. F. & Knowles, C. H. 2014. A Systematic Review of Sacral Nerve Stimulation Mechanisms in the Treatment of Fecal Incontinence and Constipation. *Neurogastroenterol Motil,* 26**,** 1222-37.

Chakravarthy, K., Chaudhry, H., Williams, K. & Christo, P. J. 2015. Review of the Uses of Vagal Nerve Stimulation in Chronic Pain Management. *Curr Pain Headache Rep,* 19**,** 54.

Chang, R. B., Strochlic, D. E., Williams, E. K., Umans, B. D. & Liberles, S. D. 2015. Vagal Sensory Neuron Subtypes that Differentially Control Breathing. *Cell,* 161**,** 622-633.

Chassaing, B., Aitken, J. D., Malleshappa, M. & Vijay-Kumar, M. 2014. Dextran Sulfate Sodium (DSS)-Induced Colitis in Mice. *Curr Protoc Immunol,* 104**,** 15.25.1-15.25.14.

Cheng, H. & Leblond, C. P. 1974. Origin, Differentiation and Renewal of the Four Main Epithelial Cell Types in the Mouse Small Intestine V. Unitarian Theory of the Origin of the Four Epithelial Cell Types. *American Journal of Anatomy,* 141**,** 537-561.

Chey, W. D., Kurlander, J. & Eswaran, S. 2015. Irritable Bowel Syndrome: a Clinical Review. *Jama,* 313**,** 949-58.

Chu, L. A., Lu, C. H., Yang, S. M., Liu, Y. T., Feng, K. L., Tsai, Y. C., Chang, W. K., Wang, W. C., Chang, S. W., Chen, P., Lee, T. K., Hwu, Y. K., Chiang, A. S. & Chen, B. C. 2019. Rapid Single-Wavelength Lightsheet Localization Microscopy for Clarified Tissue. *Nat Commun,* 10**,** 4762.

Ciobanu, L. & Pennington, C. H. 2004. 3D Micron-Scale MRI of Single Biological Cells. *Solid State Nucl Magn Reson,* 25**,** 138-41.

Combs, C. A. & Shroff, H. 2017. Fluorescence Microscopy: A Concise Guide to Current Imaging Methods. *Curr Protoc Neurosci,* 79**,** 2 1 1-2 1 25.

Conde, S. V. 2021. Low Frequency Conduction Block: a Promising New Technique to Advance Bioelectronic Medicines. *Bioelectronic Medicine,* 7**,** 11.

Da Rocha, I. M. G., Marcadenti, A., De Medeiros, G. O. C., Bezerra, R. A., Rego, J. F. M., Gonzalez, M. C. & Fayh, A. P. T. 2019. Is Cachexia Associated With Chemotherapy Toxicities in Gastrointestinal Cancer Patients? A Prospective Study. *J Cachexia Sarcopenia Muscle,* 10**,** 445-454.

De Lartigue, G. 2016. Role of the Vagus Nerve in the Development and Treatment of Diet-Induced Obesity. *J Physiol,* 594**,** 5791-5815.

De Sousa Cavalcante, M. L., Silva, M. S., Cavalcante, A. K. M., De Oliviera Santos, R., Nunes, D. D. T., Busquets, S., Argiles, J. M., Seelaender, M., De Matos Neto, E. M., Dos Santos, A. A. & Da Silva, M. T. B. 2020. Win 55,212-2, atenolol and Subdiaphragmatic Vagotomy Prevent Acceleration of Gastric Emptying Induced by Cachexia via Yoshida-AH-130 Cells in Rats. *Eur J Pharmacol,* 877**,** 173087.

De Sousa E Melo, F., Kurtova, A. V., Harnoss, J. M., Kljavin, N., Hoeck, J. D., Hung, J., Anderson, J. E., Storm, E. E., Modrusan, Z., Koeppen, H., Dijkgraaf, G. J. P., Piskol, R. & De Sauvage, F. J. 2017. A Distinct Role for Lgr5+ Stem Cells in Primary and Metastatic Colon Cancer. *Nature,* 543**,** 676-680.

Dekker, E., Tanis, P. J., Vleugels, J. L. A., Kasi, P. M. & Wallace, M. B. 2019. Colorectal Cancer. *Lancet,* 394**,** 1467-1480.

Deshmukh, A., Brown, L., Barbe, M. F., Braverman, A. S., Tiwari, E., Hobson, L., Shunmugam, S., Armitage, O., Hewage, E., Ruggieri, M. R., SR. & Morizio, J. 2020. Fully Implantable Neural Recording and Stimulation Interfaces: Peripheral Nerve Interface Applications. *J Neurosci Methods,* 333**,** 108562.

Dhanapal, R., Saraswathi, T. & Rajkumar, N. 2011. Cancer Cachexia. *Journal of Oral and Maxillofacial Pathology,* 15**,** 257-260.

Dodson, S., Baracos, V. E., Jatoi, A., Evans, W. J., Cella, D., Dalton, J. T. & Steiner, M. S. 2011. Muscle Wasting in Cancer Cachexia: Clinical Implications, Diagnosis, and Emerging Treatment Strategies. *Annu Rev Med,* 62**,** 265-79.

Du, H., Hou, P., Zhang, W. & Li, Q. 2018. Advances in CLARITY-Based Tissue Clearing and Imaging. *Exp Ther Med,* 16**,** 1567-1576.

Dudding, T. C., Vaizey, C. J., Gibbs, A. & Kamm, M. A. 2009. Improving the Efficacy of Sacral Nerve Stimulation for Faecal Incontinence by Alteration of Stimulation Parameters. *Br J Surg,* 96**,** 778-84.

Durham, W. J., Dillon, E. L. & Sheffield-Moore, M. 2009. Inflammatory Burden and Amino Acid Metabolism in Cancer Cachexia. *Curr Opin Clin Nutr Metab Care,* 12**,** 72-7.

Elmentaite, R., Ross, A. D. B., Robers, K., James, K. R., Ortmann, D., Gomes, T., Nayack, K., Tuck, L., Pritchard, S., Bayraktar, O. A., Heuschkel, R., Vallier, L., Teichmann, S. A. & Zilbauer, M. 2020. Single-Cell Sequencing of Developing Human Gut Reveals Transcriptional Links to Childhood Crohn's Disease. *Dev Cell,* 55**,** 771-783 e5.

Entenberg, D., Voiculescu, S., Guo, P., Borriello, L., Wang, Y., Karagiannis, G. S., Jones, J., Baccay, F., Oktay, M. & Condeelis, J. 2018. A Permanent Window for the Murine Lung Enables High-Resolution Imaging of Cancer Metastasis. *Nat Methods,* 15**,** 73-80.

Fallahzadeh Abarghuei, A. & Karimi, M. T. 2022. Evaluation the Efficiency of Electrical Stimulation Advanced Methods on Management of Bowel and Bladder Functions in Spinal Cord Injury Subject; A Systematic Review of Literature. *Bull Emerg Trauma,* 10**,** 1-8.

Farrar, M. J., Bernstein, I. M., Schlafer, D. H., Cleland, T. A., Fetcho, J. R. & Schaffer, C. B. 2012. Chronic In Vivo Imaging in the Mouse Spinal Cord Using an Implanted Chamber. *Nat Methods,* 9**,** 297-302.

Fassov, J., Lundby, L., Laurberg, S. & Krogh, K. 2019. Sacral Nerve Modulation for Irritable Bowel Syndrome: a Randomized, Double-Blinded, Placebo-Controlled Crossover Study. *Neurogastroenterol Motil,* 31**,** e13570.

Fazan, V. P., Ma, X., Chapleau, M. W. & Barriera, A. A. 2002. Qualitative and Quantitative Morphology of Renal Nerves in C57BL/6J Mice. *Anat Rec,* 268**,** 399-404.

Fearon, K., Strasser, F., Anker, S. D., Bosaeus, I., Bruera, E., Fainsinger, R. L., Jatoi, A., Loprinzi, C., MacDonald, N., Mantovani, G., Davis, M., Muscaritoli, M., Ottery, F., Radbruch, L., Ravasco, P., Walsh, D., Wilcock, A., Kaasa, S. & Baracos, V. E. 2011. Definition and Classification of Cancer Cachexia: an International Consensus. *Lancet Oncol,* 12**,** 489-95.

Fearon, K. C., Glass, D. J. & Guttridge, D. C. 2012. Cancer Cachexia: Mediators, Signaling, and Metabolic Pathways. *Cell Metab,* 16**,** 153-66.

Feldman-Goriachnik, R., Belzer, V. & Hanani, M. 2015. Systemic Inflammation Activates Satellite Glial Cells in the Mouse Nodose Ganglion and Alters Their Functions. *Glia,* 63**,** 2121-2132.

Foldes, E. L., Ackermann, D. M., Bhadra, N. & Kilgore, K. L. Counted Cycles Method to Quantify the Onset Response in High-Frequency Peripheral Nerve Block. *2009 Annual International Conference of the IEEE Engineering in Medicine and Biology Society*, 3-6 Sept. 2009 2009. 614-617.

Foster, J. A., Rinaman, L. & Cryan, J. F. 2017. Stress & the Gut-Brain Axis: Regulation by the Microbiome. *Neurobiol Stress,* 7**,** 124-136.

Furness, J. B. 2008. The Enteric Nervous System: Normal Functions and Enteric Neuropathies. *Neurogastroenterol Motil,* 20 Suppl 1**,** 32-8.

Furness, J. B. 2012. The Enteric Nervous System and Neurogastroenterology. *Nat Rev Gastroenterol Hepatol,* 9**,** 286-94.

Garrett, A., Rakhilin, N., Wang, N., McKey, J., Cofer, G., Anderson, R. B., Capel, B., Johnson, G. A. & Shen, X. 2021. Mapping the Peripheral Nervous System in the Whole Mouse via Compressed Sensing Tractography. *J Neural Eng,* 18.

Göbel, C. H., Tronnier, V. M. & Münte, T. F. 2017. Brain Stimulation in Obesity. *Int J Obes (Lond),* 41**,** 1721-1727.

Goldey, G. J., Roumis, D. K., Glickfeld, L. L., Kerlin, A. M., Reid, R. C., Bonin, V., Schafer, D. P. & Andermann, M. L. 2014. Removable Cranial Windows for Long-Term Imaging in Awake Mice. *Nature Protocols,* 9**,** 2515-2538.

Grimm, M. C., Pullman, W. E., Bennett, G. M., Sullivan, P. J., Pavli, P. & Doe, W. F. 1995. Direct Evidence of Monocyte Recruitment to Inflammatory Bowel Disease Mucosa. *J Gastroenterol Hepatol,* 10**,** 387-95.

Groves, D. A. & Brown, V. J. 2005. Vagal Nerve Stimulation: a Review of Its Applications and Potential Mechanisms that Mediate Its Clinical Effects. *Neurosci Biobehav Rev,* 29**,** 493-500.

Gullett, N. P., Mazurak, V. C., Hebbar, G. & Ziegler, T. R. 2011. Nutritional Interventions for Cancer-Induced Cachexia. *Curr Probl Cancer,* 35**,** 58-90.

Guo, Y. P., McLeod, J. G. & Baverstock, J. 1987. Pathological Changes in the Vagus Nerve in Diabetes and Chronic Alcoholism. *J Neurol Neurosurg Psychiatry,* 50**,** 1449-53.

Haberberger, R. V., Barry, C., Dominguez, N. & Matusica, D. 2019. Human Dorsal Root Ganglia. *Frontiers in Cellular Neuroscience,* 13.

Han, W., Tellez, L. A., Perkins, M. H., Perez, I. O., Qu, T., Ferreira, J., Ferreira, T. L., Quinn, D., Liu, Z.-W., Gao, X.-B., Kaelberer, M. M., Bohórquez, D. V., Shammah-Lagnado, S. J., De Lartigue, G. & De Araujo, I. E. 2018. A Neural Circuit for Gut-Induced Reward. *Cell,* 175**,** 665-678.e23.

Hasan, W. 2013. Autonomic Cardiac Innervation. *Organogenesis,* 9**,** 176-193.

Herrity, A. N., Rau, K. K., Petruska, J. C., Stirling, D. P. & Hubscher, C. H. 2014. Identification of Bladder and Colon Afferents in the Nodose Ganglia of Male Rats. *J Comp Neuro,* 522**,** 3667-3682.

Hillman, E. T., Lu, H., Yao, T. & Nakatsu, C. H. 2017. Microbial Ecology Along the Gastrointestinal Tract. *Microbes Environ,* 32**,** 300-313.

Hilton, A., Jorgensen, A., Gardiner, B., Robinson, S., Lambert, H. W., Morton, D. & Wisco, J. 2017. Visualization of Differential Myelinated Cardiac Plexus Fiber

Innervation in Heart Failure Using the Sihler's Stain Technique. *The FASEB Journal,* 31**,** 585.8-585.8.

Holtmaat, A., Bonhoeffer, T., Chow, D. K., Chuckowree, J., De Paola, V., Hofer, S. B., Hübener, M., Keck, T., Knott, G., Lee, W.-C. A., Mostany, R., Mrsic-Flogel, T. D., Nedivi, E., Portera-Cailliau, C., Svoboda, K., Trachtenberg, J. T. & Wilbrecht, L. 2009. Long-Term, High-Resolution Imaging in the Mouse Neocortex Through a Chronic Cranial Window. *Nature Protocols,* 4**,** 1128-1144.

Horn, M. R., Ahmen, C. & Yoshida, K. Low Frequency Alternating Current Block - A New Method to Stop or Slow Conduction of Action Potentials. *2019 9th International IEEE/EMBS Conference on Neural Engineering (NER),* 20-23 March 2019 2019. 787-790.

Huang, Q., Cohen, M. A., Alsina, F. C., Devlin, G., Garrett, A., McKey, J., Havlik, P., Rakhilin, N., Wang, E., Xiang, K., Mathews, P., Wang, L., Bock, C., Ruthig, V., Wang, Y., Negrete, M., Wong, C. W., Murthy, P. K. L., Zhang, S., Daniel, A. R., Kirsch, D. G., Kang, Y., Capel, B., Asokan, A., Silver, D. L., Jaenisch, R. & Shen, X. 2020. Intravital Imaging of Mouse Embryos. *Science,* 368**,** 181-186.

Huang, Q., Garrett, A., Bose, S., Blocker, S., Rios, A. C., Clevers, H. & Shen, X. 2021. The Frontier of Live Tissue Imaging Across Space and Time. *Cell Stem Cell,* 28**,** 603-622.

Iachetta, R. P., Cola, A. & Villani, R. D. 2012. Sacral Nerve Stimulation in the Treatment of Fecal Incontinence - the Experience of a Pelvic Floor Center: Short Term Results. *J Interv Gastroenterol,* 2**,** 189-192.

Jakob, M. O., Murugan, S. & Klose, C. S. N. 2020. Neuro-Immune Circuits Regulate Immune Responses in Tissues and Organ Homeostasis. *Front Immunol,* 11**,** 308.

Jandhyala, S. M., Talukdar, R., Subramanyam, C., Vuyyuru, H., Sasikala, M. & Nageshward Reddy, D. 2015. Role of the Normal Gut Microbiota. *World J Gastroenterol,* 21**,** 8787-803.

Jeon, T., Fung, M. M., Koch, K. M., Tan, E. T. & Sneag, D. B. 2018. Peripheral Nerve Diffusion Tensor Imaging: Overview, Pitfalls, and Future Directions. *J Magn Reson Imaging,* 47**,** 1171-1189.

Jiang, Y. & Johnson, G. A. 2010. Microscopic Diffusion Tensor Imaging of the Mouse Brain. *NeuroImage,* 50**,** 465-471.

Johnson, G. A., Benveniste, H., Black, R. D., Hedlund, L. W., Maronpot, R. R. & Smith, B. R. 1993. Histology by Magnetic Resonance Microscopy. *Magn Reson Q,* 9**,** 1-30.

Johnson, G. A., Cofer, G. P., Gewalt, S. L. & Hedlund, L. W. 2002. Morphologic Phenotyping with MR Microscopy: the Visible Mouse. *Radiology,* 222**,** 789-93.

Johnson, R. L. & Wilson, C. G. 2018. A Review of Vagus Nerve Stimulation as a Therapeutic Intervention. *J Inflamm Res,* 11**,** 203-213.

Kaelberer, M. M., Buchanan, K. L., Klein, M. E., Barth, B. B., Montoya, M. M., Shen, X. & Bohórquez, D. V. 2018. A Gut-Brain Neural Circuit for Nutrient Sensory Transduction. *Science,* 361.

Kaelberer, M. M. & Jordt, S. E. 2016. A Method to Target and Isolate Airway-innervating Sensory Neurons in Mice. *J Vis Exp*.

Kalantar-Zadeh, K., Rhee, C., Sim, J. J., Stenvinkel, P., Anker, S. D. & Kovesdy, C. P. 2013. Why Cachexia Kills: Examining the Causality of Poor Outcomes in Wasting Conditions. *J Cachexia Sarcopenia Muscle,* 4**,** 89-94.

Kaplan, A. S. & Vatter, A. E. 1959. A Comparison of Herpes Simplex and Pseudorabies Viruses. *Virology,* 7**,** 394-407.

Kaplan, G. G. 2015. The Global Burden of IBD: From 2015 to 2025. *Nat Rev Gastroenterol Hepatol,* 12**,** 720-7.

Kenefick, N. J., Nicholls, R. J., Cohen, R. G. & Kamm, M. A. 2002. Permanent Sacral Nerve Stimulation for Treatment of Idiopathic Constipation. *Br J Surg,* 89**,** 882-8.

Koopman, F. A., Chavan, S. S., Miljko, S., Grazio, S., Sokolovic, S., Schuurman, P. R., Mehta, A. D., Levine, Y. A., Faltys, M., Zitnik, R., Tracey, K. J. & Tak, P. P. 2016. Vagus Nerve Stimulation Inhibits Cytokine Production and Attenuates Disease Severity in Rheumatoid Arthritis. *Proc Natl Acad Sci U S A,* 113**,** 8284-9.

Krahl, S. E. 2012. Vagus Nerve Stimulation for Epilepsy: A Review of the Peripheral Mechanisms. *Surg Neurol Int,* 3**,** S47-52.

Kulkarni, S., Micci, M. A., Leser, J., Shin, C., Tang, S. C., Fu, Y. Y., Liu, L., Li, Q., Saha, M., Li, C., Enikolopov, G., Becker, L., Rakhilin, N., Anderson, M., Shen, X., Dong, X., Butte, M. J., Song, H., Southard-Smith, E. M., Kapur, R. P., Bogunovik, M. & Pasricha, P. J. 2017. Adult Enteric Nervous System in Health is Maintained by a Dynamic Balance Between Neuronal Apoptosis and Neurogenesis. *Proc Natl Acad Sci U S A,* 114**,** E3709-E3718.

Kupari, J., Haring, M., Agirre, E., Castelo-Branco, G. & Ernfors, P. 2019. An Atlas of Vagal Sensory Neurons and Their Molecular Specialization. *Cell Rep,* 27**,** 2508-2523 e4.

Lahner, E., Bellentani, S., Bastiani, R. D., Tosetti, C., Cicala, M., Esposito, G., Arullani, P. & Annibale, B. 2013. A Survey of Pharmacological and Nonpharmacological

Treatment of Functional Gastrointestinal Disorders. *United European Gastroenterol J,* 1**,** 385-93.

Lanzman, R. S. & Wittsack, H. J. 2017. Diffusion Tensor Imaging in Abdominal Organs. *NMR Biomed,* 30.

Lehr, H. A., Leunig, M., Menger, M. D., Nolte, D. & Messmer, K. 1993. Dorsal Skinfold Chamber Technique for Intravital Microscopy in Nude Mice. *Am J Pathol,* 143**,** 1055-62.

Lelkes, E., Headley, M. B., Thornton, E. E., Looney, M. R. & Krummel, M. F. 2014. The Spatiotemporal Cellular Dynamics of Lung Immunity. *Trends in Immunology,* 35**,** 379-386.

Liu, B., Fang, F., Pedersen, N. L., Tillander, A., Ludvigsson, J. F., Ekbom, A., Svenningsson, P., Chen, H. & Wirdefeldt, K. 2017. Vagotomy and Parkinson Disease: a Swedish Register-Based Matched-Cohort Study. *Neurology,* 88**,** 1996-2002.

Liu, D. S. & Xu, T. L. 2019. Cell-Type Identification in the Autonomic Nervous System. *Neurosci Bull,* 35**,** 145-155.

Lope-Piedrafita, S. 2018. Diffusion Tensor Imaging (DTI). *Methods Mol Biol,* 1718**,** 103-116.

Luckner, M., Burgold, S., Filser, S., Scheungrab, M., Niyaz, Y., Hummel, E., Wanner, G. & Herms, J. 2018. Label-free 3D-CLEM Using Endogenous Tissue Landmarks. *Iscience,* 6**,** 92-101.

Lyte, M. 2014. Microbial Endocrinology and the Microbiota-Gut-Brain Axis. *Adv Exp Med Biol,* 817**,** 3-24.

Maeda, A. & Dacosta, R. S. 2014. Optimization of the Dorsal Skinfold Window Chamber Model and Multi-Parametric Characterization of Tumor-Associated Vasculature. *Intravital,* 3**,** e27935.

Malbert, C. H., Picq, C., Divoux, J. L., Henry, C. & Horowitz, M. 2017. Obesity-Associated Alterations in Glucose Metabolism Are Reversed by Chronic Bilateral Stimulation of the Abdominal Vagus Nerve. *Diabetes,* 66**,** 848-857.

Marceca, G. P., Londhe, P. & Calore, F. 2020. Management of Cancer Cachexia: Attempting to Develop New Pharmacological Agents for New Effective Therapeutic Options. *Front Oncol,* 10**,** 298.

Matsuhisa, M., Yamaski, Y., Shiba, Y., Nakahara, I., Kuroda, A., Tomita, T., Iida, M., Ikeda, M., Kajimoto, Y., Kubota, M. & Hori, M. 2000. Important Role of the

Hepatic Vagus Nerve in Glucose Uptake and Production by the Liver. *Metabolism,* 49**,** 11-6.

Matsumoto, K., Mitani, T. T., Horiguchi, S. A., Kaneshiro, J., Murakami, T. C., Mano, T., Fujishima, H., Konno, A., Watanabe, T. M., Hirai, H. & Ueda, H. R. 2019. Advanced CUBIC Tissue Clearing for Whole-Organ Cell Profiling. *Nature Protocols,* 14**,** 3506-3537.

Mayer, E. A. 2011. Gut Feelings: the Emerging Biology of Gut-Brain Communication. *Nat Rev Neurosci,* 12**,** 453-66.

McKey, J., Cameron, L. A., Lewis, D., Batchvarov, I. S. & Capel, B. 2020. Combined iDISCO and CUBIC Tissue Clearing and Lightsheet Microscopy for In Toto Analysis of the Adult Mouse Ovarydagger. *Biol Reprod,* 102**,** 1080-1089.

Miller, S. M. & Szurszewski, J. H. 1997. Colonic Mechanosensory Afferent Input to Neurons in the Mouse Superior Mesenteric Ganglion. *American Journal of Physiology-Gastrointestinal and Liver Physiology,* 272**,** G357-G366.

Mintch, L. M., Muzquiz, I., Horn, M. R., Carr, M., Schild, J. H. & Yoshida, K. Reversible Conduction Block in Peripheral Mammalian Nerve Using Low Frequency Alternating Current. *2019 9th International IEEE/EMBS Conference on Neural Engineering (NER),* 20-23 March 2019. 823-824.

Mizutani, M., Pino, P. A., Saederup, N., Charo, I. F., Ransohoff, R. M. & Cardona, A. E. 2012. The Fractalkine Receptor but not CCR2 is Present on Microglia from Embryonic Development Throughout dulAthood. *J Immunol,* 188**,** 29-36.

Mkaya Mwamburi, M. D. P. M. A., Eric J. Liebler, B. A. & Andrew T. Tenaglia, B. A. 2017. Review of Non-Invasive Vagus Nerve Stimulation (gammaCore): Efficacy, Safety, Potential Impact on Comorbidities, and Economic Burden for Episodic and Chronic Cluster Headache. *Supplements and Featured Publications,* 23.

Mohan, A., Poulose, R., Kulshreshtha, I., Chautani, A. M., Madan, K., Hadda, V. & Guleria, R. 2017. High Prevalence of Malnutrition and Deranged Relationship Between Energy Demands and Food Intake in Advanced Non-Small Cell Lung Cancer. *Eur J Cancer Care (Engl),* 26.

Morarach, K., Mikhailova, A., Knoflach, V., Memic, F., Kumar, R., Li, W., Ernfors, P. & Marklund, U. 2021. Diversification of Molecularly Defined Myenteric Neuron Classes Revealed by Single-Cell RNA Sequencing. *Nat Neurosci,* 24**,** 34-46.

Mori, S., Itoh, R., Zhang, J., Kaufmann, W. E., Van Zijl, P. C., Solaiyappan, M. & Yarowsky, P. 2001. Diffusion Tensor Imaging of the Developing Mouse Brain. *Magn Reson Med,* 46**,** 18-23.

Morris, A. D., Lewis, G. M. & Kucenas, S. 2017. Perineurial Glial Plasticity and the Role of TGF-β in the Development of the Blood–Nerve Barrier. *The Journal of Neuroscience,* 37**,** 4790-4807.

Morsi, M., Maher, A., Aboelmagd, O., Johar, D. & Bernstein, L. 2018. A Shared Comparison of Diabetes Mellitus and Neurodegenerative Disorders. *J Cell Biochem,* 119**,** 1249-1256.

Muzquiz, M. I., Richardson, L., Vetter, C., Smolik, M., Alhawwash, A., Goodwill, A., Bashirullah, R., Carr, M. & Yoshida, K. 2021. In-Vivo Application of Low Frequency Alternating Currents on Porcine Cervical Vagus Nerve Evokes Reversible Nerve Conduction Block. *Bioelectronic Medicine,* 7**,** 9.

Mwamburi, M., Liebler, E. J. & Staats, P. S. 2020. Patient Experience with Non-Invasive Vagus Nerve Stimulator: GammaCore Patient Registry. *Am J Manag Care,* 26**,** S15-s19.

Mwamburi, M., Liebler, E. J. & Tenaglia, A. T. 2017. Review of Non-Invasive Vagus Nerve Stimulation (GammaCore): Efficacy, Safety, Potential Impact on Comorbidities, and Economic Burden for Episodic and Chronic Cluster Headache. *Am J Manag Care,* 23**,** S317-s325.

Naqvi, I., Gunaratne, R., McDade, J. E., Moreno, A., Rempel, R. E., Rouse, D. C., Herrera, S. G., Pisetsky, D. S., Lee, J., White, R. R. & Sullenger, B. A. 2018. Polymer-Mediated Inhibition of Pro-invasive Nucleic Acid DAMPs and Microvesicles Limits Pancreatic Cancer Metastasis. *Mol Ther,* 26**,** 1020-1031.

Naso, M. F., Tomkowicz, B., Perry, W. L., 3rd & Strohl, W. R. 2017. Adeno-Associated Virus (AAV) as a Vector for Gene Therapy. *BioDrugs : Clin Immuno, Biopharm and Gene Ther,* 31**,** 317-334.

Nobis, M., Herrmann, D., Warren, S. C., Kadir, S., Leung, W., Killen, M., Magenau, A., Stevenson, D., Lucas, M. C. & Reischmann, N. 2017. A RhoA-FRET Biosensor Mouse for Intravital Imaging in Normal Tissue Homeostasis and Disease Contexts. *Cell Reports,* 21**,** 274-288.

O'Connell, T. M., Golzarri-Arroyo, L., Pin, F., Barreto, R., Dickinson, S. L., Couch, M. E. & Bonetto, A. 2021. Metabolic Biomarkers for the Early Detection of Cancer Cachexia. *Front Cell Dev Biol,* 9**,** 720096.

Ohnuma, T. 2003. Treatment of Cachexia. *In:* D.W. Kufe, R.P., R.R. Weichselbaum, R.C. Bast, T.S. Gansler, J.F. Holland, E. Frei (ed.) *Holland-Frei Cancer Medicine.* 6 ed. Hamilton (ON): BC Decker.

Okayasu, I., Hatakeyama, S., Yamada, M., Ohkusa, T., Inagaki, Y. & Nakaya, R. 1990. A Novel Method in the Induction of Reliable Experimental Acute and Chronic Ulcerative Colitis in Mice. *Gastroenterology,* 98**,** 694-702.

Opazo, M. C., Ortega-Rocha, E. M., Coronado-Arrazola, I., Bonifaz, L. C., Boudin, H., Neunlist, M., Bueno, S. M., Kalergis, A. M. & Riedel, C. A. 2018. Intestinal Microbiota Influences Non-intestinal Related Autoimmune Diseases. *Front Microbiol,* 9**,** 432.

Patel, Y. A., Saxena, T., Bellamkonda, R. V. & Butera, R. J. 2017. Kilohertz Frequency Nerve Block Enhances Anti-Inflammatory Effects of Vagus Nerve Stimulation. *Scientific Reports,* 7**,** 39810.

Paul, S. P. & Basude, D. 2016. Non-Pharmacological Management of Abdominal Pain-Related Functional Gastrointestinal Disorders in Children. *World J Pediatr,* 12**,** 389-398.

Paulon, E., Nastou, D., Jaboli, F., Marin, J., Liebler, E. & Epstein, O. 2017. Proof of Concept: Short-Term Non-Invasive Cervical Vagus Nerve Stimulation in Patients with Drug-Refractory Gastroparesis. *Frontline Gastroenterol,* 8**,** 325-330.

Pavlov, V. A. & Tracey, K. J. 2012. The Vagus Nerve and the Inflammatory Reflex-Linking Immunity and Metabolism. *Nat Rev Endocrinol,* 8**,** 743-54.

Payne, S. C., Furness, J. B. & Stebbing, M. J. 2019. Bioelectric Neuromodulation for Gastrointestinal Disorders: Effectiveness and Mechanisms. *Nat Rev Gastroenterol Hepatol,* 16**,** 89-105.

Pelot, N. A., Goldhagen, G. B., Cariello, J. E., Musselman, E. D., Clissold, K. A., Ezzell, J. A. & Grill, W. M. 2020. Quantified Morphology of the Cervical and Subdiaphragmatic Vagus Nerves of Human, Pig, and Rat. *Front Neurosci,* 14**,** 601479.

Pelot, N. A. & Grill, W. M. 2020. In Vivo Quantification of Excitation and Kilohertz Frequency Block of the Rat Vagus Nerve. *J Neural Eng,* 17**,** 026005.

Petruzzelli, M. & Wagner, E. F. 2016. Mechanisms of Metabolic Dysfunction in Cancer-Associated Cachexia. *Genes Dev,* 30**,** 489-501.

Piliszek, A., Kwon, G. S. & Hadjantonakis, A. K. 2011. Ex Utero Culture and Live Imaging of Mouse Embryos. *Methods Mol Biol,* 770**,** 243-57.

Pinho, S. & Frenette, P. S. 2019. Haematopoietic Stem Cell Activity and Interactions with the Niche. *Nat Rev Mol Cell Biol,* 20**,** 303-320.

Porporato, P. E. 2016. Understanding Cachexia as a Cancer Metabolism Syndrome. *Oncogenesis,* 5**,** e200-e200.

Prado, B. L. & Qian, Y. 2018. Anti-Cytokines in the Treatment of Cancer Cachexia. *Annals of Palliative Medicine,* 8**,** 67-79.

Rakhilin, N., Barth, B., Choi, J., Munoz, N. L., Kulkarni, S., Jones, J. S., Small, D. M., Cheng, Y. T., Cao, Y., Lavinka, C., Kan, E., Dong, X., Spencer, M., Pasricha, P., Nishimura, N. & Shen, X. 2016. Simultaneous Optical and Electrical in Vivo Analysis of the Enteric Nervous System. *Nat Commun,* 7**,** 11800.

Rakhilin, N., Garrett, A., Eom, C. Y., Chavez, K. R., Small, D. M., Daniel, A. R., Kaelberer, M. M., Mejooli, M. A., Huang, Q., Ding, S., Kirsch, D. G., Bohórquez, D. V., Nishimura, N., Barth, B. B. & Shen, X. 2019. An Intravital Window to Image the Colon in Real Time. *Nat Commun,* 10**,** 5647.

Rani, V., Deshmukh, R., Jaswal, P., Kumar, P. & Bariwal, J. 2016. Alzheimer's Disease: Is This a Brain Specific Diabetic Condition? *Physiol Behav,* 164**,** 259-67.

Rao, M. & Gershon, M. D. 2016. The Bowel and Beyond: the Enteric Nervous System in Neurological Disorders. *Nat Rev Gastroenterol Hepatol,* 13**,** 517-28.

Renier, N., Wu, Z., Simon, D. J., Yang, J., Ariel, P. & Tessier-Lavigne, M. 2014. iDISCO: a Simple, Rapid Method to Immunolabel Large Tissue Samples for Volume Imaging. *Cell,* 159**,** 896-910.

Ritsma, L., Ellenbroek, S. I. J., Zomer, A., Snippert, H. J., De Sauvage, F. J., Simons, B. D., Clevers, H. & Van Rheenen, J. 2014. Intestinal Crypt Homeostasis Revealed at Single-Stem-Cell Level by In Vivo Live Imaging. *Nature,* 507**,** 362-365.

Ritsma, L., Steller, E. J., Beerling, E., Loomans, C. J., Zomer, A., Gerlach, C., Vrisekoop, N., Seinstra, D., Van Gurp, L., Schafer, R., Raats, D. A., DE Graaff, A., Schumacher, T. N., De Koning, E. J., Rinkes, I. H., Kranenburg, O. & Van Rheenen, J. 2012. Intravital Microscopy Through an Abdominal Imaging Window Reveals a Pre-Micrometastasis Stage During Liver Metastasis. *Sci Transl Med,* 4**,** 158ra145.

Roybal, A. E., Sivanesan, E. & Chen, Y. 2021. Case Report: Dorsal Root Ganglion (DRG) Stimulation for Acute Neuropathic Pain from Acute Herpes Zoster Infection. *SAGE Open Med Case Rep,* 9**,** 2050313x211062297.

Sampson, T. R., Debelius, J. W., Thron, T., Janssen, S., Shastri, G. G., Ilhan, Z. E., Challis, C., Schretter, C. E., Rocha, S., Gradinaru, V., Chesselet, M. F., Keshavarzian, A., Shannon, K. M., Krajmalnik-Brown, R., Wittung-Stafshede, P., Knight, R. & Mazmanian, S. K. 2016. Gut Microbiota Regulate Motor Deficits and Neuroinflammation in a Model of Parkinson's Disease. *Cell,* 167**,** 1469-1480.e12.

Sata, Y., Head, G. A., Denton, K., May, C. N. & Schlaich, M. P. 2018. Role of the Sympathetic Nervous System and Its Modulation in Renal Hypertension. *Front Med (Lausanne),* 5**,** 82.

Schneider, S., Wright, C. M. & Heuckeroth, R. O. 2019. Unexpected Roles for the Second Brain: Enteric Nervous System as Master Regulator of Bowel Function. *Annu Rev Physiol,* 81**,** 235-259.

Shahbazi, M. N. & Zernicka-Goetz, M. 2018. Deconstructing and Reconstructing the Mouse and Human Early Embryo. *Nat Cell Biol,* 20**,** 878-887.

Sharma, A., Bussen, D., Herold, A. & Jayne, D. 2013. Review of Sacral Neuromodulation for Management of Constipation. *Surg Innov,* 20**,** 614-24.

Šlauf, P. & Vobořil, R. 2021. Sacral Neuromodulation for Faecal Incontinence - 10 Years Experience and Long-Term Outcomes of a Specialized Centre. *Rozhl Chir,* 100**,** 475-483.

Spencer, N. J., Kyloh, M., Beckett, E. A., Brookes, S. & Hibberd, T. 2016a. Different Types of Spinal Afferent Nerve Endings in Stomach and Esophagus Identified by Anterograde Tracing from Dorsal Root Ganglia. *Journal of Comparative Neurology,* 524**,** 3064-3083.

Spencer, N. J., Zagorodnyuk, V., Brookes, S. J. & Hibberd, T. 2016b. Spinal Afferent Nerve Endings in Visceral Organs: Recent Advances. *American Journal of Physiology-Gastrointestinal and Liver Physiology,* 311**,** G1056-G1063.

Sung, H. Y., Park, J. W. & Kim, J. S. 2014. The Frequency and Severity of Gastrointestinal Symptoms in Patients with Early Parkinson's Disease. *J Mov Disord,* 7**,** 7-12.

Tajti, J., Szok, D., Nyári, A. & Vécsei, L. 2019. Therapeutic Strategies That Act on the Peripheral Nervous System in Primary Headache Disorders. *Expert Rev Neurother,* 19**,** 509-533.

Talley, N. J., Holtmann, G. & Walker, M. M. 2015. Therapeutic Strategies for Functional Dyspepsia and Irritable Bowel Syndrome Based on Pathophysiology. *J Gastroenterol,* 50**,** 601-13.

Tilborghs, S. & De Wachter, S. 2022. Sacral Neuromodulation for the Treatment of Overactive Bladder: Systematic Review and Future Prospects. *Expert Rev Med Devices,* 19**,** 161-187.

Van Den Berg, C. W., Koudijs, A., Ritsma, L. & Rabelink, T. J. 2020. In Vivo Assessment of Size-Selective Glomerular Sieving in Transplanted Human Induced Pluripotent Stem Cell-Derived Kidney Organoids. *J Am Soc Nephrol,* 31**,** 921-929.

Vaughan, V. C., Martin, P. & Lewandowski, P. A. 2013. Cancer Cachexia: Impact, Mechanisms and Emerging Treatments. *J Cachexia Sarcopenia Muscle,* 4, 95-109.

Vermeulen, W., De Man, J. G., Pelckmans, P. A. & De Winter, B. Y. 2014. Neuroanatomy of Lower Gastrointestinal Pain Disorders. *World J Gastroenterol,* 20, 1005-20.

Von Haehling, S., Anker, M. S. & Anker, S. D. 2016. Prevalence and Clinical Impact of Cachexia in Chronic Illness in Europe, USA, and Japan: Facts and Numbers Update 2016. *Journal of Cachexia, Sarcopenia and Muscle,* 7**,** 507-509.

Wang, N., Mirando, A. J., Cofer, G., Qi, Y., Hilton, M. J. & Johnson, G. A. 2019. Diffusion Tractography of the Rat Knee at Microscopic Resolution. *Magn Reson Med,* 81**,** 3775-3786.

Wexner, S. D., Coller, J. A., Devroede, G., Hull, T., McCallum, R., Chan, M., Ayscue, J. M., Shobeiri, A. S., Margolin, D., England, M., Kaufman, H., Snape, W. J., Mutlu, E., Chua, H., Pettit, P., Nagle, D., Madoff, R. D., Lerew, D. R. & Mellgren, A. 2010. Sacral Nerve Stimulation for Fecal Incontinence: Results of a 120-Patient Prospective Multicenter Study. *Ann Surg,* 251**,** 441-9.

WHO. 2018. *Diabetes* [Online]. World Health Organization. Available: https://www.who.int/news-room/fact-sheets/detail/diabetes [Accessed March 3 2019 2019].

Wickersham, I. R., Sullivan, H. A. & Seung, H. S. 2013. Axonal and Subcellular Labelling Using Modified Rabies Viral Vectors. *Nature Communications,* 4**,** 2332.

Williams, E. K., Chang, R. B., Strochlic, D. E., Umans, B. D., Lowell, B. B. & Liberles, S. D. 2016. Sensory Neurons that Detect Stretch and Nutrients in the Digestive System. *Cell,* 166**,** 209-21.

Wyart, E., Bindels, L. B., Mina, E., Menga, A., Stanga, S. & Porporato, P. E. 2020. Cachexia, a Systemic Disease Beyond Muscle Atrophy. *Int J Mol Sci,* 21.

Yahagi, N. 2017. Hepatic Control of Energy Metabolism via the Autonomic Nervous System. *J Atheroscler Thromb,* 24**,** 14-18.

Yao, G., Kang, L., Li, J., Long, Y., Wei, H., Ferreira, C. A., Jeffery, J. J., Lin, Y., Cai, W. & Wang, X. 2018. Effective Weight Control via an Implanted Self-Powered Vagus Nerve Stimulation Device. *Nature Communications,* 9**,** 5349.

Yoo, P. B., Lubock, N. B., Hincapie, J. G., Ruble, S. B., Hamann, J. J. & Grill, W. M. 2013. High-Resolution Measurement of Electrically-Evoked Vagus Nerve Activity in the Anesthetized Dog. *J Neural Eng,* 10**,** 026003.

Yuan, H. & Silberstein, S. D. 2016. Vagus Nerve and Vagus Nerve Stimulation, a Comprehensive Review: Part I. *Headache,* 56**,** 71-8.

Biography

Aliesha O'Raw, neé Aliesha Garrett, earned a B.S. in engineering with concentration in bioengineering from Franklin W. Olin College of Engineering in 2014. She earned an M.S. in biomedical engineering with a concentration in neuroengineering from Duke University in 2021. Her publications include "Microscopic matrix remodeling precedes endothelial morphological changes during capillary morphogenesis," "Poly(GP) proteins are a useful pharmacodynamic marker for C9ORF72-associated amyotrophic lateral sclerosis," "The extreme N-terminus of TDP-43 mediates the cytoplasmic aggregation of TDP-43 and associated toxicity in vivo," "Spt4 selectively regulates the expression of C9ORF72 sense and antisense mutant transcripts," "C9ORF72 poly(GA) aggregates sequester and impair HR23 and nucleocytoplasmic transport proteins," Poly(GR) impairs protein translation and stress granule dynamics in C9ORF72-associated frontotemporal dementia and amyotrophic lateral sclerosis," "An intravital window to image the colon in real time," "Intravital imaging of mouse embryos," "The frontier of live tissue imaging across space and time," and "Mapping the peripheral nervous system in the whole mouse via compressed sensing tractography." Aliesha is a Duke Preparing Future Faculty Fellow and a Research Affiliate with the Terasaki Institute for Biomedical Innovation.